Department of Precision and Microsystems Engineering

Attitude Control of Flapping-Wing Air Vehicles

Bas Roulaux

Report no : 2021.028
Supervisor : Hans Goosen
Specialisation : Engineering Dynamics
Type of report : Thesis
Date : May 3, 2021

TU Delft Delft University of Technology

Challenge the future

Attitude Control of Flapping-Wing Air Vehicles

by

A.S. Roulaux

For the degree of Master of Science in High Tech Engineering at Delft University of Technology
To be defended publicly on Monday May 3, 2021 at 10:00.

Student number:	4375335	
Supervisor:	Dr.ir. J.F.L Goosen,	TU Delft
Thesis committee:	Dr.ir. J.F.L Goosen,	TU Delft
	Dr.ir. V van der Wijk,	TU Delft
	Ir. B.D.W. Remes,	TU Delft

Faculty of Mechanical, Maritime and Materials Engineering (3mE) · Delft University of Technology

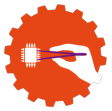

Precision and
Microsystems
Engineering

Abstract

Flapping-Wing Air Vehicles (FWAVs) are autonomously flying vehicles that use their flapping wings to simultaneously stay aloft and enable controllable flight. Numerous vehicles that are capable of controllable flight are found in literature, where many different attitude control mechanisms are used to control the amount of lift that is produced by each wing. This research strives to find the most suitable attitude control mechanism for the Atalanta drone, where two mechanisms are compared in terms of aerodynamic performance: the variation wing stroke amplitude and the variation of Angle of Attack (AOA) by means of a variable pitching hinge stiffness.

This study presents a model that consists of two main parts: an analytical quasi-steady aerodynamic model and an analytical Multi-Body Dynamics (MBD) mechanical model. Analytical models were chosen over numerical methods, due to their combination of low computational power while still achieving results with an acceptable error. The analytical aerodynamic model uses four aerodynamic terms to compute the passive pitching motion and total lift force, with only the local wing stroke kinematics and wing morphology as input. The mechanical model describes the kinematics of the vehicle body and flapping wings analytically in multiple reference frames, which allows for analytical calculation of the contribution of global body motions to local wing motions. This new approach directly allows for calculation of the contribution of body global motions to wing aerodynamics, which has not been done before in such an extensive manner in FWAV research. The aerodynamic analysis is limited to the analysis of one wing, in order to limit the computational effort.

The two models are combined to research the influence of the wing stroke amplitude and the stiffness of the wing's pitching hinge on the lift production of the dronefly wing design. To this end, the most useful description of the wing kinematics was researched, which resulted in a purely sinusoidal wing stroke and a passive pitching motion, while the out of plane wing motion was neglected. Using this description of the wing kinematics, the attitude control parameters were varied for different cases of body motion. It was found that without body motions, the lift force increases consistently with each increase in wing stroke amplitude where variation of the pitching hinge stiffness shows clear local optima instead of a consistent increase in lift within the design domain. When body motions are introduced, the induced airflow changes the passive pitching motion of the wing, which makes the lift force production more sensitive to changes in pitching stiffness. It is concluded in this report that a certain minimal pitching stiffness is necessary to ensure stable flapping kinematics, when body motions are introduced. Similarly, while the vehicle is subjected to external flows due to

body motion, a minimal pitching stiffness is required to ensure an increase in lift force when the stroke amplitude is increased. For the dronefly wing design, for which the kinematic and morphological parameters are optimized for efficient lift production, variation of the attitude control parameters leads to a decrease in lift production efficiency for the case that does not include body motion, with a maximum decrease of 2%. When body motions that mimic forward flight are introduced, the lift production generally increases compared to the case that does not include body motion, though the efficiency can drop as much as 27%. Experiments with a different, non-optimized wing design show similar results, though pitching kinematics can become chaotic for certain combinations of attitude control parameters and body motion cases.

Lastly, for both wing designs, research was done into the contribution to the attitude control of the change in effective Center of Pressure (CP) due to variation of the attitude control parameters. In all flow cases, the CP showed variations that have a negligible influence on the attitude control torques, with respect to the variations in lift force. Hence, the conclusion was drawn that a constant torque arm with respect to the body's Center of Gravity (CoG) can be assumed within each flow case while the lift forces are varied.

From the experiments that were done with the presented analytical model, it is concluded that a variation in wing stroke amplitude shows the most predictable aerodynamic results for an attitude control mechanism while using the dronefly wing design, provided that the pitching stiffness is high enough to ensure stable flapping kinematics during flight.

Acknowledgements

Although this thesis was a solo project, it could not have been completed without the support of the following people. Firstly, I would like to thank my supervisor Hans Goosen. His limitless patience with the theoretical and practical issues that came along during my project, gave me the opportunity to explore the full width of my project before zooming in on the results that were eventually presented. This made our discussions during meetings extremely interesting, gave me the opportunity to really find my own way during my project and made me see the importance of doing so. Besides making this a better project, the insights provided by Hans definitely made me a better engineer!
I'm also very grateful for the support from my friends, fellow students and fellow members of the Taylor Board who provided me with the fun distractions that any student needs during their thesis, even though we've spent most of our time at home this year. Not suprisingly, my housemates were a big help during this year as well, keeping me sharp and sane with good conversation, good laughs and good coffee. Last but not least, I would like to thank my parents. Their endless support during all my endeavors in- and outside of Delft over the past 7 years have made my time as a student an unforgettable experience.

Delft
April 19, 2021

Bas Roulaux

Table of Contents

List of Figures

List of Tables

Acronyms

UAV	Unmanned Air Vehicle
FWAV	Flapping-Wing Air Vehicle
CoG	Center of Gravity
CP	Center of Pressure
AOA	Angle of Attack
CFD	Computational Fluid Dynamics
MBD	Multi-Body Dynamics
LEV	Leading Edge Vortex
DOF	Degree of Freedom

Chapter 1

Introduction

Unmanned Air Vehicles (UAVs) have proven to be a useful tool in many different fields over the past few decades. From monitoring agriculture maintenance to international surveillance, UAVs seem to get the best of their terrestrial counterparts. Flapping-Wing Air Vehicles (FWAVs) are a specific type of UAV that use flapping wings for lift production and propulsion as opposed to the fixed wings of an airplane or the rotary wings of a helicopter. Research into UAVs has increased rapidly over the past two decades, where FWAV research has a large contribution to the total field, as shown in Figure 1-1.

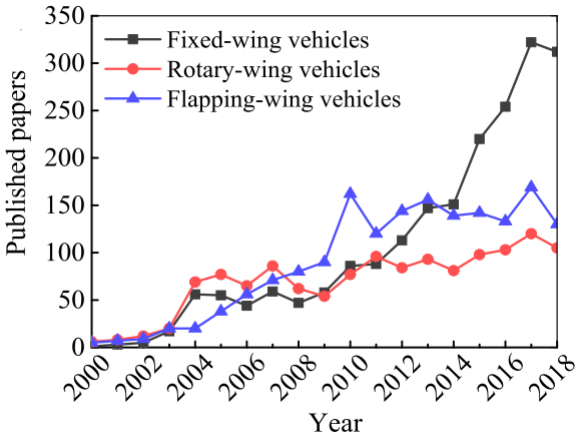

Figure 1-1: Graph showing the increase in UAV research from 2000 to 2018, courtesy of [34]

The main interest in FWAVs originates from the favourable scaling of flapping-wing aerodynamics at small sizes compared to rotary-wing vehicles and fixed-wing vehicles [41], and an increased manoeverability compared to fixed-wing vehicles. It should be noted that research into FWAV is still very much ongoing, which is why there is still some discussion on the actual efficiency of FWAVs at small scales and their implementation ([20], [41]). As Figure 1-1 suggests, many different FWAV designs exist today, hence multiple attempts to categorize

and analyze these vehicles in review papers have been done ([4], [34], [40]). From these review papers, it follows that by far most designs are inspired by bird and insect flight, although the performance gap between animal flight and FWAV flight is still significant [26], [35].

1-1 The Atalanta

A specific FWAV that is of interest in the current work, is the Atalanta, shown in Figure 1-2. This particular vehicle, with a wingtip-to-wingtip size of around 15cm, has a main actuator that brings the compliant main body into resonance in order to drive its wings, much like fruit flies do [2]. Although this description sounds rather straightforward, transferring this mechanism from a biological creature to a man-built mechanism is not. Therefore, the Atalanta does not yet perform as desired, as mentioned in the review paper by Phan et al. [34] where the performance of many different FWAV designs from literature are documented.

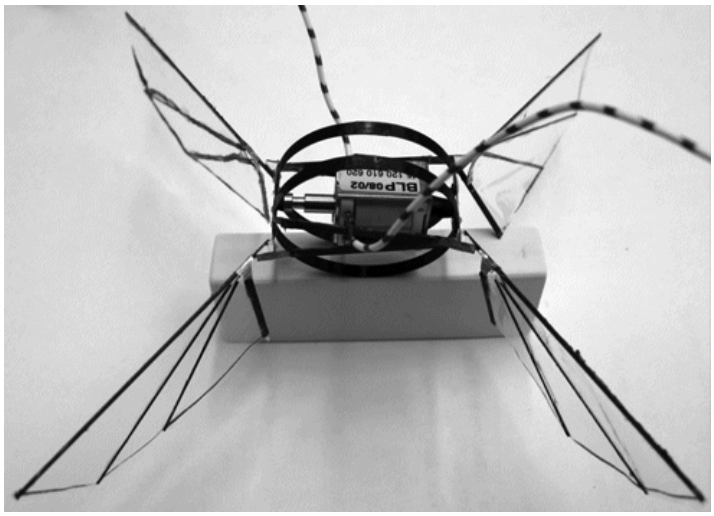

Figure 1-2: The Atalanta FWAV, courtesy of [2].

1-1-1 Performance Criteria

In general, the performance success of an FWAV can be defined by two criteria, as described by Phan et al. [34]: flight capability and attitude control.

Flight capability is successful for an FWAV if the vehicle produces sufficient lift force to overcome its downward gravitational force. To achieve this, the design of the vehicle must be lightweight with respect to the aerodynamic power that it generates. Therefore, the power source and mechanism that generate the flapping motion must be efficient, alongside the kinematics of the flapping motion that need to be efficient as well. Hence, achieving flight capability for FWAV is an integrated design challenge where driving mechanism, power source, power electronics, flapping kinematics and wing shape design all need to match.

Attitude control is successful for an FWAV when the vehicle can actively control its maneuvers and can compensate for external disturbances during flight. To achieve this, the vehicle must

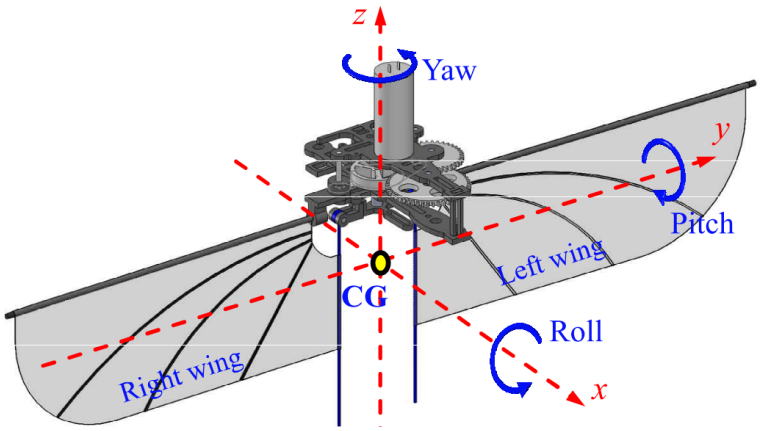

Figure 1-3: A schematic drawing of the three rotation axes of an FWAV, courtesy of [33]

be able to control its angular position around its three main axes of rotation: roll, pitch and yaw (as shown in Figure 1-3). This is done by creating torques around each of these three axes by manipulating the aerodynamic forces that are produced by each wing in terms of magnitude and timing along the wing stroke.

Before attitude control can be achieved, an FWAV must be capable of flight, since attitude control can only be used in a vehicle when it is capable of staying aloft. Therefore, attitude control is an additional challenge on top of flight capability, which is already a challenge as described earlier. Due to the tendency to first design for flight capability instead of attitude control, the attitude control system is oftentimes not taken into account in FWAV design. This results in a limited set of attitude control mechanisms available in literature, though some researchers have succeeded in the design and implementation of such mechanisms as will be shown in 1-1-2.

The Atalanta has no clearly designed attitude control system yet, though some research has been done into attitude control mechanism design for this vehicle. For instance, multiple options for attitude control actuators have been proposed by Peters et al. [29], and a measurement setup to test one of these actuator mechanisms has been built and tested as well [31]. Although the mechanism shows some potential for attitude control, the mechanism cannot be implemented directly into the Atalanta yet and many unknowns have to be solved before this mechanism could be actually attached to the Atalanta and provide for attitude control.

Fundamental mechanical research into attitude control for the Atalanta was done in earlier research ([9], [30]), which is mostly aimed at the manipulation of the body's structural dynamics for the purpose of attitude control. The results from these reports look promising, though actual implementation of these models into a mechanism is not possible yet.

Research that includes the sensitivity of flapping-wing aerodynamics to design parameters is done by Wang et al. [46], which shows that the lift production of a flapping wing shows different sensitivities with respect to different design parameters and kinematic parameters. This was mostly researched for the purpose of wing optimization, though theoretically some of these parameters could be varied intentionally to provide for attitude control.

Since other Atalanta-specific attitude control research is absent, the current work approaches the attitude control challenges from a mechanism perspective combined with an in-depth

analysis of the aerodynamic force responses, rather than an actuator perspective. This was done in order to explore the possibilities beyond the earlier research that was mentioned. To this end, a short summary of findings in literature is presented below.

1-1-2 Attitude Control Mechanisms

As mentioned earlier, despite the advanced design challenges, literature shows that some researchers have succeeded in the design of an FWAV that is capable of both flight and attitude control. An overview of examples of these mechanisms and their attitude control capabilities for the three main axes of rotation is given in Table 1-1.

Due to the Atalanta being symmetric along its two horizontal axes, the development of a successful roll mechanism could be used for the pitching direction as well. Therefore, this work limits itself to focus only on the attitude control around the roll axis of the vehicle. As Table 1-1 shows, many roll mechanisms are available in literature. However, the compliant, tailless design of the Atalanta along with the use of one central flapping actuator excludes many of the mechanisms that are proposed in literature. Therefore, the two mostly used attitude control systems from literature that are still suitable for the Atalanta design are given here: variation of the stroke amplitude and Angle of Attack (AOA) manipulation.

Variable Stroke Amplitude

In an article published by Mahjoubi and Byl [23] it is shown that during each flapping cycle, the average aerodynamic force is almost a quadratic function of the stroke amplitude. This makes stroke amplitude control a considerable option to use for control of roll motion. An example of an FWAV that makes use of this steering mechanism, is the improved Robobee by Ma et al. [21]. This FWAV has one actuator for each wing, to control the stroke amplitude of each wing independently and therefore control the roll torque generated by the wings. A picture of the Robobee is shown in Figure 1-4, and experiments have shown that it is capable of controllable flapping-wing flight.

Additionally, research was done on controlling the stroke amplitude while using one synchronous actuator that actuates the flapping motion, and one actuator controlling the stroke amplitudes of the wings relative to each other. Research by Park et al. [28] shows the design of such a flapping mechanism, which creates a flapping asymmetry by changing the lengths of transmission linkages with respect to one another. This is done by moving the central actuator while keeping the flapping frequency constant. A schematic drawing of this mechanism is given in Figure 1-5. This mechanism has been built and tested to be mechanically sound, although flight tests have not been done yet, which means that the mechanism is not proven to work in flight.
For the Atalanta, the stroke amplitude could be manipulated by locally adjusting the stiffness of the hinges that allow for the flapping motion. This way, the amplitude can be controlled per wing much like the Robobee [21] and the separation of the driving actuator with constant frequency and the attitude control actuators would be maintained as suggested in the asymmetric flapping mechanism by Park et al. [28].

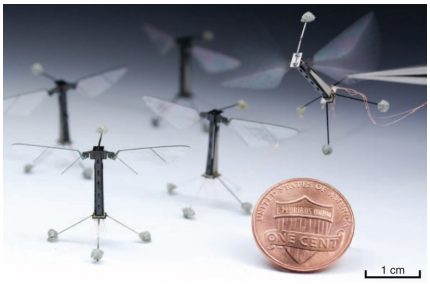

Figure 1-4: A picture of the Robobee, courtesy of [21].

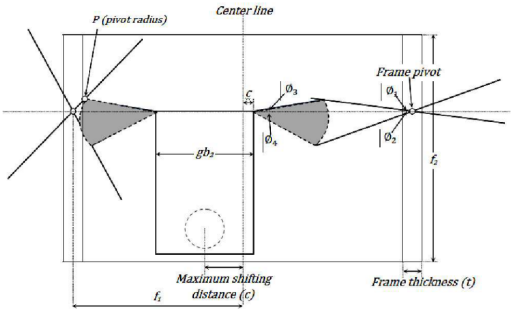

Figure 1-5: Schematic drawing of the asymmetric amplitude flapping mechanism, courtesy of [28].

AOA Manipulation

The lift force created by the flapping motion of a wing highly depends on the AOA of the wing with respect to the surrounding air. For a rigid wing, the AOA is constant along the wing span, while for flexible wings, the AOA depends on the twist profile of the wing. Flexible wings with more twist generate more lift than slightly twisted wings, up to a certain optimum. Hence, a roll torque can be created by modulating the twist distribution of the wings on either side of the vehicle. Various examples of wing twist modulation exist, but a clear distinction can be made between flapping mechanisms that use wing twist modulation for passively rotating wings and wings of which both the rotation and twist are actively modulated.
A clear example of a wing-twist attitude control mechanism which has passively rotating wings is the Nano Hummingbird by AeroVironment [18], shown in Figure 1-6. This mechanism has flexible wings, which rotate freely around the leading edge. The amount of wing twist is modulated by an actuator which applies a force on the wing roots to create tension in the leading edge of the wing, where low tension results in more twist and vice versa. A schematic representation of this wing twist system is given in Figure 1-7. Note that similar to wing twist of a flexible wing, one could also control the AOA of a rigid wing to manipulate the amount of lift production per wing. For the Atalanta, this could be done by adjusting the stiffness of the pitching hinge that allows for the passive rotation of the wing around its leading edge.

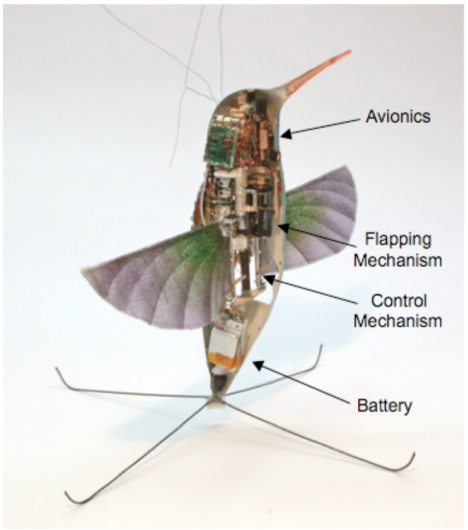

Figure 1-6: Picture of the Hummingbird developed by AeroVironment, courtesy of [18].

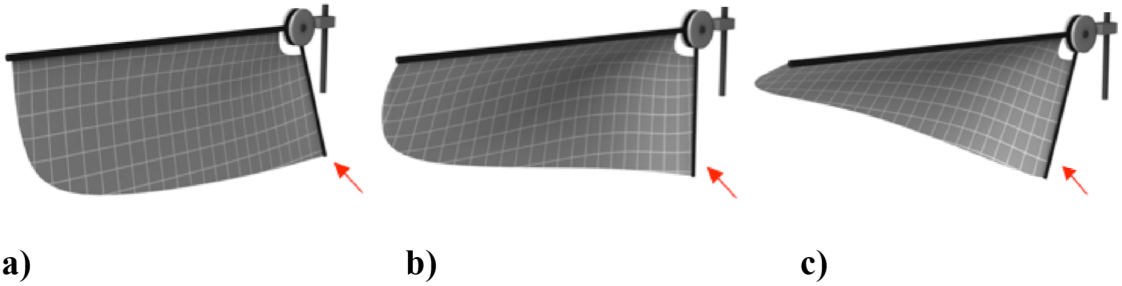

Figure 1-7: Wing twist modulation in Hummingbird, courtesy of [18]. a) Shows high force on root spar which means low twist and lift, c) shows low tension which means high twist and lift, b) shows an intermediate tension state which shows an increase in lift compared to a) and a decrease in lift compared to c).

Name	AC success	Roll	Pitch	Yaw	AC actuator
62 g robotic hummingbird [6]	Yes	VSA	SPI	SPI	Servo motor
Asymmetric flapping mech. [28]	No	VSA	-	-	Servo motor
Bat bot [36]	Yes	WTM	WTM	-	Undefined
BionicOpter [12]	Yes	VSA, WTM AFF	VSA, WTM AFF	VSA, WTM AFF	DC motor and servo motor
Butterfly-type ornithopter [5]	Yes	VOWA	VOWA	VOWA	Servo motor
Colibri [39]	Yes	WTM	WTM	-	Servo motor
Daedal Flapper [15]	Yes	VSA	SPI	SPI	Servo motor
Delfly I [7]	Yes	TWC	TWC	-	Electromagnetic actuator
Delfly Nimble [17]	Yes	AFF	VOWA	WTM	Roll: DC motor Pitch & yaw: servo motor
H2 bird [38]	Yes	-	TWC	TP	Pitch: servo motor. Yaw: unspecified
Improved Robobee [21]	Yes	VSA	VOWA	SC	Piezo electric bending beam
Insect-like FW MAV [14]	Yes	WTM	WTM	-	DC motor
KU beetle [33]	Yes	WTM	WTM	WTM	Servo motor
KUBeetle-S [32]	Yes	WTM, SPI	WTM, SPI	WTM	DC motor and servo motor
Nano Hummingbird [18]	Yes	WTM	WTM	WTM, AoAC	Servo motor
NUS Roboticbird [25]	Yes	AFF	SPI	SPI	Roll: DC motor Pitch & yaw: servo motor
Purdue hummingbird robot [50]	Yes	VSA	WTM	SC	DC motor
Quad-thopter [8]	Yes	AFF	AFF	AFF	DC motor
Resonance MAV [16]	Yes	VSA	VOWA	-	Pager motor
Robo Raven [13]	Yes	VSA	TWC	-	Servo motor
Smart bird [22]	Yes	WTM	WTM	-	Servo motor
TechJect Dragonfly [37]	Yes	VSA	VSA	VSA	Solenoid
Tunable impedance [23], [3], [24]	No	-	VOWA	AoAC	Not specified
VTOL MAV [11] [10]	No	SPI, MCoG	SPI, MCoG	-	Undefined, shape memory alloy suggested

Table 1-1: Table containing the attitude control mechanisms that were found in literature . The abbreviations mean the following: WTM - Wing Twist Modulation. SPI - Stroke Plane Inclination. MCoG - Moving Center of Gravity. TWC - Tail wing Control. VSA - Variable Stroke Amplitude. VOWA - Variable Offset Wing Angle. AFF - Asymmetric Flap Frequency. SC - Split Cycle. TP - Tail Propeller. AoAC - Angle of Attack Control

1-2 Project Description

This section describes the thesis aim, research question, the strategic plan and gives an overview of the contents of this report.

1-2-1 Aim of Thesis

The aim of this thesis is to develop a theoretical framework for the aerodynamic response of flapping wings that incorporates variation of attitude control parameters and motion of the vehicle body. The framework is developed so that the aerodynamic performance and robustness of different attitude control parameters can be analyzed and compared.

1-2-2 Research Question

The research question is formulated as follows:

Which attitude control mechanism is aerodynamically most suitable for the Atalanta?

To answer this question, the following subquestions are formulated:

- Which attitude control method results in the largest force change?
- Which aerodynamic force components are dominant in attitude control?
- Does the roll torque generation only depend on force differences, or is the torque arm a relevant factor as well?
- Which attitude control method is most robust to external factors, such as vehicle body motions?
- Does the wing morphology influence the aerodynamic response sensitivity to attitude control parameters?

1-2-3 Strategic Plan

The main focus of the research question is on the aerodynamic performance and the variation thereof when attitude control parameters are varied. Since this thesis aims to develop a theoretical framework to answer this research question, two theoretical models need to be formulated and combined: an aerodynamic model and a kinematic model. Both models can be partly based on earlier research, but due to the novelty of aerodynamic attitude control analysis that includes body motion, both models need to be extended beyond their current capabilities. After researching the most suitable combination of aerodynamic and kinematic descriptions, the total combined model needs to be tested by means of numerical experiments that show the aerodynamic performance for different attitude parameters and body motion conditions. Since physical experiments into attitude control that include the influence of

body motion are absent, the models and numerical experiments are mostly focused on finding the general aerodynamic response of the wing in a computationally efficient way, rather than finding the most detailed and accurate aerodynamic description that is very specific for one mechanism.

1-3 Thesis Overview

Firstly, the aerodynamic model that describes the loads on the wing is formulated in chapter 2. Subsequently, the kinematic formulation that extends the existing flapping formulation to a flapping formulation that includes body motion is described in chapter 3. The basic characteristics of the aerodynamic performance of flapping wings for different kinematic descriptions are analyzed in chapter 4, which results in the flapping formulation that is most useful for this thesis. This flapping formulation is then combined with the aerodynamic and kinematic formulations into one framework, so that the performance of the two attitude control mechanisms (stroke amplitude variations and AOA control by means of pitching stiffness variations) can be analyzed. The results of this analysis are shown in chapter 5, after which the conclusions of this research will be presented in chapter 6 along with a discussion and future recommendations.

Chapter 2

Flapping-Wing Aerodynamics

This chapter describes the predictive quasi-steady aerodynamic formulation that is used in this work to compute the aerodynamic forces associated with flapping-wing motion. Firstly, it will be discussed why a quasi-steady formulation is the most suitable and a background of the currently used formulation will be given along with the assumptions that are made in this formulation. Subsequently, the definitions of the morphological parameters of the wing will be described. Lastly, the equations that define the forces and the effective Center of Pressure (CP) locations are given for each aerodynamic force component

2-1 The Quasi-Steady Aerodynamic Formulation

Finding a suitable formulation for the aerodynamics of flapping wings is a cumbersome task due to the inherently unsteady behaviour of the flapping motion and the unsteady aerodynamic effects that produce the aerodynamic loads. Two existing ways to take most unsteady effects into account, are the use of Computational Fluid Dynamics (CFD) and experimental studies. Despite their relatively high accuracy, both of these methods have their limitations for motion analysis of flapping wing vehicles. Firstly, CFD is known for its high computational cost when calculating aerodynamic forces over time, with a large dependency on the definition of flow conditions. This makes a time dependent aerodynamic analysis of a flapping-wing vehicle including body motion and attitude control that considers multiple scenarios a very lengthy process. On the other hand, physical experimental studies can be performed and analyzed rather swiftly, though the design and realization of the experiment are both very time consuming and the experiments themselves are prone to measurement errors.

An analytical formulation would be a slightly less accurate, though more efficient solution for the aerodynamic analysis. A specific analytical aerodynamic formulation developed by Wang et al. [47], which is used in the current work, comes with a set of assumptions that drastically decrease the computational effort of the calculations. For an in-depth motivation of the assumptions that were made by Wang et al. the reader is referred to the motivation given in their original work, since the current work is focused on the general aerodynamic and

kinematic principles that are taken into account rather than the in-depth aerodynamics. The four most important assumptions made in the formulation by Wang et al. are the following:

1. The flow across the wing is incompressible, meaning that the fluid density term ρ^f is a constant. This is due to the fact that the maximal velocity of the wing is far below the speed of sound.
2. The flapping wing is modeled as a rigid plate, which means that wing deformation is neglected. Moreover, the wing thickness t is regarded as negligible compared to the wing span R and the average chord length $\bar{c}$. Figure 3-1 shows a visual representation of these parameters.
3. The resultant aerodynamic force on the wing is perpendicular to the wing surface at all times.
4. A quasi-steady state is assumed for infinitesimal periods of time, meaning that the transient loads on the wing are assumed to be equivalent to the loads for steady motion while using the instantaneous Angle of Attack (AOA), velocities and accelerations from the unsteady kinematic behaviour.

Different quasi-steady formulations existed before the research by Wang et al. [47] which means that the model proposed by their research does not stand by itself. Their research shows a quasi-steady formulation that combines different models from earlier research into flapping-wing aerodynamics (mostly the models proposed by Berman & Wang [1] and Whitney & Wood [48]) in one model to tackle the following three apparent issues in research into quasi-steady aerodynamic formulations:

1. The number of aerodynamic loading terms that is taken into account in different models in literature is inconsistent. The model by Wang et al. [47] aims to eliminate this inconsistency.
2. The contribution of the wing rotation around its pitching axis is incomplete in most quasi-steady models, hence this model aims to model this load contribution and corresponding Center of Pressure (CP) more accurately.
3. Many of the earlier quasi-steady aerodynamic models rely on empirical parameters to a large extent, which limits the possibilities of those models to be used for different wing shapes, kinematic properties, load cases etc. The model proposed by Wang et al. aims to reduce this dependence on empirical parameters in order to find a more general formulation compared to previous models.

Since the work by Wang et al. was found to be the only model that extensively compares different quasi-steady formulations and uses as few empirical parameters as possible (up until now), it was decided to use their quasi-steady aerodynamic formulation in this work. Additionally, the formulation shows a better agreement with physical measurements than other formulations in literature and it is more broadly applicable due to independence of empirical parameters. Moreover, the kinematic formulation of the work by Wang et al. allows for the addition of extra kinematic components like body motion and hinge motion, as is desired for the current work. How this is done, will be shown in chapter 3.

2-2 Wing Morphology

This section discusses the parameters that are used in this work to describe the full morphology of the rigid flapping wing. The flapping wing is attached to the main body at the wing root through the wing hinge. It depends on the type of kinematic formulation how many degrees of freedom (DoFs) this wing hinge has. Independent of its formulation (either rigid or flexible) the wing can rotate around its pitching axis due to aerodynamic forces. The pitching axis and other wing parameters and definitions can be found in Figure 3-1.

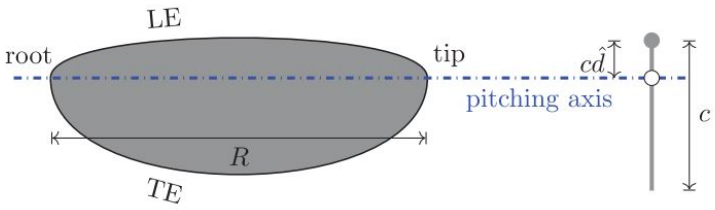

Figure 2-1: Schematic representation of a flapping wing, showing different relevant wing parameters and the definitions of leading edge (LE) and trailing edge (TE). In the lateral view on the right, the LE is represented with a filled gray circle and $\hat{d}$ is the dimensionless distance from the LE to the pitching axis. Courtesy of [47].

Wing morphology plays an important role in flapping wing analysis. First of all, the dimensions and material of the wing determine the wing's weight distribution and therefore the inertia with respect to each rotation axis. Additionally, some dimensional characteristics of the wing (such as the wingspan and chord), have an effect on the production of aerodynamic forces by the wing. The dependency of wing aerodynamics on each wing dimension will be further discussed in section 2-3. Since the wing will be modeled as a rigid plate in the current work, the stiffness distribution of the wing itself will not be taken into account.

2-3 Flapping Wing Aerodynamics

As mentioned earlier, the quasi-steady formulation by Wang et al. [47] that is used in this work describes the aerodynamic flapping-wing forces analytically. Finding a single analytical representation that captures the all properties of the unsteady flow around a flapping wing is not trivial, therefore the aerodynamic loads on the wing are divided into four different contributions: translation-induced forces, rotation-induced forces, coupling forces and forces due to the added-mass effect. A schematic representation of these four aerodynamic load components is given in Figure 2-2.

In order to account for the variation of velocity and acceleration along the wing, the blade-element method (BEM) as developed by Osborne [27] is used to compute the total force acting on the flapping wing. This method divides the flapping wing into chordwise strips with a finite width, after which the kinematic information of each strip can be used to determine the aerodynamic force on each strip. Adding the strip forces over the entire wingspan gives the instantaneous aerodynamic force on the wing at a certain time instance. The Wagner

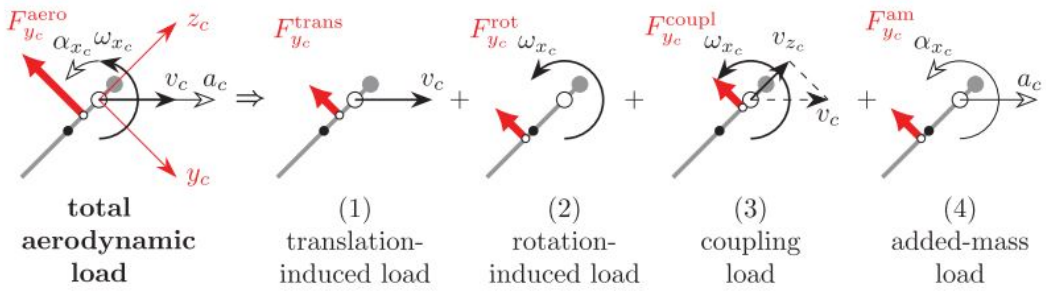

Figure 2-2: The decomposed aerodynamic loads on a flapping wing. Grey lines represent the chord, grey dots represent the leading edge (LE), large white circles represent the pitching axis and black circles represent the chord center. The smaller white circles represent the CoP of the respective load. Note that the wing's kinematic quantities and loads are represented in a qualitative way. Courtesy of [47].

effect [45], which describes additional forces introduced by the formation of Leading Edge Vortices (LEVs) when the wing accelerates from standstill, is taken into account in various quasi-steady formulations, though no benchmark exists as of yet that indicates in which cases it should be taken into account. It was decided to not take this effect into account, since there are no apparent arguments to do so and the work by Wang et al. [47] has shown that it should not be taken into account for at least one type of wing that is analyzed in this work: the artifical wing that is inspired by the wing of the Eristalis tenax (dronefly). It should be noted that the description of the aerodynamic forces below are not only used for the calculation of the lift forces that are produced by the flapping wing. The research by Wang et al. makes use of an iterative function that calculates the passive pitching motion of the wing due to the aerodynamic loads. This means that the aerodynamic formulation, combined with the input kinematics imposed by the flapping mechanism, is firstly used to calculate the torques around the pitching axis that induce the passive pitching motion. The full kinematics, including the pitching motion, are then used to calculate the lift forces that are produced by the flapping wing. It is described in chapter 4 whether such a passive pitching formulation is useful for the purposes of this research.

2-3-1 Notation Conventions

It should be noted that the kinematic description of the wing in the current work is formulated in a slightly different way from the original formulations by Wang et al. [47]. Since additional kinematic terms are added in the current work (in chapter 3), the kinematic formulation of the velocities and accelerations of point p on the wing need to be defined in a new way. Therefore, the aerodynamic terms based on the research of Wang et al. are discussed in this work, with the following notation conventions.
The kinematic properties of point p are all formulated in the reference frame that is fixed to the flapping wing, referred to as the corotating frame c. The notation of kinematic variables in the corotating frame is done in the following way: ${}^{c}\boldsymbol{v}_p$, ${}^{c}\boldsymbol{a}_p$, ${}^{c}\boldsymbol{\omega}_W$, ${}^{c}\boldsymbol{\alpha}_W$ are the linear velocity of point p, the linear acceleration of point p, the angular velocity of the wing and angular acceleration of the wing, respectively. Components of these velocities and accelerations will be written with triple subscripts, for example the velocity of point p in the y direction of the

corotating frame c is written as $v_{p_{y_c}}$. How the kinematic variables are described in different reference frames, will be discussed in chapter 3. For the aerodynamic load analysis, the kinematic variables ${}^c\boldsymbol{v}_p, {}^c\boldsymbol{a}_p, \omega_{x_c}$ and α_{x_c} as shown in Figure 2-2 are sufficient.
In the following sections, the analytical formulations for each of the four aerodynamic loads, as defined by Wang et al. [47], are described together with the effective CP formulations for each aerodynamic load component.

2-3-2 Translation-Induced Loads

While calculating the translational loads on a flapping wing, the wing is described as a rigid plate that linearly moves through a fluid under a certain AOA. The translational loads can be directly calculated from the wing kinematics, the morphological parameters of the wing (chord c) and the density (ρ^{f}) of the fluid that surrounds the wing, using the following equation for the translational force on the wing in the y direction of the corotating frame $F_{y_c}^{\text{trans}}$:

$$F_{y_c}^{\text{trans}} = -\operatorname{sgn}\left(v_{p_{y_c}}\right) \frac{1}{2}\rho^{\text{f}} \int_0^R C_{F_{y_c}}^{\text{trans}} \, |{}^c\boldsymbol{v}_p|^2 c \, dx_c. \tag{2-1}$$

The $C_{F_{y_c}}^{\text{trans}}$ variable in Equation 2-1 represents the translational force coefficient in the y direction of the corotating frame, which is derived from the translational lift coefficient C_L^{trans} in the following way:

$$C_{F_{y_c}}^{\text{trans}} = C_L^{\text{trans}} / \cos\tilde{\alpha}. \tag{2-2}$$

Extensive experimental research into the translational lift coefficient of a wing has shown that the lift coefficient can be approximately written as

$$C_L^{\text{trans}} = A \sin 2\tilde{\alpha}, \tag{2-3}$$

with A the maximum lift coefficient that depends on the wing shape and $\tilde{\alpha}$ the angle of attack (AOA) of a rigid wing, which are respectively calculated as follows:

$$\tilde{\alpha} = \arccos \frac{|v_{p_{z_c}}|}{|{}^c\boldsymbol{v}_p|}, \quad \text{if} \quad {}^c\boldsymbol{v}_p \neq \mathbf{0}, \tag{2-4}$$

$$A = \frac{\pi \, \text{AR}}{2 + \sqrt{\text{AR}^2 + 4}}, \tag{2-5}$$

where AR is the aspect ratio of the wing, which is defined as $\frac{R}{\bar{c}}$. Note that $C_{F_{y_c}}^{\text{trans}}$ is written inside the integral in Equation 2-1, since it depends on ${}^c\boldsymbol{v}_p$, which varies with the spanwise position of p on the wing.

Experimental research into the effective CP of the translational force on flapping wings, has shown that the chordwise effective CP location shifts from near the LE to the chord center with the increase of the AOA. The experimental research shows that the relation between

AOA and the dimensionless chordwise location $\hat{d}_{cp}^{\text{trans}}$ of the effective CP (with $\hat{d}_{cp}^{\text{trans}} = 0$ at the LE) is equal to

$$\hat{d}_{cp}^{\text{trans}} = \frac{\tilde{\alpha}}{\pi}, \quad \text{where} \quad 0 \leq \tilde{\alpha} \leq \frac{\pi}{2}. \tag{2-6}$$

The spanwise coordinate of the effective CP is equal to the spanwise coordinate of the wing strip that is analyzed.

Both the spanwise and chordwise effective CP coordinates are taken into account for every wing strip as defined in be BEM, and combining these with the force on each wing strip as defined in Equation 2-1 enables calculation of the torques that are induced by the aerodynamic translational force on each wing strip. Integrating the torques on each element over the wingspan results in the total torques around the x_c and z_c axes of the wing, for which the explicit formulas are given in [47].

2-3-3 Rotation-Induced Loads

The rotational loads describe the loads on the wing as it rotates around a certain axis in a medium, which leads to distributed loads along the wing. The calculation of the rotational loads only take the rotational motion of the wing into account and, similar to the calculation of the translational force, the kinematic information, morphological properties of the wing and the fluid properties are the only terms that are necessary to calculate the rotational aerodynamic loads. The axis of rotation that is taken into account for this load term, is the pitching axis (see Figure 3-1). Due to this definition, the chordwise strips that are used in the BEM is insufficient, since the wing strips have a velocity profile that linearly increases with the distance from the pitching axis. Therefore, the chordwise strips must be discretized as well, meaning that the wing is divided into a mesh and the rotational loads are calculated by determining the load on each infinitesimal area $dx_c dz_c$ and integrating over the entire wing mesh. The resulting equation for the rotation-induced force on the wing in y_c direction is

$$F_{y_c}^{\text{rot}} = \frac{\rho^{\text{f}}}{2} \omega_{x_c} |\omega_{x_c}| C_D^{\text{rot}} \int_0^R \int_{\hat{d}c-c}^{c} z_c |z_c| dz_c dx_c, \tag{2-7}$$

with

$$C_D^{\text{rot}} = \frac{2\pi \mathit{AR}}{2 + \sqrt{\mathit{AR}^2 + 4}}. \tag{2-8}$$

Since the integration of forces happens along both the x_c axis and z_c axis, the effective CP and the torques can be calculated by multiplying the force from Equation 2-7 with the chordwise and spanwise locations of each infinitesimal square. Note that if the pitching axis would coincide with the chord center, the resultant rotational force would be zero while the rotational torques would be nonzero. Due to this fact, the purely rotational term is oftentimes omitted in the quasi-steady aerodynamic models from literature, but the work by Wang et al. [47] proves that taking this term into account leads to more accurate aerodynamic load prediction. Therefore it was decided to take this term into account.

2-3-4 Coupling Loads

Experimental research by Sane & Dickinson [42] has shown that adding the earlier described translational and rotational load terms, gives an insufficient representation of the aerodynamic loads on a flapping wing. This is due to nonlinearities that are introduced by fluid-wing interactions during simultaneous translation and rotation of the flapping wing. The derivation of this term was described in-depth in the work by Wang et al. [47], and leads to the following formulation of the coupling force:

$$F_{y_c}^{\text{coupl}} = \begin{cases} \pi\rho^{\text{f}}\omega_{x_c}\left[\int_0^R\left(\frac{3}{4}-\hat{d}\right)c^2(-v_{p_{z_c}})dx_c+\int_0^R\frac{1}{4}c^2x_cdx_c\right], & v_{p_{z_c}}\geq 0 \\ \pi\rho^{\text{f}}\omega_{x_c}\left[\int_0^R\left(\hat{d}-\frac{1}{4}\right)c^2(-v_{p_{z_c}})dx_c+\int_0^R\frac{1}{4}c^2x_cdx_c\right], & v_{p_{z_c}}<0. \end{cases} \tag{2-9}$$

Again, due to integration along the x_c axis of the wing, the torque along the z_c axis of the wing can be calculated by multiplying the force on each wing strip with the spanwise location of each wing strip. For the torque calculation around the x_c axis, the chordwise effective CP is required for each wing strip. For the case where $v_{p_{z_c}} \geq 0$, the first term of $F_{y_c}^{\text{coupl}}$ is associated with an effective CP at a 1/4 chord, whereas the second term of $F_{y_c}^{\text{coupl}}$ is associated with an effective CP at the 3/4 chord. To find the average chordwise effective CP per strip, a force-weighted average of these individual needs to be taken. For the case where $v_{p_{z_c}} < 0$, the chordwise locations for the effective CPs switch, due to switching of the TE and LE as a consequence of the sign switch of v_{pz_c} .

2-3-5 Added-Mass Loads

Due to the inherently unsteady behaviour of the flapping-wing motion, the wing accelerates and decelerates with each half stroke and the surrounding fluid accelerates and decelerates with it. The accelerating and decelerating fluid applies a reaction force on the wings, of which the influence is most apparent in the stroke reversal phase of the flapping motion. These reaction forces are referred to as the added-mass loads and can be calculated as follows:

$$F_{y_c}^{\text{am}} = -\frac{\pi}{4}\rho^{\text{f}}\int_0^R c^2\left[\,a_{y_c}+c\,(1/2-\hat{d_0})\,\alpha_{x_c}\right]dx_c, \tag{2-10}$$

with a_{y_c} the linear acceleration in y_c direction and α_{x_c} the rotational acceleration around the x_c axis. The torque around the z_c axis is found by integrating along the wing span, whereas the calculation of the torque around the x_c axis is more cumbersome. As clearly shown in Eq. 2-10, the added-mass force calculation consists of two components. The first component (depending on linear acceleration) is associated with an effective CP at the half chord and the second component (depending on the rotational acceleration) is associated with an effective CP at the $(9-16\hat{d})/(16-32\hat{d})$ chord. Multiplication of the force terms with these effective CPs, gives the torque around the x_c axis that is generated by each wing strip.

Chapter 3

Kinematic Analysis

To calculate the aerodynamic forces according to the model from chapter 2, the local kinematics of each point on the wing with respect to the surrounding air needs to be known. Therefore, the kinematics of the wing must be properly described. Since the motion of the wing is influenced by body motions and hinge motions as well, a formulation is necessary that converts these effects into kinematic contributions in terms of the local kinematics of each point on the wing. Such a formulation is made in this work, and will be discussed in this chapter as follows. Firstly, the basic principles and definitions of the kinematic model are formulated in section 3-1, after which the kinematic analysis steps that take all kinematic components (vehicle displacement and rotation, hinge displacement, wing rotation and wind effects) into account, are shown in section 3-2. Finally, the chapter is concluded in section 3-3.

3-1 Kinematic Formulations

This section discusses the kinematic formulations that are used to describe the motion of a flapping-wing vehicle and its wings. Firstly, the general formulations of the kinematics are discussed in section 3-1-1 along with the notation conventions for the kinematic analysis, which are presented in section 3-1-2. From these basic formulations, the description of the flapping-wing reference frames and vehicle reference frames follow in sections 3-1-3 and 3-1-4, respectively.

3-1-1 General formulations

Flapping wing vehicles generally consist of three substructures: the main body, the wings and the wing drive mechanism.
The main body usually contains the actuator, power source, power electronics and sensors. Therefore the largest share of the weight budget of Flapping-Wing Air Vehicle (FWAV) goes to the main body.

The wings consist of at least two spars (one in the spanwise direction and one in the chordwise direction) with a thin membrane spanning between the spars, creating a surface that is subjected to aerodynamic forces when it moves through a fluid. Even though the wings have relatively low weight compared to the main body, they need to produce the lift force to keep the complete vehicle aloft.
Lastly, wing drive mechanism is the connection between the main body and the wings, translating the forces and motions produced by the actuator into wing motion.

In order to perform aerodynamic and kinematic analysis for flapping-wing vehicles in a general manner, the vehicle's substructures are formulated as follows. The main body is modeled as a solid rigid body, which can rotate with respect to its surroundings. The wings are modeled as rigid plates with a pre-defined morphology, of which the general parameters were defined in section 2-2. The wing drive mechanism is not explicitly included in the model. Instead, the flapping wings are connected to the main body by rotational hinges with three rotational Degrees of Freedom (DOFs) where the time-dependent angular description of each DOF can be defined individually. The stiffness can be adjusted in such a way that it resembles the specific wing drive mechanism of the vehicle. Depending on the type of drive mechanism that needs to be modeled, the wing hinge is either fixed to the body or has translational degrees of freedom as well.

It should be noted that the attitude control system, the subsystem of interest in this study, is not treated as a separate subsystem. This is due to the fact that for tailless flapping-wing vehicles, the attitude control mechanism is integrated within either the main body, the wing drive mechanism, the wings or a combination of these three. Furthermore, both attitude control mechanisms that are investigated in this work (variation of stroke amplitude and pitching hinge stiffness), can be incorporated in the presented kinematic formulation. Section 5-2 shows a more detailed description of the implementation of the attitude control mechanisms into the model.

The formulation above leaves two separate bodies, the vehicle main body and flapping wings, which are connected via hinges at the wing base. Similar to the aerodynamic formulations in chapter 2, it would be desired to have a kinematic model with low computational effort. A Multi-Body Dynamic model with mostly predefined kinematic formulations provides an elegant solution for the kinematic model, since it allows for analytical formulation of the kinematics. If necessary, external loads can be taken into account in an iterative manner.

The formulation that is described above means that the following assumptions and simplifications are done for this kinematic analysis of the Atalanta:

- The main body is a rigid body of which the body-fixed inertia does not change over time.
- The wing is modeled as a rigid plate, meaning that bending of the flapping wing membrane and wing spars is not taken into account.
- Motion of the wing hinge due to deformations within the driving mechanism of the body can be taken into account if desired.
- Motion of the wing hinge with respect to the body's **CoM!** (**CoM!**) can be taken into account. This could be desired for compliant FWAV with non-stationary hinges, such as the Atalanta.

- As mentioned in chapter 2, all kinematics of the vehicle are pre-defined and imposed on the vehicle, except for the passive pitching motion of the wing. This means that the aerodynamic forces that are calculated in this model, will not affect any of the imposed motions, except for the passive pitching motion of the wing.

A combination of this kinematic model and aerodynamic model from chapter 2, gives a formulation for the aerodynamic forces on the wing. Moreover, it presents the possibility to transform these local wing forces to forces and torques on the body, so that eventually the motion of the vehicle in 3D space can be formulated. The necessary notation conventions and different reference frames will be presented in the following sections.

3-1-2 Notation Conventions

In order to compactly describe all vectors in the different reference frames, the following notation conventions will be used. In this section, a position vector is used as an example, though the notation is used for any kind of vector in the rest of this work.

In the notation of the variables and vectors below, the superscripts before a vector refer to the reference frame in which a vector is defined. If a single subscript is used, it means that the vector concerns the state of a certain point with respect to the origin of the reference frame in which it is defined. If a double subscript with two factorized terms is used, the vector defines the state of a point with respect to another point. For instance, the vector ${}^{b}\mathbf{x}_{p}$ is the position of point p in the b reference frame with respect to the origin of the b reference frame, and ${}^{G}\dot{\mathbf{x}}_{p/I}$ is the relative velocity of point p with respect to point I in the G reference frame. The definition of rotation matrices in the equations is defined similar to the definitions by Vallery and Schwab [44], which means that capital bold letters refer to rotation matrices and rotation matrix ${}^{G}\mathbf{R}_{b}$ transforms an example position vector ${}^{b}\mathbf{x}_{a}$ from the b reference frame to the G reference frame as follows in Equation 3-1:

$$ {}^{G}\mathbf{x}_{a} = {}^{G}\mathbf{R}_{b}\,{}^{b}\mathbf{x}_{a}. \tag{3-1} $$

The actual meaning of the sub- and superscripts like the previously used G, b and I, will be explained in the next sections.

3-1-3 Flapping Wing Reference Frames

First, it should be noted that all reference frames (including the frames that will be defined later in this report) are defined using the right-hand rule convention.
For now, the assumption is made that the wing is fixed to the body at the wing hinge, which is stationary. Translational DOFs of the hinge are neglected for now in the reference frame definition, and will be introduced later in section 3-2. Hence, the kinematics of a flapping wing can be fully described by using the three Euler angles of the wing with respect to the wing hinge. In order of succession, these angles are the sweeping angle (ϕ), the heaving angle (θ) and the pitching angle (η). The angles that are used to describe the flapping wing kinematics are visualized by the 'cans in series' method [43], as shown in Figure 3-1, and the corresponding reference frames will be discussed here.

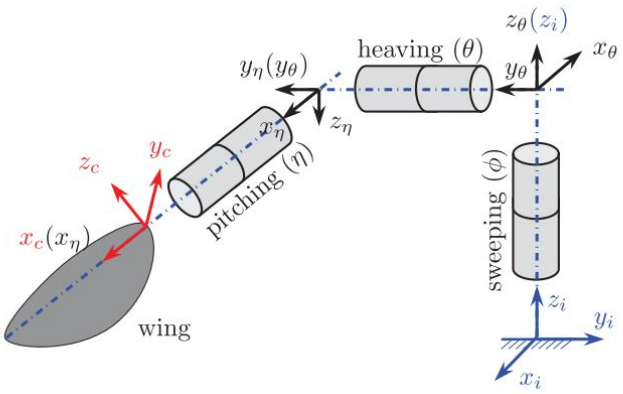

Figure 3-1: Visualization of the angles that are used to describe the flapping wing kinematics by the 'cans in series' method [43]. Four different reference frames (the inertial frame, two intermediate frames and the corotating frame) are used in this description. All four reference frames share the same origin. Courtesy of [47].

Firstly, the inertial frame $[x_i, y_i, z_i]$, which is fixed to the body at the wing hinge. It is important to note that the stroke plane of the wing is defined by the x_i and y_i axes, while the z_i axis is perpendicular to the stroke plane. As mentioned, the first rotation is the sweeping angle ϕ which rotates around the z_i axis and results in the intermediate frame $[x_\theta, y_\theta, z_\theta]$. The heaving motion (or the out of plane motion, since it is the deviation from the stroke plane) is defined as the rotation around axis y_θ and leads to the second intermediate frame $[x_\eta, y_\eta, z_\eta]$. The last transformation is defined by the pitching rotation around the x_η axis. This results in the final reference frame, the corotating frame $[x_c, y_c, z_c]$ which is fixed to the wing and rotates with it along all three rotational coordinates. For clear understanding of the direction of the axes with respect to the wing: the x_c axis coincides with the pitching axis and is aligned with the direction of the wing span, the z_c axis coincides with the wing surface and is aligned with the direction of the wing chord and lastly, the direction of the y_c axis is perpendicular to the wing surface.
In order to perform kinematic analysis according to these definitions, it is necessary to define rotation matrices that each correspond to a rotation about a specific Euler angle. The rotation matrices for the sweeping, heaving and pitching motion of the wing, respectively, are defined as follows:

$$\begin{aligned}
\mathbf{R}_\phi &= \begin{bmatrix} \cos\phi & -\sin\phi & 0 \\ \sin\phi & \cos\phi & 0 \\ 0 & 0 & 1 \end{bmatrix}, \\
\mathbf{R}_\theta &= \begin{bmatrix} \cos\theta & 0 & \sin\theta \\ 0 & 1 & 0 \\ -\sin\theta & 0 & \cos\theta \end{bmatrix}, \\
\mathbf{R}_\eta &= \begin{bmatrix} 1 & 0 & 0 \\ 0 & \cos\eta & -\sin\eta \\ 0 & \sin\eta & \cos\eta \end{bmatrix}.
\end{aligned} \tag{3-2}$$

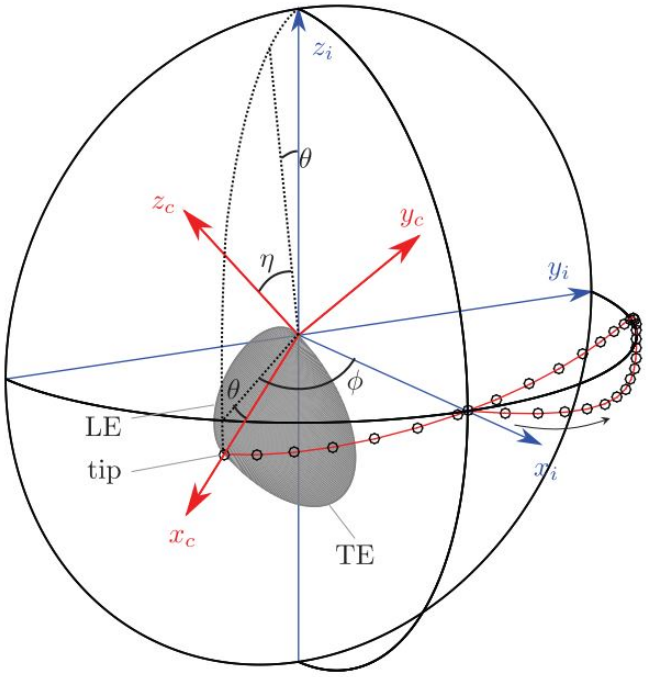

Figure 3-2: Visualization of the flapping-wing motion using the three Euler angles. The inertial frame $[x_i, y_i, z_i]$ is fixed to the origin while the corotating frame $[x_c, y_c, z_c]$ is fixed to the wing and rotates with it. The x_i and y_i axes span the stroke plane, and the black circles show the wing tip trajectory, which slightly deviate from the stroke plane following a "∞" shape in this example. The angles ϕ, θ and η represent the sweeping, heaving and pitching angle, respectively. The grey area shows the wing's surface with a distinction between the trailing edge (TE) and leading edge (LE). Courtesy of [47].

If a certain point a on the wing with position vector in the corotating frame ${}^{c}\mathbf{x}_a$ needs to be defined in the body-fixed frame (which is written as ${}^{b}\mathbf{x}_a$), the rotation matrices from Equation 3-2 can be used as follows:

$$ {}^{b}\mathbf{x}_a = {}^{b}\mathbf{R}_c \, {}^{c}\mathbf{x}_a = \mathbf{R}_\phi \mathbf{R}_\theta \mathbf{R}_\eta \, {}^{c}\mathbf{x}_a. \tag{3-3} $$

To make Equations 3-2 and 3-3 more insightful, an example of a random orientation of a flapping wing is shown in Figure 3-2, visualizing the Euler angles and the inertial and corotating reference frames. Figure 3-2 only shows the position of the wing in terms of the corotating reference frame and the inertial reference frame, meaning that the intermediate reference frames $[x_\theta, y_\theta, z_\theta]$ and $[x_\eta, y_\eta, z_\eta]$ are only used in the analysis steps and serve no further purpose in the results of the kinematic analysis.

3-1-4 Vehicle Reference Frames

The motion of the flapping-wing vehicle in 3D space can be modeled by six DOFs: three translations and three rotations. In order to model the effect of attitude control on the motion and orientation of the vehicle with respect to its surroundings, the distinction is made

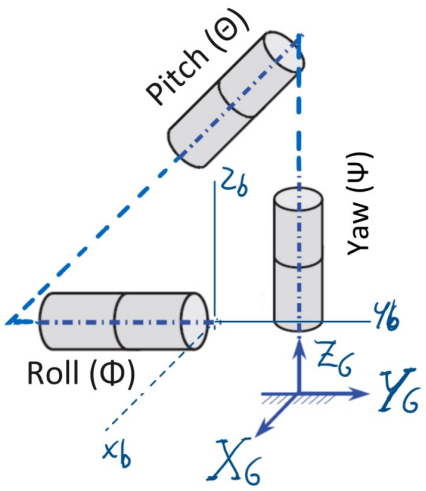

Figure 3-3: Yaw-Pitch-Roll angles that define the rotation of the body-fixed frame *b* with respect to the global frame *G*, as described by the 'cans-in-series' method [44]. The implementation that is shown is specifically designed for this work.

between two reference frames: the global reference frame $[X_G, Y_G, Z_G]$ which is fixed to the world and does not rotate, and the body-fixed reference frame $[x_b, y_b, z_b]$ which is fixed to the center of gravity (CoG) of the vehicle and of which the axes are aligned with those of the inertial frame $[x_i, y_i, z_i]$. The orientation of the body with respect to the global reference frame can be described by the use of the three subsequent rotations around the three axes of rotation of the body, using the formulation of the Euler angles as defined by Schwab et al. [43], which was used in the previous section as well.

The Euler angles of the flapping-wing vehicle are defined as in the Yaw-Pitch-Roll formulation by Vallery and Schwab [44] where angle Θ is the pitching angle around the X_G axis, angle Φ is the roll angle around the Y_G axis and angle Ψ is the yaw angle around the Z_G axis. When all body rotation angles are zero, the global axes X_G, Y_G and Z_G are aligned with the body-fixed axes x_b, y_b and z_b, respectively. A visual representation of these rotations is given in Figure 3-3.
In order to use the Yaw-Pitch-Roll rotations in the kinematic analysis, it is necessary to formulate the respective rotation matrices corresponding to each Euler angle. This was done in a similar manner to the previous section, hence the rotation matrices are defined as follows:

$$\begin{aligned}
\mathbf{R}_\Psi &= \begin{bmatrix} \cos\Psi & -\sin\Psi & 0 \\ \sin\Psi & \cos\Psi & 0 \\ 0 & 0 & 1 \end{bmatrix}, \\
\mathbf{R}_\Phi &= \begin{bmatrix} \cos\Phi & 0 & \sin\Phi \\ 0 & 1 & 0 \\ -\sin\Phi & 0 & \cos\Phi \end{bmatrix}, \\
\mathbf{R}_\Theta &= \begin{bmatrix} 1 & 0 & 0 \\ 0 & \cos\Theta & -\sin\Theta \\ 0 & \sin\Theta & \cos\Theta \end{bmatrix}.
\end{aligned} \tag{3-4}$$

In order to rotate an example position vector of point a, ${}^{b}\mathbf{x}_a$ (initially defined in the b-frame), from the body-fixed frame to the global reference frame, resulting in ${}^{G}\mathbf{x}_a$, the rotation matrices are defined in the following manner:

$$ {}^{G}\mathbf{x}_a = {}^{G}\mathbf{R}_b {}^{b}\mathbf{x}_a = \mathbf{R}_\Psi \mathbf{R}_\Theta \mathbf{R}_\Phi {}^{b}\mathbf{x}_a. \tag{3-5} $$

If the vector that describes the position of point a is initially defined in the corotating frame (${}^{c}\mathbf{x}_a$) and needs to be defined in terms of the global frame, Equations 3-3 and 3-5 can be combined as follows:

$$ {}^{G}\mathbf{x}_a = {}^{G}\mathbf{R}_b {}^{b}\mathbf{R}_c {}^{c}\mathbf{x}_a = \mathbf{R}_\Psi \mathbf{R}_\Theta \mathbf{R}_\Phi \mathbf{R}_\phi \mathbf{R}_\theta \mathbf{R}_\eta {}^{c}\mathbf{x}_a. \tag{3-6} $$

3-2 Kinematic Analysis

As defined in chapter 2, the aerodynamic forces on the wing are calculated by using the kinematic information of the wing, which is defined in the corotating frame. In this proposed model, not all kinematic components that are taken into account are initially defined in the corotating frame. Therefore it is necessary to define the components that are taken into account in a consistent way, starting with the global reference frame, while taking all the necessary reference frame transformations into account.

3-2-1 Position Definition

In order to build up the velocity definitions in a consistent way, the wing kinematic analysis is done by investigating the motion of a random point p on the flapping wing. A formulation has to be defined so that it can describe any combination of orientations of the body and the wing. Since the orientation of the body and the wing have to be taken into account, the point p is initially defined in the most general frame: the global frame $[X_G, Y_G, Z_G]$. From this frame, the first and second time derivatives of the position of p will be taken in the next sections.

In the global frame, the position of p relative to the global frame origin G is built up out of three components:

- ${}^{G}\mathbf{x}_B$: the position of the vehicle's CoM B relative to the origin G of the global reference frame. At every time instance, the position of B and G is the same, though the orientation of the vehicle might differ from the orientation of the global reference frame. Moreover, the instantaneous linear and rotational velocities of point B might not be equal to zero. This relative position is defined in the global reference frame.
- ${}^{G}\mathbf{x}_{I/B}$: the position of the wing hinge point I relative to the vehicle's CoM B, of which the latter is the origin of the body-fixed reference frame b. This relative position is defined in the global reference frame.

- ${}^{G}\mathbf{x}_{p/I}$: the position of point p on the wing, relative to the wing hinge point I. Point I is the origin of both the inertial reference frame i and the corotating reference frame c, though both reference frames are rotated with respect to each other. Note that this relative position is defined in the global reference frame as well.

Hence, the position of point p in the global frame is defined by Equation 3-7:

$$ {}^{G}\mathbf{x}_{p} = {}^{G}\mathbf{x}_{B} + {}^{G}\mathbf{x}_{I/B} + {}^{G}\mathbf{x}_{p/I}. \tag{3-7} $$

The position of point p is defined using three separate components, since it facilitates a concise manner of velocity and acceleration analysis. How this is done exactly, will be shown in the following sections.

3-2-2 Velocity Definition

For the velocity definition, the analysis for calculating the linear velocity is slightly different from the calculation of the angular velocity. Therefore, these two velocity components will be derived separately in this section.

Linear velocity

To calculate the velocity of point p in the global frame, the time derivative of Equation 3-7 must be taken. Before the time derivative is taken, Equation 3-7 should be rewritten in such a way that the rotational velocities that contribute to the motion of point p are visible in the equation. Therefore, each of the three terms in Equation 3-7 must be written in terms of the reference frames in which they were originally defined and the rotation matrices to transform them back to the global reference frame. Hence, Equation 3-7 is rewritten as follows:

$$ {}^{G}\mathbf{x}_{p} = {}^{G}\mathbf{x}_{B} + {}^{G}\mathbf{R}_{b}{}^{b}\mathbf{x}_{I/B} + {}^{G}\mathbf{R}_{b}{}^{b}\mathbf{R}_{c}{}^{c}\mathbf{x}_{p/I}. \tag{3-8} $$

Since the position of point p has now been written out in terms of all the original coordinates and rotation matrices, it is possible to take the time derivative without overlooking any velocity contributions. By using the definition in Equation 3-8, the velocity of point p is defined by the following equation:

$$ \frac{d({}^{G}\mathbf{x}_{p})}{dt} = \frac{d({}^{G}\mathbf{x}_{B})}{dt} + \frac{d({}^{G}\mathbf{R}_{b}{}^{b}\mathbf{x}_{I/B})}{dt} + \frac{d({}^{G}\mathbf{R}_{b}{}^{b}\mathbf{R}_{c}{}^{c}\mathbf{x}_{p/I})}{dt}. \tag{3-9} $$

Writing out the derivative terms in Equation 3-9 leads to Equation 3-10, which is eventually used for the calculation of the velocity of point p. The equation is formulated as follows:

$$ {}^{G}\dot{\mathbf{x}}_{p} = {}^{G}\dot{\mathbf{x}}_{B} + {}^{G}\dot{\mathbf{R}}_{b}{}^{b}\mathbf{x}_{I/B} + {}^{G}\mathbf{R}_{b}{}^{b}\dot{\mathbf{x}}_{I/B} + {}^{G}\dot{\mathbf{R}}_{b}{}^{b}\mathbf{R}_{c}{}^{c}\mathbf{x}_{p/I} + {}^{G}\mathbf{R}_{b}{}^{b}\dot{\mathbf{R}}_{c}{}^{c}\mathbf{x}_{p/I} + {}^{G}\mathbf{R}_{b}{}^{b}\mathbf{R}_{c}{}^{c}\dot{\mathbf{x}}_{p/I}. \tag{3-10} $$

Since Equation 3-10 contains a lot of terms, a few reordering steps are required after which the equation will make more sense intuitively. Firstly, the term ${}^{G}\mathbf{R}_{b}{}^{b}\mathbf{R}_{c}{}^{c}\dot{\mathbf{x}}_{p/I}$, which is defined as the velocity of point p due to motion of point p on the wing in the corotating frame, can be neglected. This is due to point p being a stationary point on the wing. Hence, the velocity of point p with respect to point I in the corotating reference frame will be equal to zero. The other terms are all nonzero and after reordering those terms, the final equation for the velocity of point p in the global reference frame becomes:

$$ {}^{G}\dot{\mathbf{x}}_{p} = {}^{G}\dot{\mathbf{x}}_{B} + {}^{G}\mathbf{R}_{b}{}^{b}\dot{\mathbf{x}}_{I/B} + {}^{G}\dot{\mathbf{R}}_{b}{}^{b}\mathbf{x}_{I/B} + {}^{G}\dot{\mathbf{R}}_{b}{}^{b}\mathbf{R}_{c}{}^{c}\mathbf{x}_{p/I} + {}^{G}\mathbf{R}_{b}{}^{b}\dot{\mathbf{R}}_{c}{}^{c}\mathbf{x}_{p/I}. \tag{3-11} $$

The terms in Equation 3-11 can be physically interpreted as follows (all terms are defined with respect to the global reference frame):

- ${}^{G}\dot{\mathbf{x}}_{B}$ is defined as the linear velocity of point B, due to linear motion of the vehicle through space.
- ${}^{G}\mathbf{R}_{b}{}^{b}\dot{\mathbf{x}}_{I/B}$ is defined as the motion of hinge point I with respect to the CoM B of the vehicle. This term would be zero if the wing hinge position was fixed in all types of flapping-wing vehicles, but since the Atalanta has flexible hinges which are non-stationary, it was decided to incorporate this term in the proposed model.
- ${}^{G}\dot{\mathbf{R}}_{b}{}^{b}\mathbf{x}_{I/B} + {}^{G}\dot{\mathbf{R}}_{b}{}^{b}\mathbf{R}_{c}{}^{c}\mathbf{x}_{p/I}$ is defined as the velocity of point p with due to rotation of the vehicle body. This term consists out of two components, the velocity of point I relative to point B and the velocity of point p relative to point I. Adding these up gives the velocity of point p relative to point B in the global reference frame, due to rotation of the vehicle body.
- ${}^{G}\mathbf{R}_{b}{}^{b}\dot{\mathbf{R}}_{c}{}^{c}\mathbf{x}_{p/I}$ is defined as the velocity of point p due to rotations of the wing. In previous quasi-steady models, for instance the model that was developed by Qi Wang [47], this is the only velocity term that is taken into account since in most models the vehicle is assumed to be stationary with a wing hinge that does not move with respect to the vehicle body.

The previously discussed terms are all linear velocity terms that originate from motion of the body, whereas velocity terms can be imposed by the environment as well in the form of wind. Since wind has an influence on the velocity of point p with respect to the surrounding air, a wind velocity term has to be added to Equation 3-11, which is the wind term defined in the global frame: ${}^{G}\mathbf{q}$.

So the final equation with all velocity factors taken into account is given in Equation 3-12 below:

$$ {}^{G}\dot{\mathbf{x}}_{p} = {}^{G}\dot{\mathbf{x}}_{B} + {}^{G}\mathbf{R}_{b}{}^{b}\dot{\mathbf{x}}_{I/B} + \underbrace{{}^{G}\dot{\mathbf{R}}_{b}{}^{b}\mathbf{x}_{I/B} + {}^{G}\dot{\mathbf{R}}_{b}{}^{b}\mathbf{R}_{c}{}^{c}\mathbf{x}_{p/I}}_{\text{velocity due to body rotation}} + {}^{G}\mathbf{R}_{b}{}^{b}\dot{\mathbf{R}}_{c}{}^{c}\mathbf{x}_{p/I} + {}^{G}\mathbf{q}. \tag{3-12} $$

Equation 3-12 shows all linear velocity contributions in terms of the position coordinates in their original reference frames and the corresponding rotation matrices or time derivatives

thereof. In vector analysis, time derivatives of rotation matrices cannot be directly used to compute the linear velocity vectors of point p. Hence, a method proposed by Vallery and Schwab [44] was used to convert the time derivatives of rotation matrices to rotational velocity vectors. Understanding this conversion of parameters is important for grasping the difference between time derivatives of rotation matrices, rate of change of Euler angles and angular velocities of bodies in different reference frames. The mathematical steps to perform this conversion are discussed in Appendix A, which leads to the following definition for the time derivative of an example rotation matrix ${}^{G}\dot{\mathbf{R}}_{b}$:

$$ {}^{G}\dot{\mathbf{R}}_{b}\,{}^{b}\mathbf{x}_{I/B} = {}^{G}\boldsymbol{\omega}_{B} \times {}^{G}\mathbf{x}_{I/B}. \tag{3-13} $$

Equation 3-13 shows that, for example, the term that defines the velocity of point I with respect to vehicle body's Center of Gravity (CoG) B, ${}^{G}\dot{\mathbf{R}}_{b}\,{}^{b}\mathbf{x}_{I/B}$ can be rewritten as the cross product between the angular velocity of vehicle body B in the global frame and the position of I relative to B in the global frame. Similar to the method shown in Equation 3-13, other velocity terms that contain time derivatives of rotation matrices can be rewritten in terms of angular velocity vectors as well. This results in the following rewritten equation for the linear motion of point p in the global frame:

$$ {}^{G}\dot{\mathbf{x}}_{p} = {}^{G}\dot{\mathbf{x}}_{B} + {}^{G}\mathbf{R}_{b}\,{}^{b}\dot{\mathbf{x}}_{I/B} + \underbrace{{}^{G}\boldsymbol{\omega}_{B} \times {}^{G}\mathbf{x}_{I/B} + {}^{G}\boldsymbol{\omega}_{B} \times {}^{G}\mathbf{x}_{p/I}}_{\text{velocity due to body rotation}} + {}^{G}\mathbf{R}_{b}({}^{b}\boldsymbol{\omega}_{W} \times {}^{b}\mathbf{x}_{p/I}) + {}^{G}\mathbf{q}. \tag{3-14} $$

Equation 3-14 clearly shows that the time derivatives of the rotation matrices are now replaced by ${}^{G}\boldsymbol{\omega}_{B}$ which is the rotational velocity of the vehicle body in the global reference frame and ${}^{b}\boldsymbol{\omega}_{W}$ which is the rotational velocity of the wing W in the body-fixed reference frame. Both are multiplied with the position vectors of the corresponding points using a cross product.

The total velocity vector of point p has so far been defined in the global reference frame, but the aerodynamic formulation in this work requires the velocity vector of point p to be defined in the corotating reference frame. Since ${}^{G}\dot{\mathbf{x}}_{p}$ is a linear velocity vector, the linear velocity in the corotating frame can simply be found by two reference frame rotations as follows:

$$ {}^{c}\dot{\mathbf{x}}_{p} = {}^{c}\mathbf{R}_{b}\,{}^{b}\mathbf{R}_{G}\,{}^{G}\dot{\mathbf{x}}_{p}. \tag{3-15} $$

Equation 3-15 gives the local velocity vector, which defines the velocity in the corotating frame of any point p on the wing, as long as the rotational velocities of the body and the wing are known. The velocity of points on the wing in the corotating frame, can be used to calculate the aerodynamic forces on the wing, as defined in chapter 2.

Angular Velocity

As suggested in the linear velocity equation that was defined earlier, Equation 3-14, there are two rotational velocity components that have to be taken into account: the rotational velocity of body B and the rotational velocity of the wing W. Since all relative angles and rotational velocities are known, and the different reference frames are initially aligned when all angles

are zero, a total formulation for the rotational velocity of the wing body in the corotating frame can be defined, which takes both the body and wing rotational velocity into account. In other words, this is the rotational velocity of the wing W with respect to the origin G of the global reference frame, defined in the corotating reference frame. This rotational velocity term is defined as ${}^{c}\boldsymbol{\omega}_{W/G}$.

Following the method that was presented in appendix section A-2, the formulation for the total wing rotational velocity is as follows:

$$ {}^{c}\boldsymbol{\omega}_{W/G} = \dot{\boldsymbol{\eta}} + \mathbf{R}_{\eta}^{T}\dot{\boldsymbol{\theta}} + \mathbf{R}_{\eta}^{T}\mathbf{R}_{\theta}^{T}\dot{\boldsymbol{\phi}} + \mathbf{R}_{\eta}^{T}\mathbf{R}_{\theta}^{T}\mathbf{R}_{\phi}^{T}\dot{\boldsymbol{\Phi}} + \mathbf{R}_{\eta}^{T}\mathbf{R}_{\theta}^{T}\mathbf{R}_{\phi}^{T}\mathbf{R}_{\Phi}^{T}\dot{\boldsymbol{\Theta}} + \mathbf{R}_{\eta}^{T}\mathbf{R}_{\theta}^{T}\mathbf{R}_{\phi}^{T}\mathbf{R}_{\Phi}^{T}\mathbf{R}_{\Theta}\dot{\boldsymbol{\Psi}}. \quad (3\text{-}16) $$

The complete symbolic expression that results from Equation 3-16, is shown in appendix section B-1. Since the expression in Equation 3-16 contains all 6 rotational velocities and reference frame transformations, it would be tempting to assume that this single rotational velocity expression can be used to formulate the linear velocity of point p on the wing. However, since the point G (the origin of the body rotation) and point I (the origin of the wing rotation) are not located at the same point in space, the rotational velocity does not contain all the required information to compute the linear velocity of point p. Hence, the proposed solution is to use the expression in Equation 3-14 as the linear velocity inputs and the expression in Equation 3-16 as the rotational velocity inputs for the aerodynamic model. Which velocity terms are exactly required, was described in chapter 2.

The velocity profile of the wing and local angular velocity of the wing is not sufficient for the full aerodynamic analysis of the wing, since the accelerations are required as well. The acceleration expressions will be derived in the next section.

3-2-3 Acceleration Definition

Similar to the linear and angular velocity terms, the linear and angular components of the accelerations are calculated separately. Therefore, the angular and linear accelerations will be discussed separately in this section as well.

Linear Acceleration

In order to define the accelerations in a concise way, the time derivative of the linear velocity definition of point p on the wing as described in Equation 3-14 should be taken. This results in the following equation:

$$ \begin{aligned} \frac{d({}^{G}\dot{\mathbf{x}}_p)}{dt} = &\underbrace{\frac{d({}^{G}\dot{\mathbf{x}}_B)}{dt}}_{1} + \underbrace{\frac{d({}^{G}\mathbf{R}_b\,{}^{b}\dot{\mathbf{x}}_{I/B})}{dt}}_{2} + \underbrace{\frac{d({}^{G}\boldsymbol{\omega}_B \times {}^{G}\mathbf{x}_{I/B} + {}^{G}\boldsymbol{\omega}_B \times {}^{G}\mathbf{x}_{p/I})}{dt}}_{3} + \\ &\underbrace{\frac{d({}^{G}\mathbf{R}_b({}^{b}\boldsymbol{\omega}_W \times {}^{b}\mathbf{x}_{p/I}))}{dt}}_{4} + \underbrace{\frac{d({}^{G}\mathbf{q})}{dt}}_{5}. \end{aligned} \quad (3\text{-}17) $$

Since the second time derivatives are not written out yet, Equation 3-17 shows the same amount of terms as Equation 3-14. For a practical insight into which acceleration terms originally correspond to which velocity terms, the compact acceleration terms in Equation 3-17 have been numbered in such a way that they correspond with the respective velocity terms given in Equation 3-14. Writing out the second time derivatives, with the numbers underneath the terms being associated to the same terms as in Equation 3-17, gives the following equation for the acceleration of point p in the global frame:

$$\begin{aligned}
{}^G\ddot{\mathbf{x}}_p = &\underbrace{{}^G\ddot{\mathbf{x}}_B}_{1} + \underbrace{{}^G\dot{\mathbf{R}}_b\,{}^b\dot{\mathbf{x}}_{I/B} + {}^G\mathbf{R}_b\,{}^b\ddot{\mathbf{x}}_{I/B}}_{2} + \\
&\underbrace{{}^G\dot{\boldsymbol{\omega}}_B \times {}^G\mathbf{x}_{I/B} + {}^G\boldsymbol{\omega}_B \times {}^G\dot{\mathbf{x}}_{I/B} + {}^G\dot{\boldsymbol{\omega}}_B \times {}^G\mathbf{x}_{p/I} + {}^G\boldsymbol{\omega}_B \times {}^G\dot{\mathbf{x}}_{p/I}}_{3} + \\
&\underbrace{{}^G\dot{\mathbf{R}}_b({}^b\boldsymbol{\omega}_W \times {}^b\mathbf{x}_{p/I}) + {}^G\mathbf{R}_b({}^b\dot{\boldsymbol{\omega}}_W \times {}^b\mathbf{x}_{p/I}) + {}^G\mathbf{R}_b({}^b\boldsymbol{\omega}_W \times {}^b\dot{\mathbf{x}}_{p/I})}_{4} + \\
&\underbrace{{}^G\dot{\mathbf{q}}}_{5}.
\end{aligned} \tag{3-18}$$

Each individual term of Equation 3-18 needs to be written out more explicitly to enable acceleration analysis. Since this is a rather lengthy process which mostly consists of reordering terms and writing the rotation matrix time derivatives in terms of rotational velocities (as given in appendix A), the derivation was omitted and the resulting acceleration equation is given below:

$$\begin{aligned}
{}^G\ddot{\mathbf{x}}_p = &\underbrace{{}^G\ddot{\mathbf{x}}_B}_{1} + \underbrace{{}^G\boldsymbol{\omega}_B \times ({}^G\mathbf{R}_B\,{}^b\dot{\mathbf{x}}_{I/B}) + {}^G\mathbf{R}_b\,{}^b\ddot{\mathbf{x}}_{I/B}}_{2} + \\
&\underbrace{{}^G\dot{\boldsymbol{\omega}}_B \times {}^G\mathbf{x}_{I/B} + {}^G\boldsymbol{\omega}_B \times ({}^G\boldsymbol{\omega}_B \times {}^G\mathbf{x}_{I/B}) + {}^G\boldsymbol{\omega}_B \times ({}^G\mathbf{R}_b\,{}^b\dot{\mathbf{x}}_{I/B})}_{3} + \\
&\underbrace{{}^G\dot{\boldsymbol{\omega}}_B \times {}^G\mathbf{x}_{p/I} + {}^G\boldsymbol{\omega}_B \times ({}^G\boldsymbol{\omega}_B \times {}^G\mathbf{x}_{p/I}) + {}^G\boldsymbol{\omega}_B \times ({}^G\mathbf{R}_b({}^b\boldsymbol{\omega}_W \times {}^b\mathbf{x}_{p/I}))}_{3} + \\
&\underbrace{{}^G\boldsymbol{\omega}_B \times ({}^G\mathbf{R}_b({}^b\boldsymbol{\omega}_W \times {}^b\mathbf{x}_{p/I})) + {}^G\mathbf{R}_b({}^b\dot{\boldsymbol{\omega}}_W \times {}^b\mathbf{x}_{p/I}) + {}^G\mathbf{R}_b({}^b\boldsymbol{\omega}_W \times ({}^b\boldsymbol{\omega}_W \times {}^b\mathbf{x}_{p/I}))}_{4} + \\
&\underbrace{{}^G\dot{\mathbf{q}}}_{5}.
\end{aligned} \tag{3-19}$$

Equation 3-19 shows all the relevant acceleration terms that follow from the velocity definitions in the current work. Note that the position of point p on the wing is fixed and that therefore the velocity of point p relative to wing hinge I is zero. This was defined earlier as well, but it is repeated here to account for the absence of Coriolis terms in term 4 of Equation 3-19. Since the velocity of point p in the corotating frame was defined to be zero, the acceleration terms are automatically set to zero as well and therefore they do not occur in Equation 3-18.

This equation however, can be reduced by reordering, leaving the final equation for the acceleration of point p in the global frame:

$$\begin{aligned}{}^{G}\ddot{\mathbf{x}}_p =& {}^{G}\ddot{\mathbf{x}}_B + {}^{G}\mathbf{R}_b\,{}^{b}\ddot{\mathbf{x}}_{I/B} + \\ & 2 * ({}^{G}\boldsymbol{\omega}_B \times ({}^{G}\mathbf{R}_B\,{}^{b}\dot{\mathbf{x}}_{I/B})) + {}^{G}\boldsymbol{\omega}_B \times ({}^{G}\boldsymbol{\omega}_B \times {}^{G}\mathbf{x}_{I/B}) + {}^{G}\dot{\boldsymbol{\omega}}_B \times {}^{G}\mathbf{x}_{I/B} + \\ & {}^{G}\boldsymbol{\omega}_B \times ({}^{G}\boldsymbol{\omega}_B \times {}^{G}\mathbf{x}_{p/I}) + 2 * ({}^{G}\boldsymbol{\omega}_B \times ({}^{G}\mathbf{R}_b({}^{b}\boldsymbol{\omega}_W \times {}^{b}\mathbf{x}_{p/I}))) + {}^{G}\dot{\boldsymbol{\omega}}_B \times {}^{G}\mathbf{x}_{p/I} + \\ & {}^{G}\mathbf{R}_b({}^{b}\dot{\boldsymbol{\omega}}_W \times {}^{b}\mathbf{x}_{p/I}) + {}^{G}\mathbf{R}_b({}^{b}\boldsymbol{\omega}_W \times ({}^{b}\boldsymbol{\omega}_W \times {}^{b}\mathbf{x}_{p/I})) + {}^{G}\dot{\mathbf{q}}.\end{aligned} \tag{3-20}$$

The 11 acceleration terms that are left in Equation 3-20 are interpreted as follows:

- ${}^{G}\ddot{\mathbf{x}}_B$ is the linear acceleration of point B, the CoG of the vehicle body.
- ${}^{G}\mathbf{R}_b\,{}^{b}\ddot{\mathbf{x}}_{I/B}$ is the linear acceleration of point I in the body-fixed frame due to deformations of the body.
- $2 * ({}^{G}\boldsymbol{\omega}_B \times ({}^{G}\mathbf{R}_B\,{}^{b}\dot{\mathbf{x}}_{I/B}))$ and ${}^{G}\boldsymbol{\omega}_B \times ({}^{G}\boldsymbol{\omega}_B \times {}^{G}\mathbf{x}_{I/B})$ are the Coriolis acceleration due to the combined rotation of body B and linear velocity of point I, and the centripetal acceleration due to the body rotational velocity, respectively.
- ${}^{G}\dot{\boldsymbol{\omega}}_B \times {}^{G}\mathbf{x}_{I/B}$ is the acceleration of point I due to the angular acceleration of body B.
- ${}^{G}\boldsymbol{\omega}_B \times ({}^{G}\boldsymbol{\omega}_B \times {}^{G}\mathbf{x}_{p/I})$ and $2 * ({}^{G}\boldsymbol{\omega}_B \times ({}^{G}\mathbf{R}_b({}^{b}\boldsymbol{\omega}_W \times {}^{b}\mathbf{x}_{p/I})))$ are the centripetal acceleration of point $\mathbf{p}$ due to the rotation of body B, and the Coriolis acceleration on point p due to the rotational velocity of body B and the motion of point p caused by rotational velocity of wing W, respectively.
- ${}^{G}\dot{\boldsymbol{\omega}}_B \times {}^{G}\mathbf{x}_{p/I}$ is the acceleration of point $\mathbf{p}$ due to the angular acceleration of body $\mathbf{B}$.
- ${}^{G}\mathbf{R}_b({}^{b}\dot{\boldsymbol{\omega}}_W \times {}^{b}\mathbf{x}_{p/I})$ and ${}^{G}\mathbf{R}_b({}^{b}\boldsymbol{\omega}_W \times ({}^{b}\boldsymbol{\omega}_W \times {}^{b}\mathbf{x}_{p/I}))$, are the accelerations of point p due to the angular acceleration of wing W and the centripetal acceleration due to rotational velocity of wing W.
- ${}^{G}\dot{\mathbf{q}}$ is the acceleration of the wind flow, which could, for example, originate from wind gusts.

Finally, the expression in Equation 3-20 can be defined in the corotating frame as well. Similar to the transformation of the linear velocity in Equation 3-15, the linear acceleration in the corotating frame can be computed as follows:

$${}^{c}\ddot{\mathbf{x}}_p = {}^{c}\mathbf{R}_b\,{}^{b}\mathbf{R}_G\,{}^{G}\ddot{\mathbf{x}}_p. \tag{3-21}$$

Angular Acceleration

The angular acceleration of the wing W in the corotating frame can be found by taking the time derivative of Equation 3-16. Since determination of the time derivative by hand is a rather cumbersome task, the symbolic expressions of Equation 3-16 were written in MatLab®. The 'jacobian' operator within the symbolic toolbox enables taking concise time derivatives of lengthy symbolic equations, which is the method that was used for this computation. The full equation that describes the angular acceleration vector of wing W in the corotating frame, is given in appendix section B-2.

3-3 Chapter Conclusion

To conclude, the kinematic formulations in this chapter describe the position, velocity and acceleration of any point p on the wing, in all necessary reference frames while taking all kinematic contributions (body motion, hinge motion, wing motion and wind effects) into account. At the same time, the reference frame definitions make it possible to transform the aerodynamic forces on the wings in the corotating frame to forces and torques in the body-fixed frame. The latter can subsequently be transformed to forces and torques in the global frame, so that the motion in 3D space can be analyzed. The implementation of multiple reference frames for flapping-wing analysis that includes wing motion, vehicle motion, hinge motion and wind effects is unique for the current work.

Chapter 4

Aerodynamics with Basic Kinematics

Earlier, in section 3-1-3, it was described that the kinematics of the flapping wing can be described by three Euler angles: sweeping angle ϕ, heaving angle θ and pitching angle η. The time dependent functions that describe the variation of the Euler angles, define the velocity vectors that are used in section 2-3 to calculate the aerodynamic forces that are generated by the wing. Since different descriptions of the Euler angles lead to different velocity vectors, it only makes sense that these different angle descriptions lead to different aerodynamic responses as well. In this chapter, different options for the kinematic description of the wing motion are given and the corresponding differences in aerodynamic response are shown. From these options, the most suitable combination of Euler angle descriptions is chosen for the purposes of this research. Section 4-1 describes the model setup, after which the different possible formulations for each Euler angle of the flapping motion are given in 4-2. The results that support the choices for the kinematic formulations are presented in section 4-3, after which the chapter is discussed and concluded in sections 4-4 and 4-5, respectively.

4-1 Model Setup

Since this chapter discusses which kinematic formulation is most suitable for the analysis in the current work, the criteria for a suitable formulation must be defined in more detail. As described in chapter 2, the computation of aerodynamic forces in flapping-wing aerodynamic analysis is dominated by a trade-off between model accuracy and computational efficiency. A similar trade-off was made for the mechanical modeling of the wing, as described in chapter 3. In both cases, the decision was made to use a computationally efficient model that shows the force generation of the wing in a qualitatively accurate way, such that the model is generally applicable in many cases of flapping-wing vehicle motion. The kinematic description needs to meet the same requirements, meaning that a widely applicable description that clearly shows the overall aerodynamic response of different wing designs and body motion cases is desired over a description that shows the aerodynamic responses as accurate as possible for very specific situations.

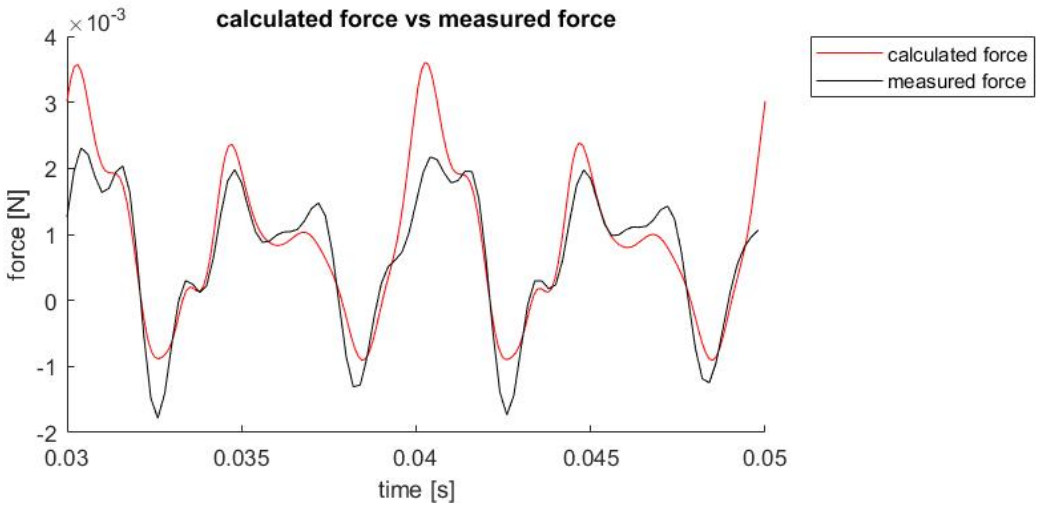

Figure 4-1: Physical measurement of aerodynamic force generated by a flapping wing, compared with the calculated aerodynamic forces generated by the same flapping wing with corresponding measured kinematics. Note that the aerodynamic response of two consecutive wing strokes is shown, starting with the downstroke.

To get an insight into the performance of predictive aerodynamic models, the 'best case scenario' for the combination of aerodynamic model and kinematic model that was used in this work is shown in Figure 4-1.

In this figure, the physical measurements of forces generated by a flapping wing are compared with the analytical aerodynamic model that is used in the current work. It is a 'best case scenario' for the performance of the analytical model, since the kinematics that are used as input of the aerodynamic model are the wing kinematics as they were measured in the aforementioned physical experiment. From this figure, it can be concluded that even this best case scenario performs quite poorly in the quantitative sense, since the instantaneous force values are quite far apart. Qualitatively, the result is close enough, since the overall force curves are the same and the average values of the lift force are of the same order of magnitude (this has also been shown in [47]). Moreover, better analytical simulations of flapping-wing aerodynamic responses have not been reported in literature, since accurate modeling of the nonlinear aerodynamic terms in flapping-wing aerodynamics is a challenge.
Note that the measured and calculated results in Figure 4-1 include the inertial forces of the wing, since these forces cannot be isolated in the physical experiment. Further graphs in this chapter will only take the aerodynamic forces into account, hence the force graphs later in this chapter may look rather different from the one in Figure 4-1. Note that the results in this figure and in the rest of this work are produced using the wing planform that mimics the wing of the Eristalis tenax (dronefly) as defined by Witney & Wood [48]. A schematic representation of this wing planform is given in Figure 4-2.

Fully measured kinematics provide an acceptable result, but since a method that is generally applicable for multiple wing morphologies, attitude control parameters and body motions is desired in the current work, it is not a valid option. Therefore, the following sections will discuss other options for flapping-wing kinematic formulations that still capture the global aerodynamic behaviour as shown in Figure 4-1, with the goal of finding a more generally

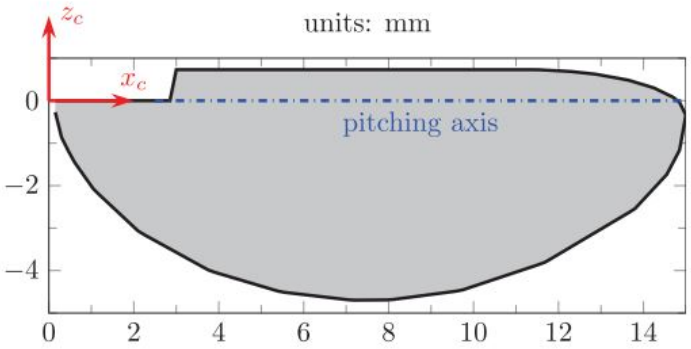

Figure 4-2: Wing planform design inspired on the dronefly wing. Design by Whitney & Wood [48], figure is the courtesy of Wang et al. [47].

applicable method compared to the measured kinematics.

4-2 Flapping-Wing Kinematic Formulations

This section discusses the different formulations that can be used to describe the time dependent Euler angles that describe the flapping motion of the wings. Since the application of the flapping-wing aerodynamics on attitude control mechanisms in this work is new, the choice for the most suitable kinematic descriptions does not follow logically form literature. Hence, a trade-off must be made on which formulation should be used for each Euler angle, as done in [19], where two different experiments within the same work required different kinematic descriptions. The different possibilities for angle formulation will be given here for each Euler angle: sweeping angle ϕ, heaving angle θ and pitching angle η.

4-2-1 Sweeping Motion

Three types of time dependent angle descriptions from literature are considered for the sweeping motion $\phi(t)$:

- Fully harmonic sweeping motion, described as

$$\phi(t) = \phi_m \sin(2\pi\, ft), \tag{4-1}$$

  where ϕ_m is the sweeping amplitude, f is the flapping frequency and t is time. This formulation is mostly chosen in models that consider vehicle motion or structure motion next to the flapping-wing aerodynamics, such as in the 6-DoF flight dynamics model by Kim et al. [19]. Hence this formulation is also used in a model where other flight states than hovering were investigated.

- A harmonic sweeping motion that can be altered using empirical parameters such as the following equation developed by Berman & Wang [1]:

$$\phi(t) = \frac{\phi_m}{\sin^{-1}(K)} \sin^{-1}[K \sin(2\pi f t)], \quad \text{where} 0 < K < 1, \tag{4-2}$$

in which $\phi(t)$ is a smooth triangular waveform. The parameter K determines the smoothness of $\phi(t)$. When K approaches zero, $\phi(t)$ becomes a sinusoid whereas it becomes a triangular wave when K approaches one. Therefore, K can be described as the measure how quickly the reversal of wing motion takes place. The value of K is empirically determined and enables tuning of the sweeping motion pattern to resemble physically measured wing motion. Moreover, parameterization of the sweeping motion can be used for optimizing the kinematics for maximum lift production at the lowest energy cost for certain wing shapes, as shown in [1].

- The sweeping motion can be determined by measurements as well. In this case, physical measurements using flapping wings are done and the sweeping angle is measured over time along with the aerodynamic forces. This method for motion description gives very accurate results when it is combined with a good predictive aerodynamic model, but this type of formulation is not useful when variations to the flapping motion need to be applied. Therefore, measured sweeping motion is mostly used for the verification of predictive aerodynamic models, since the predicted and measured aerodynamic forces are based on the same sweeping kinematics and the aerodynamic force responses can be compared fairly. This method is, for instance, used in the research into a quasi-steady aerodynamic formulation by Whitney & Wood in [48] whose research provided the necessary foundation for the work by Wang et al. [47] and the current work.
- Software can be used to model the 3D structure of the driving mechanism, to provide for a more mechanism-specific description compared to analytical formulations and to allow for a less time consuming process compared to physical measurements. This could either be done by using an Multi-Body Dynamics (MBD) description for a rigid body description of the wing drive mechanism, or a finite element method approach to model a compliant wing drive mechanism.

4-2-2 Heaving Motion

Again, three different types of heaving angle descriptions from literature are considered for the heaving motion $\theta(t)$:

- The simplest way to model the heaving motion that was found in literature, is to not take it into account at all and set it equal to zero, as done by Kim et al. [19]. This would seem like a shortcut, but since many flapping-wing mechanisms do not control the heaving motion actively and the analysis would be simplified by taking an Euler angle out of the equation. Additionally, most flapping mechanisms have a relatively high stiffness in the heaving direction (as shown in the experiments by [48]) compared to the aerodynamic forces, which makes this option worth considering.
- The heaving motion can be described by an adjusted sinusoidal oscillation, much like the sweeping motion expression in 4-2, where the expression for the heaving motion is as follows:

$$\theta(t) = \theta_m \cos(2\pi N f t + \Phi_\theta) + \theta_0, \tag{4-3}$$

where θ_m is the heaving amplitude Φ_θ is the phase offset, θ_0 is the heaving offset angle and N is a constant that is either 1 or 2. Here, $N = 1$ corresponds to one vertical oscillation per period of flapping motion and $N = 2$ corresponds to two vertical oscillations per period of flapping motion (also referred to as a 'figure 8' motion shape). This description of the heaving angle is used by Berman & Wang [1] among others, and is both used for optimization of wing kinematics and modeling of passive heave motion to match experimentally measured heaving motion.

- The heaving motion of the wing can be fully described by measurements as well, similar to the sweeping motion. Again, this would serve as a method for validation of aerodynamic models, as done by Whitney & Wood [48]. In this work, the measured heaving motion will be mostly used to decide whether it is necessary to take heaving motion into account at all.

- A passive formulation for the heaving motion, based on the aerodynamic forces produced by the wing, could provide a generally applicable formulation of heaving motion that does not depend on parameter tuning or measurements. However, literature does not report such a formulation since the contribution of sweeping and (passive) pitching motion to the aerodynamic forces is substantially larger.

4-2-3 Pitching Motion

A lot of research has been done on the passive and active pitching motion of flapping wings. Since the driving system of the Atalanta has a passive pitching mechanism [2], the methods to model active pitching motion will not be discussed, leaving three possible categories of passive pitch motion modeling:

- Approximation of passive pitch motion by analytical functions is oftentimes used in quasi-steady aerodynamic analysis of flapping wings. Both due to its low addition in computational effort and possibility to tune the pitching function, it is very suitable for 3D vehicle motion analysis as done by Kim et al. [19] and optimization of the kinematics as done by Berman & Wang [1]. Two disadvantages of this method are that the analytical formulation relies heavily on the tuning of parameters and the influence of flow induced by body motions on the passive pitch cannot be continuously taken into account.

- Again, the pitching motion can be fully measured. The advantage of this method is that the passive pitching motion can be taken into account very accurately, even when a flow is applied to the wing during the measurement. The direct disadvantage is that measurements are required for each new situation (different wing shape, actuator, flow state, sweeping/heaving patterns etc.), making this method suitable for model verification rather than a tool for describing the pitching kinematics in a 3D model.

- A passive pitching motion formulation based on the aerodynamic loads was developed in the work by Wang et al. [47], in order to find a general formulation of the passive pitching motion that only depends on the wing morphology and prescribed wing motions (sweeping and heaving, if applicable). The loads and torques on the wing as described in 2-3 are used to compute the pitching torques on the wing, from which the pitching motion is calculated over time. This method largely eliminates the dependency on parameter tuning or measurements, while giving a realistic representation of the passive pitching motion (as shown by Wang et al. [47]). Moreover, when other velocity components like body velocities or external flow velocities are integrated in the wing velocity vector from section 2-3, the influence of these additional velocity components on the passive pitching motion could be taken into account by using this description. Furthermore, this passive pitching formulation directly allows for the calculation of the influence of the pitching hinge stiffness (k_η) on the pitching kinematics of the wing. Therefore, this description allows for attitude control analysis that includes variation of the pitching hinge stiffness.
  A disadvantage of this method, is that the calculation of the pitching motion due to aerodynamic torques at each time step slightly increases the computational effort, though this increase is not problematic for the proposed aerodynamic analysis in the current work.

4-3 Results

4-3-1 Sweeping Motion Results

For the current work, the sweeping motion is represented by the pure sinusoid function from Equation 4-1. This formulation still allows for taking differences in flapping frequency and flapping amplitude into account, which is sufficient for this study. Additionally, this study focuses more on the general aerodynamic principles of flapping motion and the influence of body motion on aerodynamic performance, rather than the exact aerodynamic response of one specific flapping mechanism. This allows the kinematic description to be used for multiple wing designs and show the different responses to attitude control and additional flows for different wings in a general sense. To verify the validity of this simplification, the aerodynamic force responses a sinusoidal sweeping motion function and a fully measured sweeping motion are compared while using the same expressions for the heaving (none) and pitching (active, sinusoidal) motions. The comparison of sweeping kinematics is shown in Figure 4-3, whereas the comparison of lift force production is shown in Figure 4-4.

Figure 4-3 clearly shows that the purely harmonic description of the sweeping motion differs from the measured sweeping motion. The measured sweeping motion shows both a phase and mean angle offset with respect to the purely harmonic case and the downstroke and upstroke motions are slightly asymmetric as well, which is not the case for the purely harmonic sweeping motion.

Even though Figure 4-4 shows that the force response varies with small changes in sweeping motion, the general shape of the force response stays the same and the average force response shows a 20 percent difference, where the harmonic case has the largest value and therefore

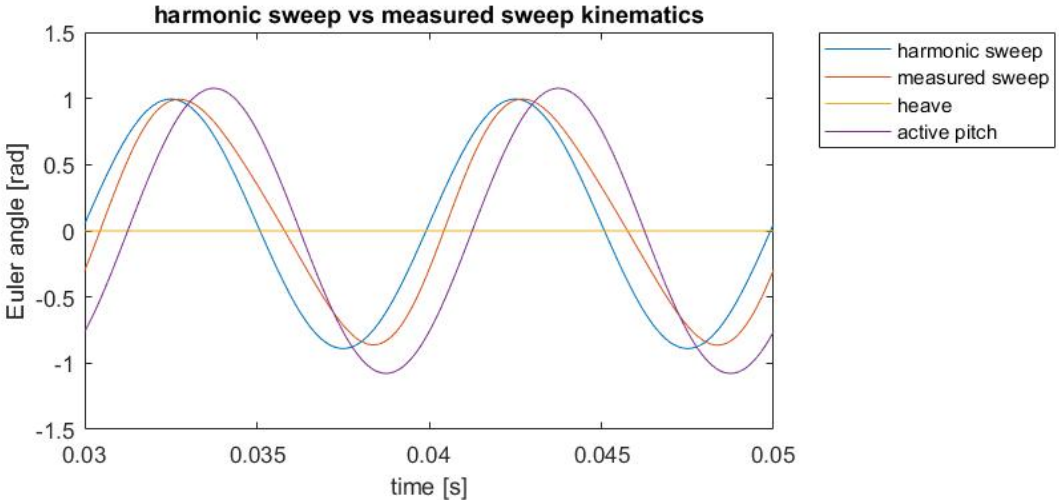

Figure 4-3: A visual representation of the difference between measured sweeping kinematics and purely sinusoidal sweeping kinematics. Note that the kinematics for two consecutive wing strokes are shown, starting with the downstroke. In each following figure, the kinematics and the force responses are shown for two consecutive wing strokes.

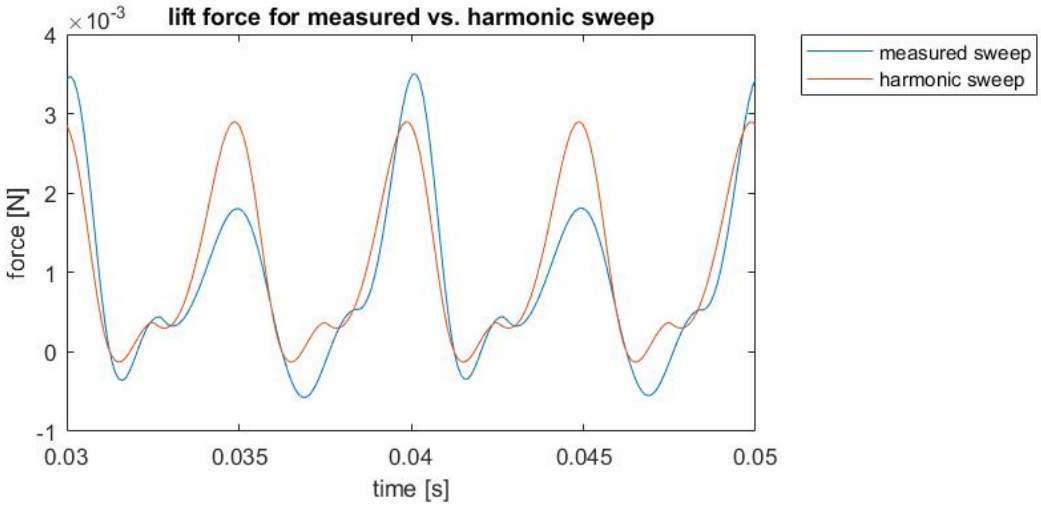

Figure 4-4: Calculated lift forces generated by flapping motion, comparing measured sweeping kinematics with purely sinusoidal sweeping kinematics.

slightly overestimates the average lift force. The harmonic description is decided to be sufficiently accurate, since the global aerodynamic behaviour is captured by the description. Therefore, the comparisons later in this work will be done while using the same harmonic sweeping kinematics that only vary in amplitude.

It should be noted that these sinusoidal sweeping kinematics were also modeled in the Adams® MBD software and were successfully implemented in the current aerodynamic model. This did not lead to any new conclusions for this work, but it shows that a more detailed description of the sweeping kinematics for specific mechanisms could be done in such a modeling environment in future research.

4-3-2 Heaving Motion Results

In the previous section, it was already mentioned that the most Flapping-Wing Air Vehicles (FWAVs) do not have a flapping mechanism that imposes active heaving motion on the wing. Therefore, if present, the heaving motion occurs only passively and no formulation exists for this type of heaving motion at this time. An attempt was made to develop a such passive heaving formulation, using finite element modeling software (Abaqus®) to describe load cases that resemble aerodynamic forces. During this attempt, it became clear that a static load analysis resulted in negligible heaving motions, and a dynamic analysis was too time-consuming to apply within the model. Hence, it was decided that for this research, a passive heaving formulation will not be considered as a valid option to model the heaving motion. Therefore, it will be verified here if the heaving motion can be left out of this analysis altogether, by comparing the measured heaving kinematics with the case that does not include heaving kinematics.

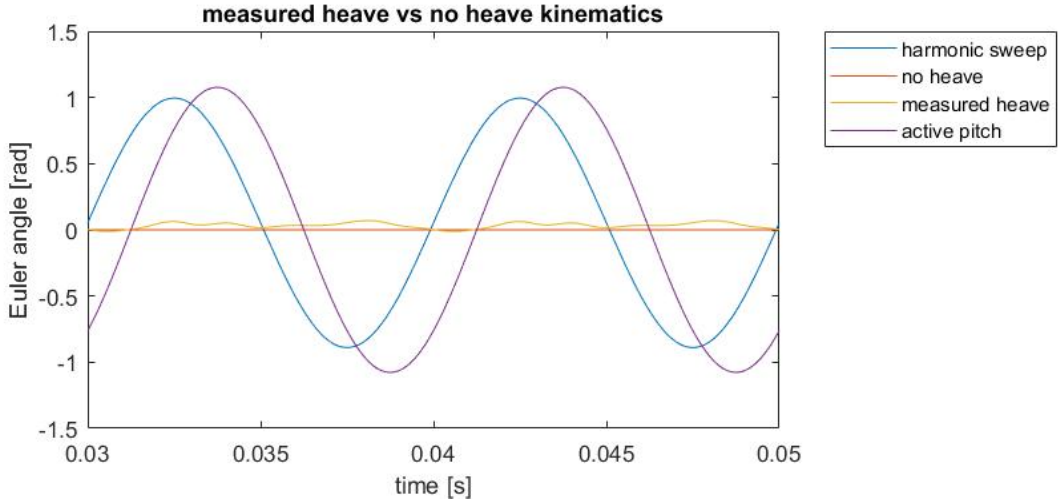

Figure 4-5: A visual representation of the wing kinematics, where the difference between no heave and the measured heave is shown.

As shown in Figure 4-5 and Figure 4-6, a slight change in heaving kinematics gives a slight change in lift force generation of the wing. The global shape of the lift curve is rather similar, but the lift generation at the stroke reversals is rather different. The average lift force shows a difference of 10 percent (where the case without heave is largest). Since a representation of

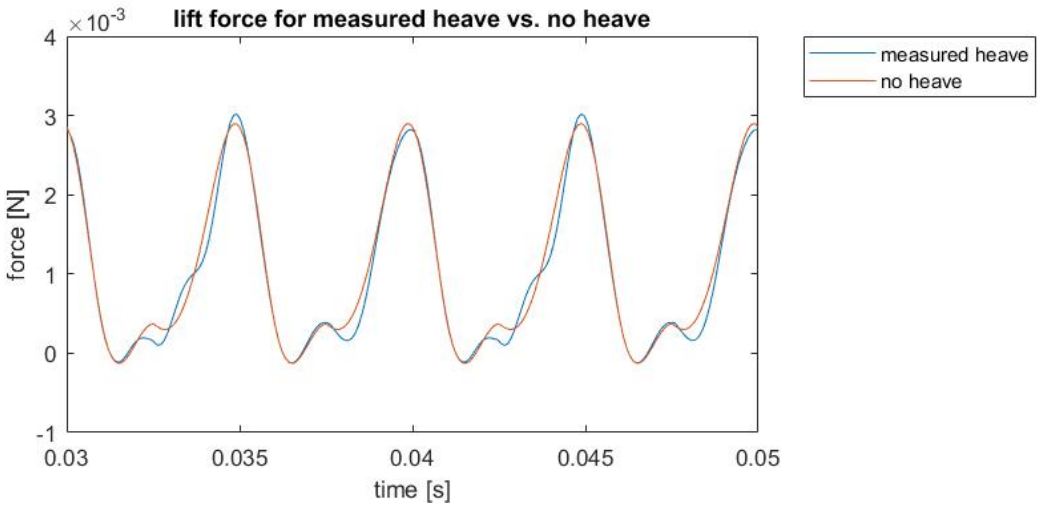

Figure 4-6: Calculated lift force, where the proposed heaving formulation is compared with the calculated lift based on measured heaving kinematics.

the global curve of the lift production is sufficient for this analysis, and since later in this work the same heaving pattern will be used for all scenarios, it was decided to not take heaving motion into account.

4-3-3 Pitching Motion Results

Since the current work researches the force response of the flapping wing under the influence of attitude control and body motions, a general formulation for the passive pitching motion is desired. Since the passive pitching formulation by Wang et al. [47] is in theory widely applicable, it would be desired to use this formulation. However, it must be verified whether this formulation provides a sufficiently accurate prediction of the passive pitching motion.
Therefore, the calculated lift generation corresponding to the fully measured kinematics of all angles of the flapping wing are compared with the calculated lift generation corresponding to measured sweeping and heaving motion while the pitching motion is formulated by the earlier mentioned passive pitching function.
Figure 4-7 shows that the passive pitching function approximates the measured pitching behaviour rather well in a global manner, and Figure 4-8 shows that the lift curve resulting from these approximated kinematics show global agreement too. Comparison of the average lift force over two wing strokes shows a difference of only 1 percent, where the force based on calculated passive pitching motion is the lower of the two. Hence it is concluded that the passive pitching function can be used in the current work.

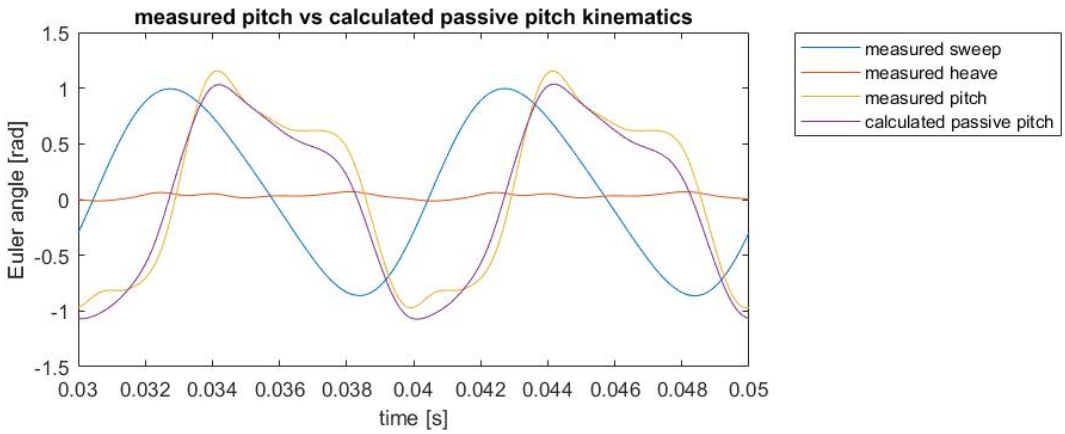

Figure 4-7: Visual representation of the wing kinematics, where the measured passive pitching motion and calculated passive pitching motion are compared.

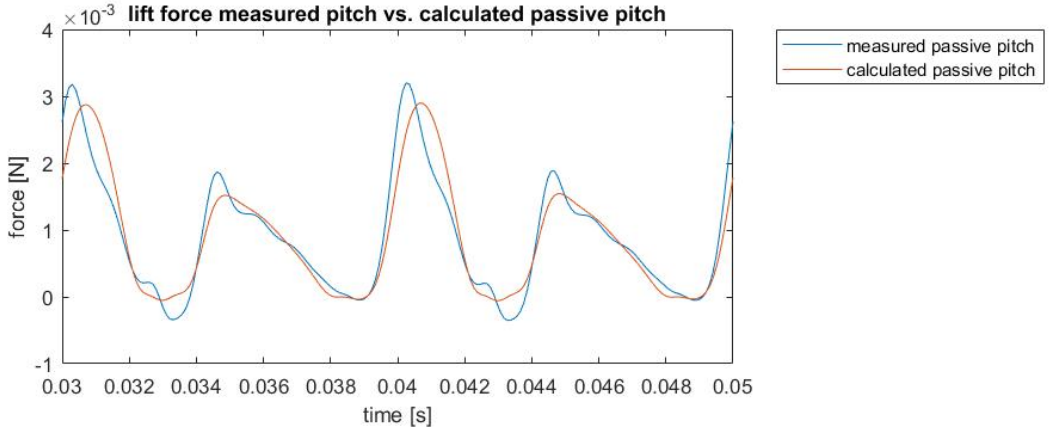

Figure 4-8: calculated lift force with proposed passive pitching formulation compared with the calculated lift based on measured pitching kinematics.

4-4 Chapter Discussion

Firstly, it should be noted that this chapter only compares the formulation options for each kinematic component separately. This was mostly done to provide an insight into the influence of each kinematic component on the aerodynamic lift production, though it should be noted that large changes in sweeping kinematics have an indirect influence on the passive pitching kinematics. Therefore, when the sweeping kinematics would be changed in future research, the passive pitching kinematics should be recalculated due to the indirect influence of the change in sweeping motion. Moreover, the influence of heaving motion on the aerodynamic performance of flapping wings has not been extensively studied, since in most cases the angular displacement in the heaving direction is only a few degrees. It is not known how significant the heaving motion becomes under the influence of flows induced by body motion, which is why the heaving motion is neglected for the rest of this work. It would be worth to research the passive heaving motion due to external flows, and find its influence on aerodynamic performance in future research.

4-5 Chapter Conclusion

This chapter gives an overview of the different time dependent descriptions of the Euler angles of the wing and the influence of these description choices on the aerodynamic performance of the wing. The objective of this chapter is to find a widely applicable formulation for the wing kinematics that does not introduce much extra computational effort, which is also valid during aerodynamic analysis of FWAV that include attitude control and body motions. A global representation of the aerodynamic force response and wide applicability are more important for this work than high numerical modeling accuracy. It was shown that changes in sweeping motion have a large influence on the absolute values of the lift production, but that a pure sinusoid still shows the global aerodynamic behaviour of the flapping wing. Therefore it was decided that the pure sinusoid can be used as description of the sweeping motion for the relative comparisons later in this work. Additionally, it was shown that the heaving motion does not have a large influence on both the absolute values of the lift production and the global aerodynamic response, therefore it was decided to not take heaving motion into account. Lastly, the pitching motion will be described by the passive pitching formulation as done by Wang et al. [47]. This chapter has shown that the passive pitching formulation provides accurate kinematic and aerodynamic results. Furthermore, the passive pitching description is expected to account for the pitching pattern changes induced by changes in sweeping motion, pitching pattern changes induced by adjusting the pitching stiffness and pitching pattern changes induced by external air flows that are induced by body motion. It will be verified in chapter 5 if this is a valid expectation. In short, this chapter has found a widely applicable description for the flapping-wing kinematics that is expected to correctly describe the kinematics and aerodynamics of the flapping wing when attitude control parameters and body motions are introduced.

Chapter 5

Attitude Control Experiments

This section contains the main experiments that are used to answer the research question of this work on attitude control mechanisms for Flapping-Wing Air Vehicles (FWAVs). First the objectives of the experiments will be discussed in section 5-1, after which the experimental methods are described in section 5-2. The results are then shown in section 5-3, after which they are discussed in section 5-4. Lastly, the chapter conclusions will be given in 5-5.

5-1 Experiment Objectives

The objective of the experiments in this chapter is to find the attitude control mechanism that is the most suitable for the Atalanta: either a variable sweeping (or stroke) amplitude or a variable pitching stiffness. Adjustments of the sweeping amplitude will influence the lift force production through direct changes in translational velocity of the wing and indirect changes in rotational velocities and Angle of Attack (AOA) of the wing. Adjustments of the pitching stiffness will directly influence the rotational velocities and AOA of the wing.
To concisely investigate which attitude control parameter is most suitable, the following questions need to be answered:

- Which method results in the largest and most predictable lift force change?
- Which attitude control method has the highest aerodynamic efficiency?
- Does the location of the average effective Center of Pressure (CP) play a role for the attitude control torque? Which method show the largest effective CP location change?
- Which method is most robust to airflow that is induced by motions of the vehicle body?
- Do the answers to questions above hold in a general sense, or do the results depend on wing morphology?

5-2 Experimental Methods

To investigate the influence of the attitude control parameters on the force production of a single flapping wing, the attitude control parameters that were suggested in 1-1-2 have to be varied: the sweeping amplitude and the pitching hinge stiffness. The quasi-steady aerodynamic formulation that was used in this work, directly allows for adjustment of these parameters. Sweeping amplitude ϕ_m can be varied within the kinematic formulation of the sweeping motion, which is a pure sinusoid as described in chapter 4. The pitching stiffness k_η can be adjusted in the parameter settings of the passive pitching function, for which the formulation is given in [47], and can be interpreted as the mechanical resistance that opposes the aerodynamic torques that are generated during the flapping motion.

For the analysis in this chapter, the dronefly wing design as described in Figure 4-2 is used, along with the following base values of the kinematic parameters:

$$\begin{array}{rc} f_{flap}: & 100 \text{ Hz} \\ \phi_m: & 0.9425 \text{ rad} \\ k_\eta: & 2.35 * 10^{-6} \text{ Nm/rad} \end{array}$$

The sweeping amplitude will be adjusted to 75%, 87,5%, 100%, 112,5% and 125% of the original value. For the pitching stiffness, this will be done for 50%, 75%, 100%, 125% and 150% of the original value. The influence of these attitude control parameters on the kinematics, force production and effective CP location on the wing will be analyzed in the following way. The aerodynamic model from chapter 2 and the kinematic framework proposed in chapter 3 are combined to compute the aerodynamic forces produced by the flapping wing, as done in chapter 4. The addition that is done in the current chapter, is that the kinematic components due to body motion can be included in the kinematic definition of point p on the wing. This allows for aerodynamic analysis that takes both attitude control parameters and the influence of vehicle body motion into account.
A qualitative analysis will be done of the changes in wing kinematics and the different aerodynamic force components. A quantitative analysis of the average lift production, average lift production efficiency and average effective CP location is done afterwards. The efficiency of the wing stroke in terms of lift force is defined as the magnitude of the average lift force with respect to the magnitude of the average total aerodynamic force. For the computation of the average CP, the CP terms associated with each aerodynamic term are calculated as described in chapter 2, force weighted and added for each time step. Then the average over time is taken for each set of attitude control parameters and body motion conditions.

It should be noted that quantitative analysis steps are done while using the average lift forces and average effective CP locations, instead of the instantaneous values, for two reasons. Firstly, finding the instantaneous values of the lift force of flapping wings is difficult. Both physical measurements and aerodynamic models (both Computational Fluid Dynamics (CFD) and analytical models), do not provide accurate results for the instantaneous lift force. The measurements of average lift forces can be predicted more accurately and consistently, making the average values more suitable for quantitative analysis. Secondly, maneuvers of FWAVs happen over multiple wing beats [24]. Therefore, the average lift force per wing stroke gives sufficient information on the attitude control forces.

To investigate the robustness of the attitude control methods with respect to external airflow induced by body motion, the aforementioned characteristics will be analyzed for two cases of body motion. Firstly, a forward body motion of 3 m/s will be applied to the vehicle. Earlier research by Willmott & Ellington [49], describes measurements of the kinematics of hawkmoths (Manduca Sexta) that show body velocities up to 5 m/s. Since the dronefly wing is smaller than the hawkmoth wing, the forward velocity of the dronefly was estimated at 3 m/s, which is slightly lower but in the same order of magnitude as forward velocity of the hawkmoth. Second, a theoretical description of vertical oscillation during hovering will be analyzed, which is modeled as a sinusoidal vertical motion with a frequency that is equal to twice the flapping frequency, since lift is generated twice every wing stroke. Both these flow cases will be compared with the previously mentioned numerical experiments that do not include flow.

To investigate the sensitivity of the aerodynamic response to small changes in wing morphology, the aforementioned aerodynamic analysis will be done for another wing with a different shape and a size similar to that of the dronefly wing.

It should be noted that all the experiments described above are done while using the quasi-steady formulation from chapter 2, that originally does not include external flows and attitude control. However, the added body motions and attitude control variables are applied in such a way that the basic assumptions for the validity of this model are not violated. Hence, it is assumed that the internal comparison of the attitude control variables and added body motions is valid within the current work, to show the general aerodynamic behaviour due to the variation of attitude control parameters and body motions.

5-3 Results

Firstly, the case for basic attitude control without additional flows will be investigated. After this, the impact of external flows will be analyzed by simulating a state of forward motion and vertical oscillations during hovering. Lastly, the influence of wing morphology will be investigated.

5-3-1 Basic Attitude Control

Kinematics

Firstly, the results without any flow induced by body motion will be shown. As expected, the kinematics of the wing are changed when sweeping amplitude ϕ_m and pitching stiffness k_η are varied. Changing ϕ_m will simply change the amplitude of the sinusoidal sweeping motion, which is shown in Figure 5-1.

Since the passive pitching motion is coupled to the sweeping motion through the aerodynamic torques that are generated by the wing motion, the pattern of the passive pitching motion changes when ϕ_m is changed. This effect is shown in Figure 5-2, where it is clearly shown that the amplitude of the pitching motion slightly increases with each increase in ϕ_m. The figure shows that the passive pitching motion is periodic and symmetric around zero, but it is not a perfect sinusoid like the sweeping motion. This is due to the nonlinear aerodynamic

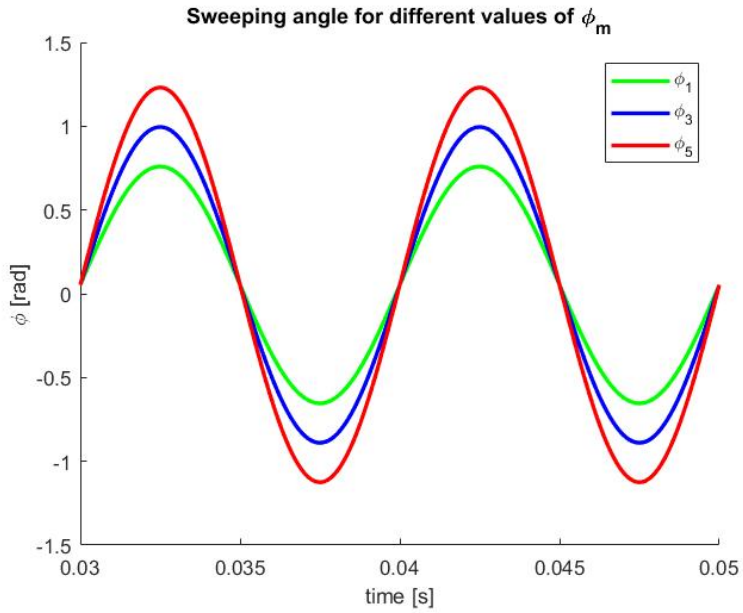

Figure 5-1: Sweeping angle ϕ over time, associated with different values for the sweeping amplitude ϕ_m. Note that two full wing strokes are shown in the figure and that the motion starts with the downstroke, which is the same for all following figures. Legend entries ϕ_1, ϕ_3 and ϕ_5 refer to the lowest, middle and highest values of ϕ_m, respectively. These sweeping kinematics hold for all test cases that are discussed in this chapter.

effects that induce aerodynamic torques around the pitching axis. Furthermore, the phase stays approximately the same although the pitching pattern just after the stoke reversal is slightly different for each value of ϕ_m.

Obviously, since k_η directly influences the stiffness of the pitching hinge with respect to aerodynamic torques, k_η changes the passive pitching motion of the wing as well. This effect is shown in Figure 5-3, which shows an increase in pitching amplitude for each decreasing step in pitching stiffness. This increase in pitching amplitude is higher than the indirect amplitude increase due to the variation of ϕ_m. Moreover, the figure shows a phase delay between the pitching patterns that are associated with different values of k_η and a difference in pattern shape just after stroke reversal. Just like in Figure 5-2, Figure 5-3 shows a periodic pitching pattern that is symmetric around the zero angle, though again it is not a perfect sinusoid like the sweeping pattern.

To provide insight in the range of pitching patterns that can occur and to compare the influence of ϕ_m and k_η on the pitching patterns qualitatively, the pitching patterns associated with 9 different attitude control parameter settings are plotted in Figure 5-4. The lines describing the pitching patterns show a lot of overlap, though significant differences in pitching amplitude and motion phase can be discovered. In general, the change in amplitude and phase is larger for variations of k_η than for variations of ϕ_m. This indicates that the pitching amplitude has a higher sensitivity to changes in k_η than to changes in ϕ_m, especially since with each step k_η only increases with 25% whereas ϕ_m increases 50% with each step. Furthermore, it is shown that the indirect influence of ϕ_m on the pitching angle is larger for lower values of k_η than for higher values of k_η. This makes sense, since the pitching pattern of the flapping

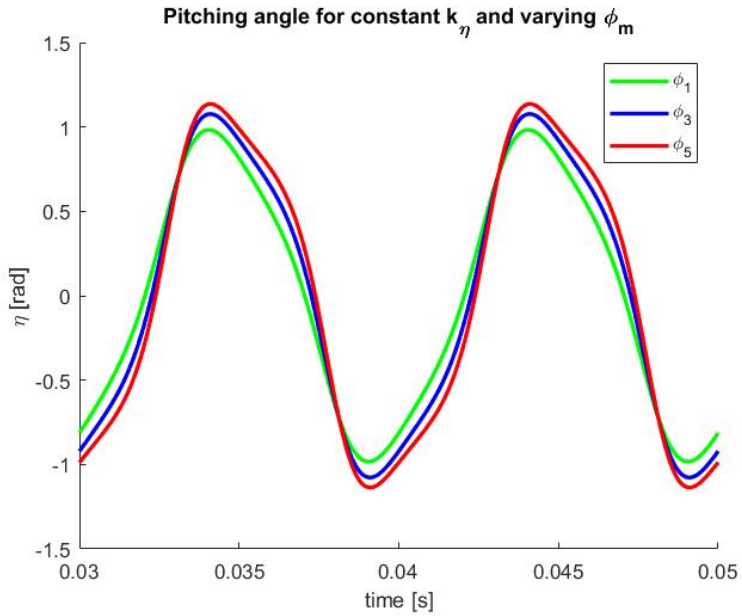

Figure 5-2: Pitching angle η over time, associated with different values for the sweeping amplitude ϕ_m. Legend entries ϕ_1, ϕ_3 and ϕ_5 refer to the lowest, middle and highest values of ϕ_m, respectively. This figure corresponds to the case that does not include body motions.

.

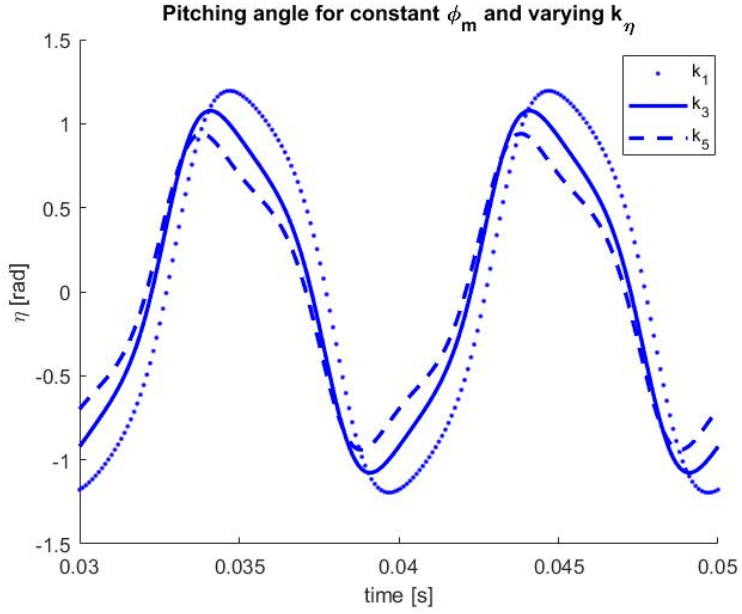

Figure 5-3: Pitching angle η over time, associated with different values for the pitching stiffness k_η. Legend entries k_1, k_3 and k_5 refer to the lowest, middle and highest value of k_η, respectively. This figure corresponds to the flow case that does not include body motions.

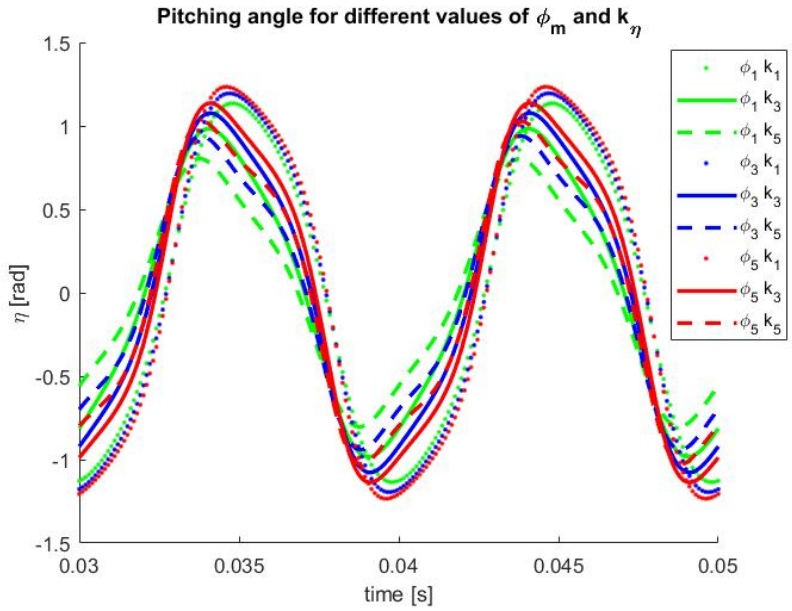

Figure 5-4: Pitching angle η over time, associated with different values for ϕ_m and k_η. Legend entries correspond to the same values as before, though now they are combined. For example, $\phi_1\, k_1$ corresponds to the lowest values of both ϕ_m and k_η. Different colors correspond to different values of ϕ_m and different line fonts correspond to different values of k_η. This figure corresponds to the flow case that does not include body motions.

wing becomes less susceptible to changes in aerodynamic force when the pitching stiffness increases. Lastly, the figure clearly shows that for all attitude control parameter settings the pitching pattern is periodic and symmetric around the zero angle, though none of them resemble a perfect sinusoid.

Forces

As mentioned in chapter 2, the aerodynamic lift force in the current formulation contains four force terms. The response of these aerodynamic terms over time is shown in Figure 5-5 together with the total lift force, which is simply the four separate terms added together. The attitude control parameters corresponding to Figure 5-5 are the ones associated with the optimized values from literature ([47], [48]), so it shows the aerodynamic response of the dronefly wing as it normally behaves. The figure clearly shows that all aerodynamic components behave periodically, with two peaks of lift production in one wing stroke since both the upstroke and downstroke generate lift. Moreover, it is shown that the lift peaks generated due to the translational force are approximately twice as high as the other terms. Therefore, it makes sense that the the total lift curve roughly follows the shape of the translational force curve. Furthermore, the phase of the coupling term and the added-mass term matches in such a way that the total aerodynamic force never drops below zero.

First, ϕ_m is varied to its highest value while k_η remains constant, of which the effects are shown in Figure 5-6. The shape of the total force curve is not altered by much, though the absolute value of all force peaks (both positive and negative) have increased, which leads to

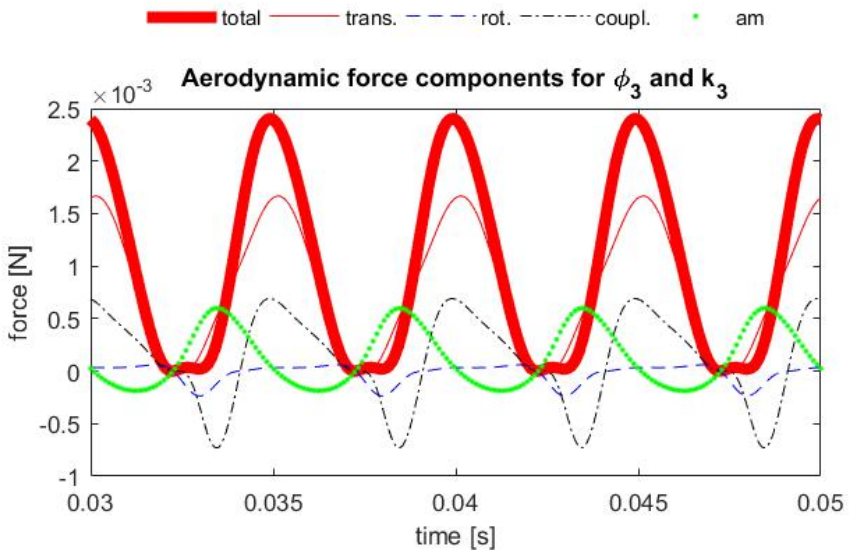

Figure 5-5: Breakdown of the different aerodynamic force components over time, for the middle values of ϕ_m and k_η.This figure corresponds to the flow case that does not include body motions.

the peak of the total aerodynamic force increasing by 40%. This shows that the increase in wing velocity combined with the slight change in pitching pattern has a large positive influence on the lift production. Moreover, a slight phase difference is visible between the added-mass, rotational and coupling force, which leads to the total aerodynamic force going slightly below zero for a short period of time during stroke reversal.

When k_η is varied, the force responses change in a rather different way. Figure 5-7 shows the aerodynamic response for the middle value of ϕ_m and the lowest value of k_η. Compared to Figure 5-5, the current figure shows a decrease in the absolute value of the peaks of all force components except for the negative peaks of the coupling force. Still, the shape of the total force curve is dominated by the shape of the translational force curve, and the total force peaks are reduced in height by 20%. This shows that this combination of ϕ_m and k_η leads to a less optimal AOA value than the original combination of attitude control values. It should be noted that the reduction of the magnitude of the translational force causes the other force terms to be more significant for the shape of the total force curve. Lastly, the phase difference between the force components now causes the total force to clearly drop below zero.

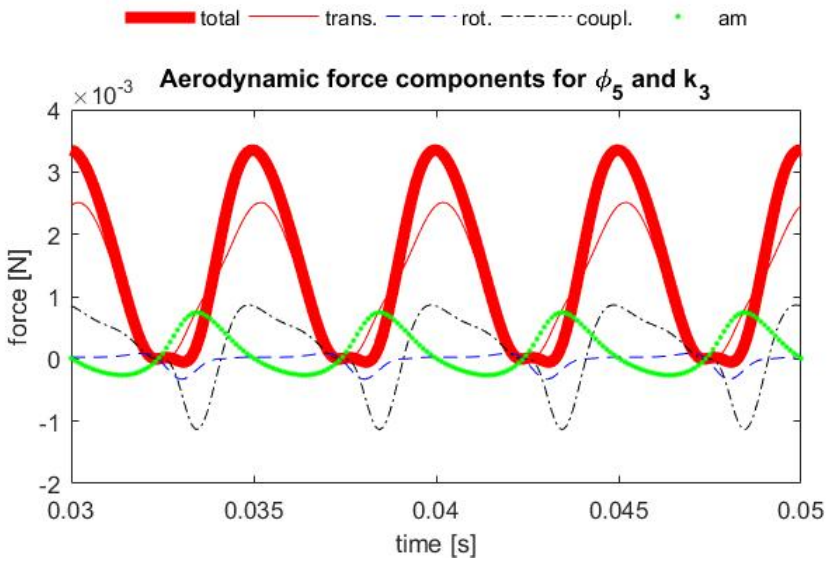

Figure 5-6: Breakdown of the different aerodynamic force components over time, for the highest value of ϕ_m and the middle value of k_η.This figure corresponds to the flow case that does not include body motions.

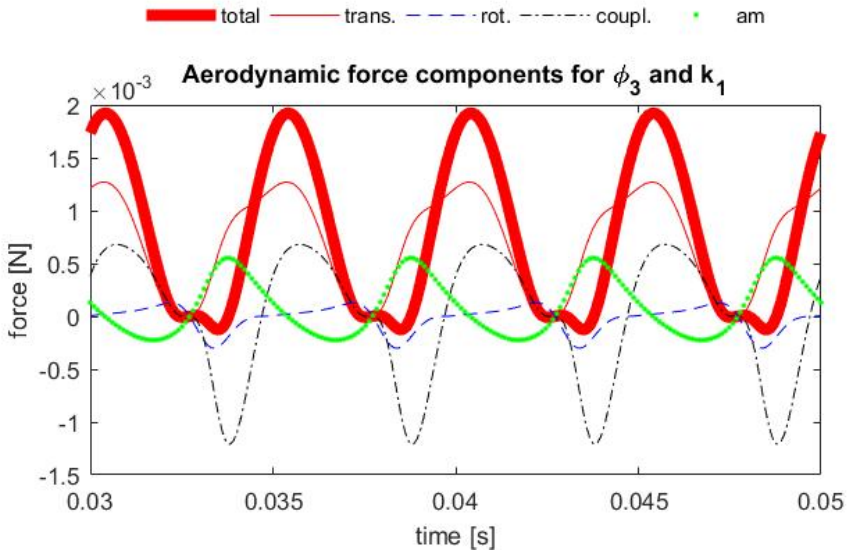

Figure 5-7: Breakdown of the different aerodynamic force components over time, for the middle value of ϕ_m and the lowest value of k_η. This figure corresponds to the flow case that does not include body motions.

To get a better insight in the sensitivity of the lift production to the attitude control parameters, the average lift force was calculated for each combination of ϕ_m and k_η. The results of this calculation are shown in Figure 5-8. This figure clearly shows that for low ϕ_m and low k_η (in the top left corner), the lift increases gradually and with the same order of magnitude for both parameters with each increase step. The increase of lift is consistently visible for each increase in k_η, though for higher stiffness (the right half of the figure) the gradual increase is not visible. For the highest sweeping angle, the highest lift production is reached with the highest pitching stiffness, which is not the case for the lowest sweeping angle. This suggests that there is an optimum in pitching stiffness for each sweeping amplitude, of which the optimal value increases with increasing sweeping amplitude, as shown by the optimal lift value in the bottom right of the heat map. The highest lift value shows a 50% increase in average lift, whereas the lowest lift value shows a 50% decrease in average lift value with respect to the original average lift value. Lastly, Figure 5-8 shows that ϕ_m has a larger and more consistent effect on the lift production than k_η, which suggests that the variation of wing velocity has a larger influence on lift production than an optimal AOA for the case of zero body motion.

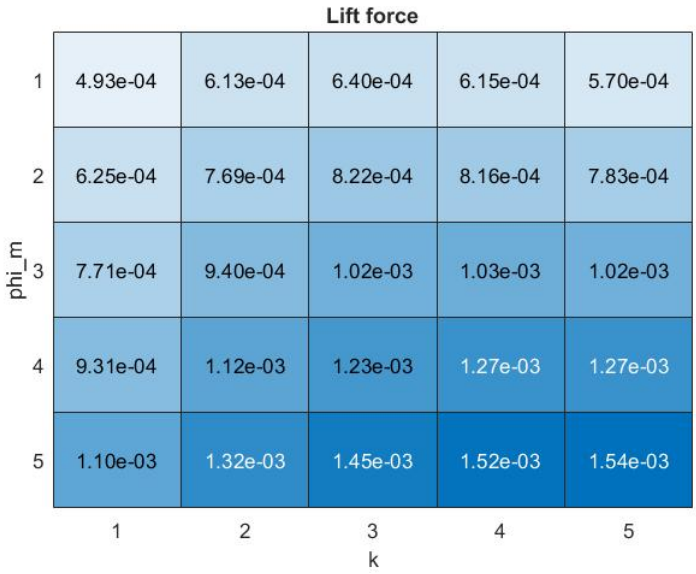

Figure 5-8: A quantitative heat map of the average lift force, associated with each of the 25 combinations of attitude control parameters. This figure corresponds to the flow case that does not include body motions.

The efficiency of the wing stroke, defined as the percentage of the total aerodynamic force that is directed upward as lift force, is shown in Figure 5-9. First of all, the differences in efficiency are of the order of a few percent, which suggests that sensitivity of the efficiency with respect to the attitude control parameters is low relative to the sensitivity of lift production with respect to the attitude control parameters. Furthermore, the figure shows that the optimum of the efficiency lies around the diagonal from top left to bottom right. Remarkably, the optimal efficiency value does not lie at the center of the heat map which corresponds to the design parameters for this wing that were found in literature.

Figure 5-9: A quantitative heat map of the average efficiency of the wing stroke, associated with each of the 25 combinations of attitude control parameters. This figure corresponds to the flow case that does not include body motions.

Effective CP

Figure 5-10 shows the effective average CPs of for the different attitude control variables. The main interest is in the spanwise location of the effective average CP, since this coordinate would potentially have the largest influence on the roll torque of the vehicle. As the figure shows, the position of the effective CPs only changes with a few percent of the span in the spanwise direction. This change in position is negligible with respect to the order of magnitude in lift force change, which was 50% at its maximum, since both the spanwise CP position and the lift force are linearly related to the roll torque. Therefore it is assumed that for the case of zero body motion, the influence of the location of the effective CP does not have a significant influence on the attitude control torque around the roll axis of the vehicle.

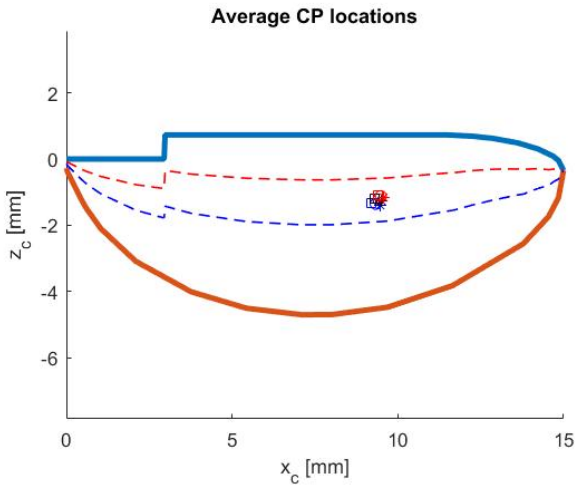

Figure 5-10: Schematic representation of the flapping wing, with the CP locations of the 9 most characteristic combinations of attitude control parameters that were used for Figure 5-4 as well. This figure corresponds to the flow case that does not include body motions. Red and blue dashed lines correspond to the quarter chord and half chord respectively.

5-3-2 Body Motion Effects

This section researches the robustness of both attitude control parameters with respect to external flows that are induced by body motions. As mentioned in section 3-1-1, the body motions are imposed on the system, meaning that the body motions have an influence on the aerodynamic performance, where the aerodynamic response does not influence the body motions. Firstly, a state of forward flight is discussed. Lastly, the motion case that mimics vertical oscillations during hover is analyzed.

Forward Flight

As mentioned in section 5-2, the forward flight velocity of a dronefly was estimated at 3 m/s, and during forward flight the vehicle is estimated to be at a 30° incline. In other words, the pitching angle Θ of the vehicle, the angle between the z_b and Z_G axis, has a value of 30° while the velocity of the vehicle in the Y_G direction is 3 m/s (see Figure 3-3 for a recap on the reference frames). This section analyzes the aerodynamic forces on the wing during forward motion, and compares the robustness of the attitude control mechanisms with the added velocity terms. Note that the forward velocity of 3m/s is around the order of magnitude of the wingtip velocity, hence it is expected that this additional motion has a significant influence on the aerodynamic response. The passive pitching motion is the only kinematic term that can be influenced by the added airflow, since the sweeping motion is prescribed. This influence can simply be shown by plotting the full wing kinematics for the zero flow case and the current flow case, as done in Figure 5-11.

As Figure 5-11 clearly shows, the pitching angle η (defined in the hinge-fixed frame i) has a negative offset of around 0.5 rad and due to the flow induced by body motion, the transition from downstroke to upstroke has a different shape compared to the transition from upstroke to downstroke. The amplitude of the pitching motion of the forward flow case is comparable

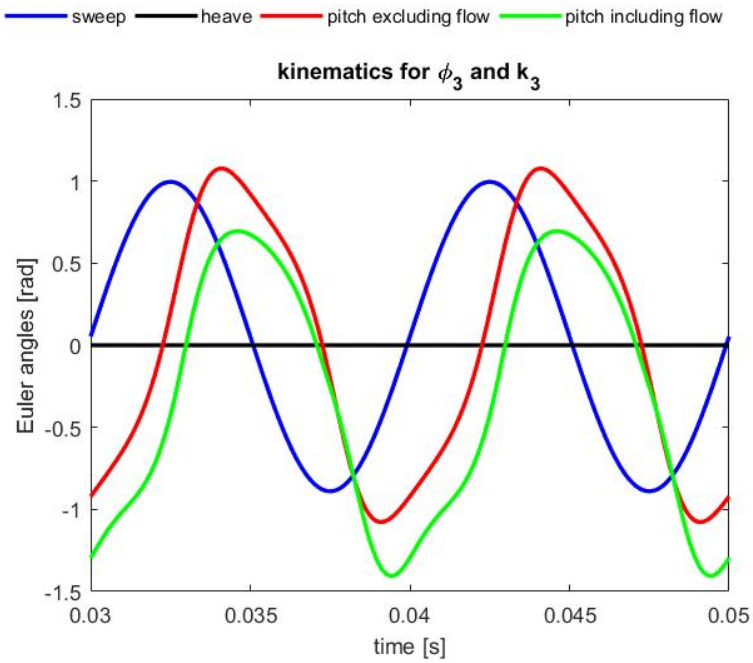

Figure 5-11: Full kinematics of the flapping wing during forward motion under an angle of 30 degrees, compared with the kinematics of the case that does not include body motion, for the two middle values of ϕ_m and k_η.

to that of the still case.
The attitude control parameters ϕ_m and k_η are varied in the same manner as before in Figure 5-4, though influence of the variation of the attitude control parameters on the passive pitching motion is different. This is clarified by Figure 5-12, which shows the pitching motion for the same combinations of attitude control parameters as Figure 5-4. Figure 5-12 shows some clear differences with Figure 5-4. The pitching pattern is still periodic, but the symmetry along the zero angle line is no longer present due to the asymmetric wing velocity that is induced by airflow that is induced by body motion. Furthermore, the increase in pitching amplitude during the downstroke to upstroke reversal seems to be comparable for both parameter variations, which was not the case earlier. On the contrary, during the upstroke to downstroke reversal, there is a clear distinction between the influence of ϕ_m and k_η since the decrease in k_η shows a very clear increase in pitching amplitude and phase whereas the amplitude changes for increases in ϕ_m seem to be marginal.

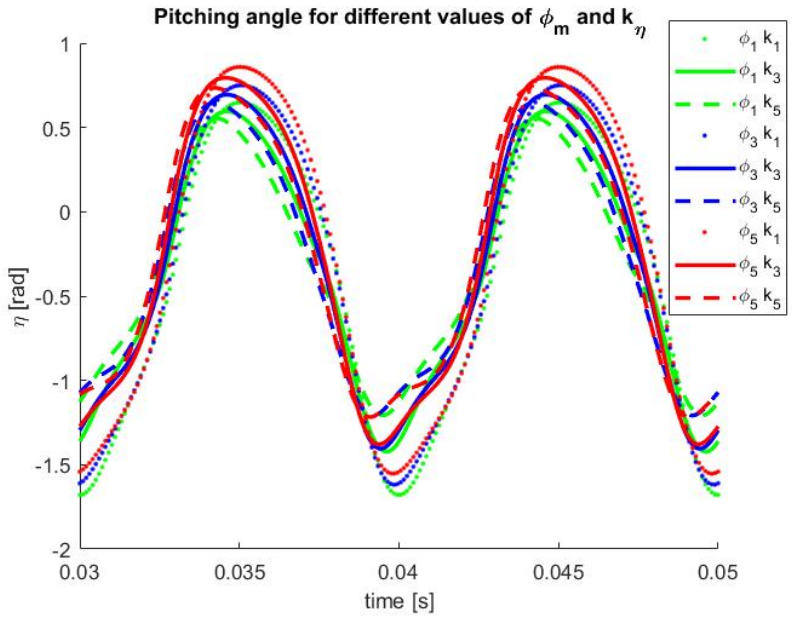

Figure 5-12: Pitching angle η associated with different values for ϕ_m and k_η. Legend entries and line colors correspond to the same attitude control parameter values as in Figure 5-4. This figure corresponds to the forward body motion case.

The change in kinematics for this flow case has consequences for the aerodynamic forces. Firstly, the aerodynamic forces with the standard attitude control settings are shown in Figure 5-13. This figure shows many similarities to Figure 5-5 except for the fact that in the current figure, the translational force peaks are higher and the translational force curve shows a small higher order oscillation during the downstroke. Also, the total force peaks are approximately 20% higher in Figure 5-13 compared to Figure 5-5. When ϕ_m is increased, the translational force peaks increase just like in the previous case without flow. However, when k_η is decreased, the influence of the flow case on the attitude control mechanism becomes more clear.

Figure 5-14 shows a rather chaotic graph where the sweeping pattern cannot be clearly derived from the force graph any more. This is due to the pitching stiffness being too low to resist the incoming flow, which makes that the influence of the body-motion induced flow on the pitching pattern becomes comparable to that of the sweeping motion. This causes the AOA to become larger than its optimal value during the downstroke, which causes irregularities in the lift peak during the downstroke.

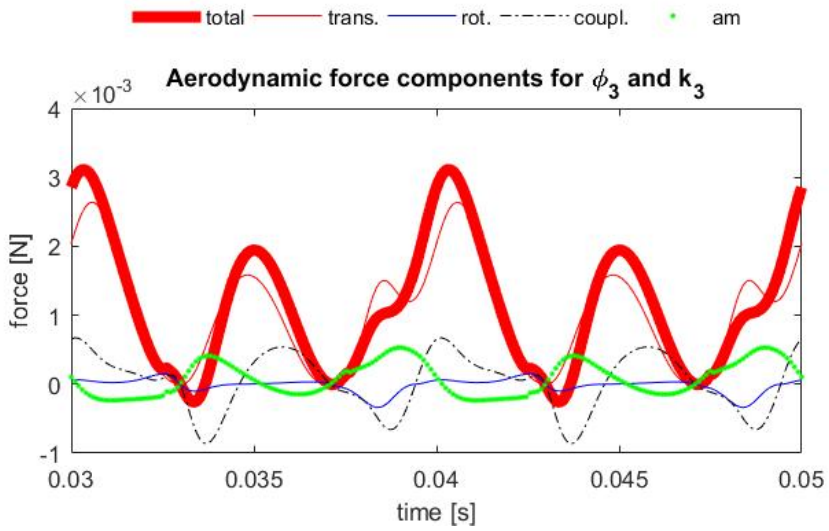

Figure 5-13: Breakdown of the different aerodynamic force components over time, for the middle values of ϕ_m and k_η. This figure corresponds to the forward body motion case.

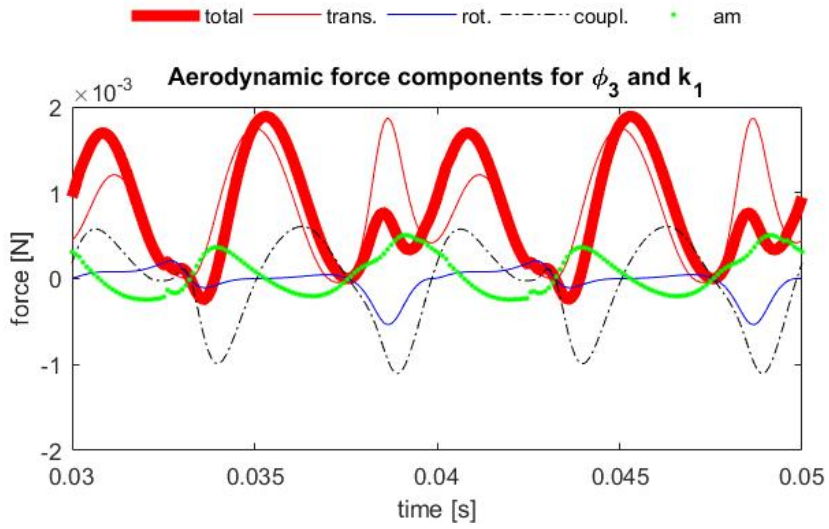

Figure 5-14: Breakdown of the different aerodynamic force components over time, for the middle value of ϕ_m and lowest value of k_η. This figure corresponds to the forward body motion case.

Due to the partially frontal incoming flow, the velocity of the wing with respect to the surrounding air is higher during the downstroke and lower during the upstroke, compared to the case without additional flow. Overall, the lift production of this flow case is higher compared to the case without flow, for most combinations of attitude control parameters that were analyzed. This is shown in the heat map in Figure 5-15. The fact that the increase in lift production is inconsistent for the different attitude control parameters, indicates that the attitude control parameters are not linearly related to the lift production.
The wing's sensitivity to the attitude control parameters changes as well. With the current flow case, an increase in pitch stiffness leads to an increase of lift production for all sweeping amplitudes, which was not the case for the case without flow (see Figure 5-8). This suggests that during forward flight, the AOA has a more significant influence on the lift production than during standstill. Nevertheless, the variation of sweeping angle shows a more consistent and predictable change in lift than variation of the pitching angle, which would suggest that the sweeping amplitude is a more robust parameter to control lift variation in the case of forward flow as well. The attitude control parameter settings with maximal lift production show a 59% increase compared to the original parameter settings, whereas the parameter settings with the lowest lift production show a 56% decrease in lift production compared to the original parameter settings.
Though an increase in lift occurs when the forward body motion is introduced, the efficiency of the wing stroke decreases rather drastically, as shown in Figure 5-16. The difference between the most and least efficient wing stroke in this design domain is approximately 27%. Additionally, the difference in efficiency between the different attitude control parameter cases is much larger in Figure 5-16 compared to Figure 5-9. The drop in efficiency once flow is introduced, can be explained by the fact that the wing is optimized and analyzed for hovering without any external flows. Again, the most efficient combinations of parameters occur along the main diagonal of the heat map.

Due to the introduced flow, the average effective CP shows a shift in position for all attitude control parameters. The expectation is that this shift would occur symmetrically for all wings of the vehicle, therefore it would not introduce any roll torques. For the forward flow case, the magnitude of effective CP differences between the attitude control parameters is larger than for the still case, but still in the order of a few (maximum 8) percent. This could slightly disturb the generation of a roll torque, although again it is not significant compared to the differences in lift production. For completeness, a visual representation is shown in appendix C, in Figure C-1.

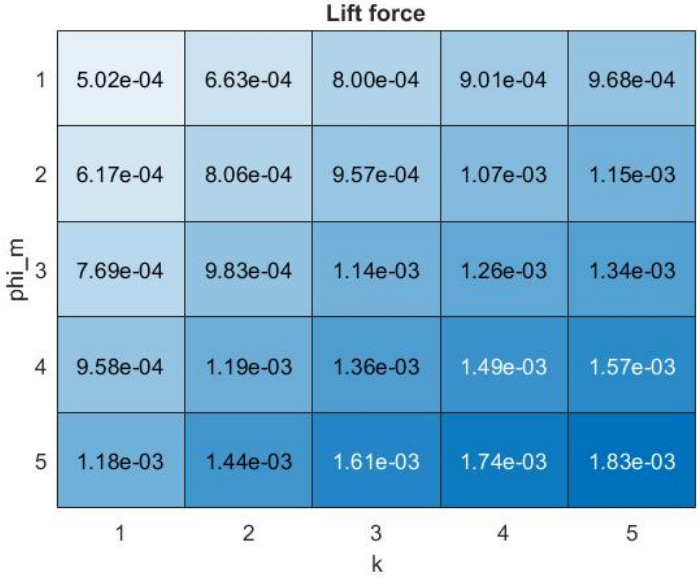

Figure 5-15: A quantitative heat map of the average lift produced by the flapping wing, associated with each of the 25 combinations of attitude control parameters. This figure corresponds to the forward body motion case.

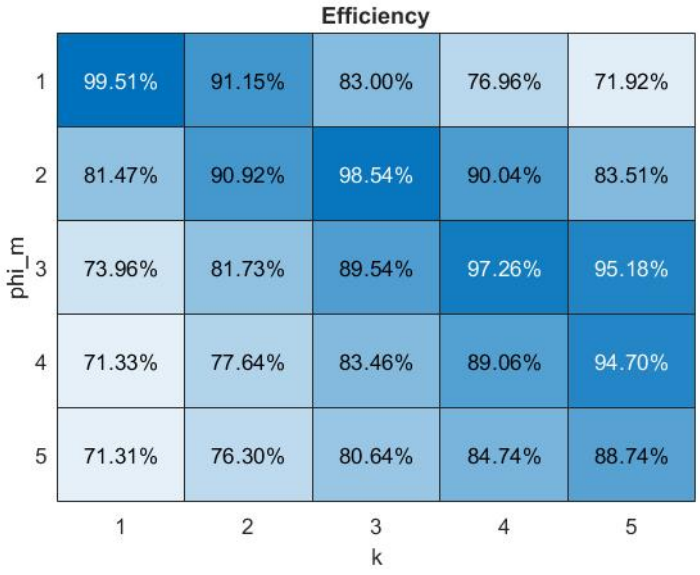

Figure 5-16: A quantitative heat map of the average efficiency of the wing stroke, associated with each of the 25 combinations of attitude control parameters. This figure corresponds to the forward body motion case.

Oscillations During Hovering

Due to the inherently sinusoidal shape of the lift production, the motion of the vehicle during hover will show a sinusoidal vertical motion as well. This motion will likely be damped due to the aerodynamic damping of the wings, but as a first-order approximation the vertical motion during hovering is modeled as a simple sinusoid with twice the flapping frequency and an amplitude of 5mm, since lift is produced with each half stroke and thus an upward motion is induced twice per wing stroke.

The hovering motion has been defined in such a way that the vehicle is at its highest position at the moment of stroke reversal, and descends from there as there is a brief moment of zero (or even negative) lift production during the stroke reversal phase. The airflow that is introduced by this motion results in the wing kinematics as shown in Figure 5-17. This figure clearly shows that the flow induced by the vertical motion both causes a pitching amplitude difference and a phase difference with respect to the case that does not include flow. To further clarify the kinematic behaviour during hovering-induced vertical oscillations for varying attitude control parameters, the full spectrum of possible pitching kinematics due to attitude control parameter variation is shown in Figure 5-18. This figure clearly shows that variations in pitching stiffness have a larger influence on the pitching behaviour than variations in sweeping amplitude.

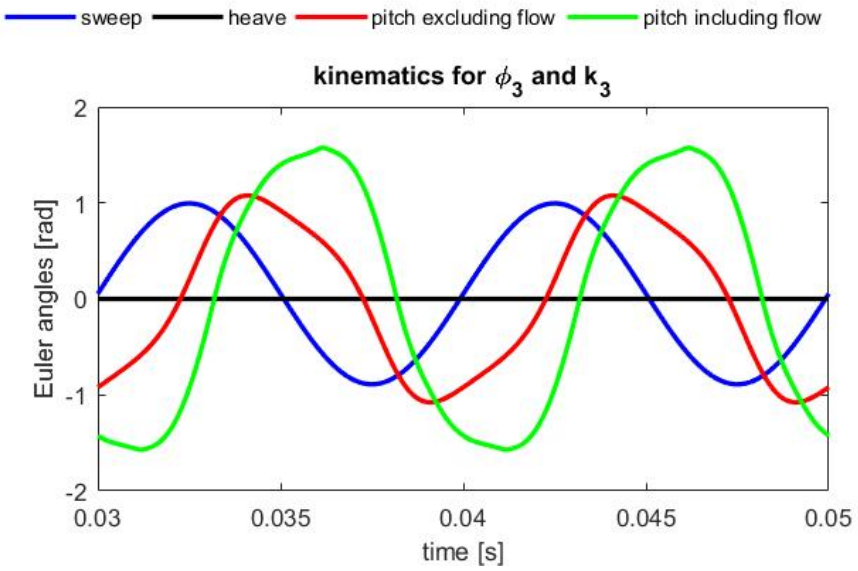

Figure 5-17: Full kinematics of the wing, that compares the pitching motion in the case of vertical oscillations during hovering with the case that does not include body motion, for the middle values of ϕ_m and k_η.

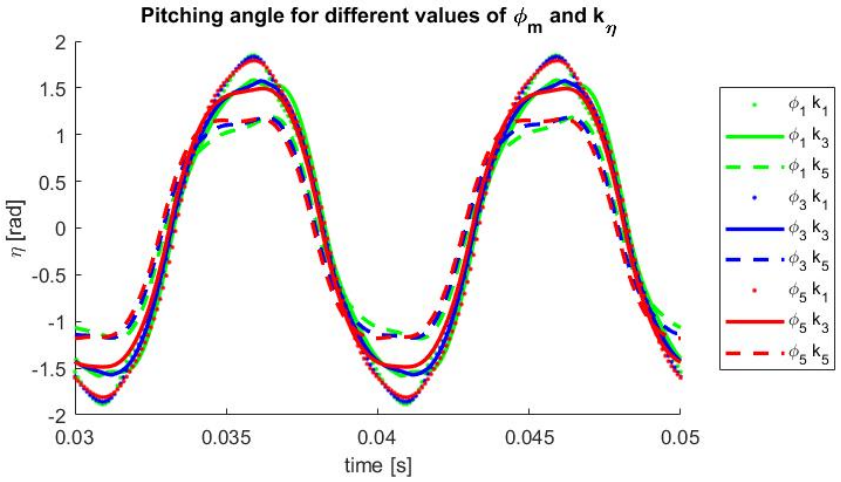

Figure 5-18: Pitching angle η associated with different values for ϕ_m and k_η. Legend entries and line colors correspond to the same attitude control parameter values as in Figure 5-4. This figure corresponds to case that simulates vertical oscillation during hover.

Since this flow case shows such a different pattern for the pitching angle, the lift force response is expected to be rather different as well. This suspicion is confirmed by Figures 5-19 and 5-20. These figures illustrate that this flow case introduces a larger lift force amplitude for all forces and a more force curve with more higher order harmonic behaviour, compared to the stationary case that was shown in Figure 5-5. Especially Figure 5-20 shows that when the amplitude of the translational terms decrease, the total lift force is influenced by the other terms to a larger extent. This is caused by the low pitching stiffness, which makes the wing more susceptible to external flows, which reduces the influence of the sweeping motion on the lift force production and reduces the production of aerodynamic force in this case. This is confirmed by Figure 5-19, which shows that an increase in pitching stiffness causes the peaks of the translational force to become twice as high compared to Figure 5-20.

The overall influence of the pitching stiffness becomes more clear when the heat map for lift production is observed in Figure 5-21. This figure shows that an increase in pitching stiffness results in an increase in lift force, whereas an increase in sweeping amplitude does not show this behaviour throughout the complete heat map. This again shows the importance of the wing velocity combined with a suitable pitching stiffness to provide for an optimal AOA, so that the translational force is produced optimally. The influence of attitude control parameters on the lift production is significant for this case of body motion as well: the best performing combination of attitude control parameters shows an increase of 75% in lift production, whereas the worst performing combination of attitude control parameters shows a 21% decrease in lift production with respect to the original attitude control parameters. It should be noted that for this flow case, the efficiency of the wing stroke does not drop as much as for the forward flow case, as shown in figure 5-22. This is not surprising, since this flow case resembles the stationary case that was originally used to model hovering behaviour. The efficiency optimum is less clearly defined than in the previous flow cases.

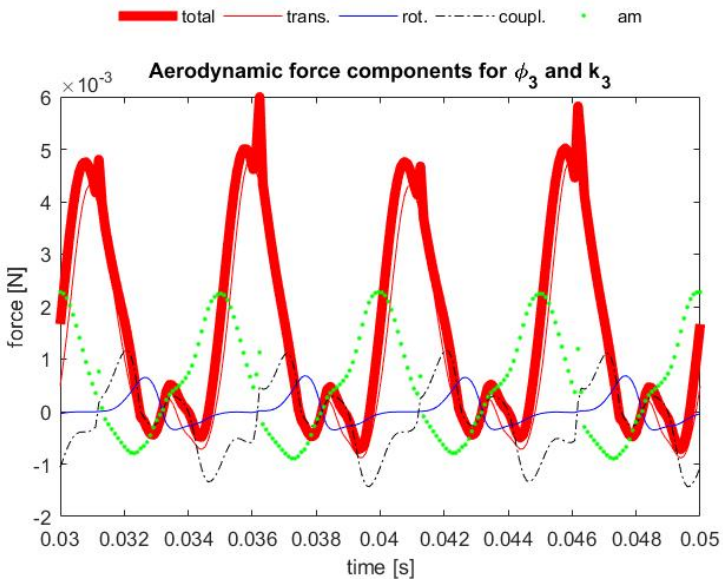

Figure 5-19: Breakdown of the different aerodynamic force components over time, for the middle values of ϕ_m and η_k. This figure corresponds to the flow case that simulates the vertical oscillation during hover.

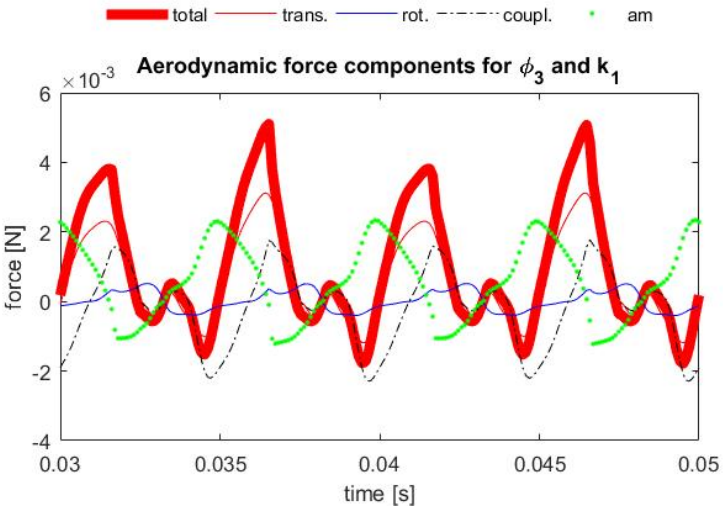

Figure 5-20: Breakdown of the different aerodynamic force components over time, for the middle value of ϕ_m and lowest value of η_k. This figure corresponds to the flow case that simulates the vertical oscillation during hover.

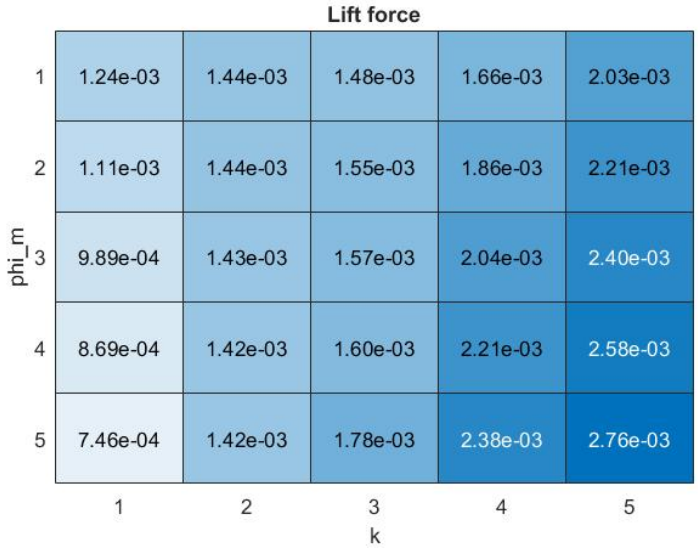

Figure 5-21: A quantitative heat map of the average lift produced by the flapping wing, associated with each of the 25 combinations of attitude control parameters. This figure corresponds to the flow case that simulates the vertical oscillation during hover.

Figure 5-22: A quantitative heat map of the average efficiency of the wing stroke, associated with each of the 25 combinations of attitude control parameters. This figure corresponds to the flow case that simulates the vertical oscillation during hover.

Similar to the forward flight case, the average effective CP locations are slightly shifted due to flow that is induced by vertical oscillations, though approximately the same shift holds for all attitude control values. Since the effective CP location only changes with a few percent of the wing span, it is decided that the changes in effective CP location are not significant with respect to the changes in lift production. For completeness, a visual representation is given in appendix C in Figure C-2.

5-3-3 Wing Morphology Influence

The current work aims to find out if the effect of the attitude control parameters that was found before holds for multiple wing morphologies. Earlier, it was suggested that for the dronefly wing, the average lift production and efficiency depends on the optimization of the wing. Therefore, the influence of the attitude control parameters is investigated for a wing with a morphology that is clearly not optimized: a rectangular plate of which the measures are roughly based on the dronefly wing. The span, chord and location of the pitching axis are all taken as the mean values of those parameters for the dronefly wing, which results in a wing with measures as shown in Figure 5-23.

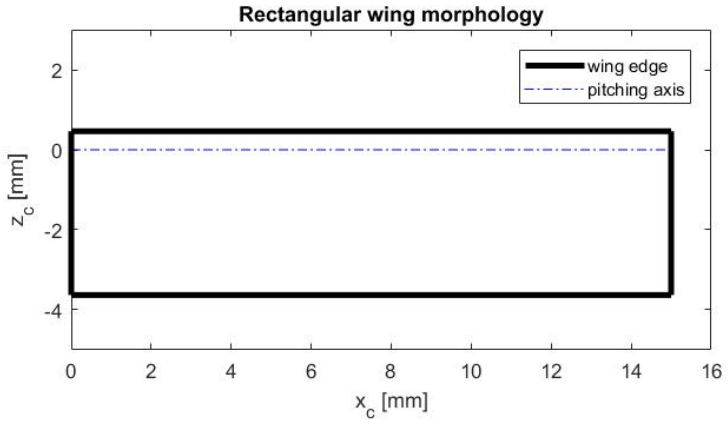

Figure 5-23: Rectangular wing planform, based on the shape of the dronefly wing design as used by Wang et al. [47].

Figure 5-24 clearly shows that the pitching pattern shows a different response to changes in k_η compared to the dronefly wing. For the lowest pitching stiffness, the pitching motion becomes rather unpredictable, for the highest two pitching stiffness values the pitching pattern resembles the dronefly wing kinematics, though the amplitude and phase changes are different.

Due to the unstable pitching behaviour for low pitching stiffness, the lift production is close to zero, or even negative for these attitude control settings, as shown in Figure 5-25. As seen before in the dronefly wing design analysis, the highest lift production occurs for the combination of both the highest values of the sweeping amplitude and pitching stiffness. The

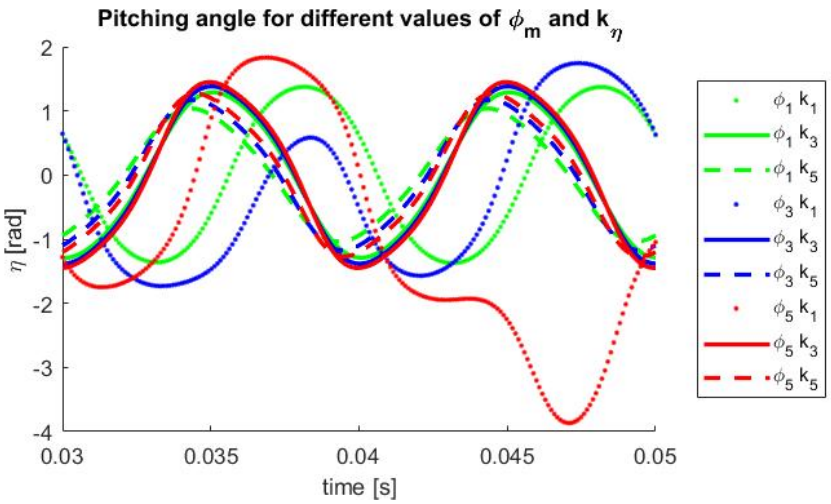

Figure 5-24: Pitching angle η associated with the rectangular wing for the same combination of attitude control parameters as in Figure 5-4. No body motions are taken into account in this case.

rectangular design is not optimized, so the efficiency does not show an optimal value around the main diagonal like the dronefly wing design shows in Figure 5-9. Moreover, Figure 5-26 shows some sudden decreases in efficiency, which are most likely caused by the unstable pitching patterns as shown in Figure 5-24.

The location of the average effective CP again only changes minimally due to changes in attitude control parameters. Hence, it is concluded that for non-optimized wings, the location of the CP does not play a significant role for attitude control. For completeness, a visual representation is given in appendix C in Figure C-3.

The analysis of the rectangular wing mostly shows that the tuning and design domain of the attitude control parameters is a delicate matter, which should be adjusted to the wing design. For the completeness of the study, the analysis of the rectangular wing that includes body motion is shown in appendix D, which shows that the basic influences of body motions that were shown for the dronefly wing in 5-3-2 hold for the rectangular wing shape as well, though the flapping kinematics become unstable for certain attitude control parameter combinations.

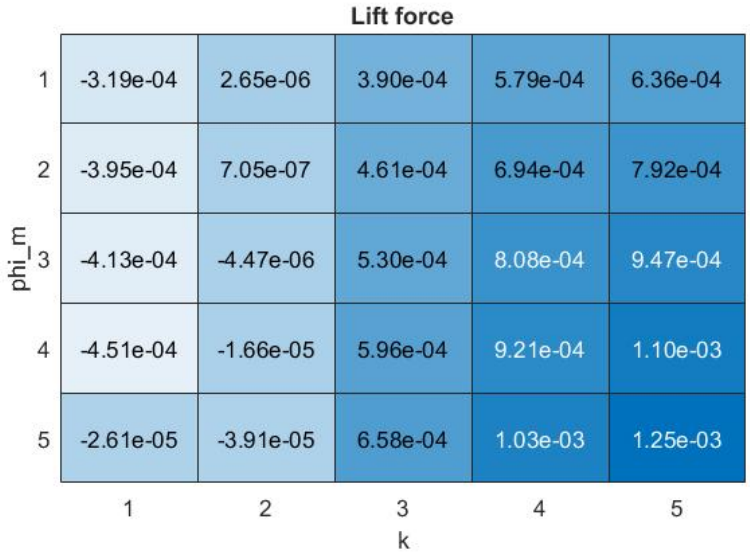

Figure 5-25: A quantitative heat map of the average lift produced by the rectangular flapping wing, associated with each of the 25 combinations of attitude control parameters. No body motions are taken into account in this case.

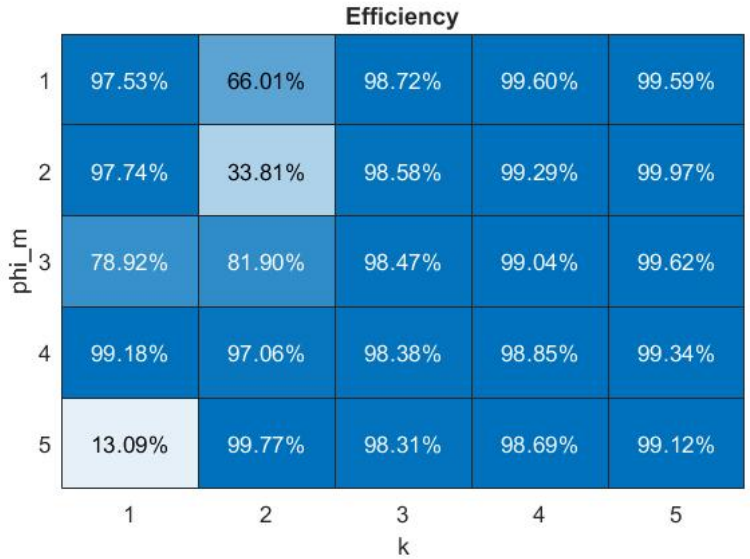

Figure 5-26: A quantitative heat map of the average efficiency of the wing stroke of the rectangular wing, associated with each of the 25 combinations of attitude control parameters. No body motions are taken into account in this case.

5-4 Discussion

The experiments that are done in the current work, provide a good insight in the response of flapping wings with respect to the two attitude control parameters ϕ_m and k_η, and their robustness with respect to flow induced by body motions. Due to the analytical methods that are used in this analysis, the model allows for quick comparison between flow cases, attitude control parameters and wing morphologies. For example, calculating the kinematics and forces of the forward flow case from section 5-3-2 for all 25 combinations of attitude control parameters during two wing beats takes around 300 seconds.

Firstly, it should be noted that the combination of a pitching stiffness that corresponds with the sweeping amplitude is essential for lift production, since both these parameters influence the AOA of the wing. This was shown in Figures 5-7 and 5-5, where the change in pitching stiffness from the first to the second value caused a 20% increase in lift production mostly induced by the translational term. When external flows are introduced, it appears that a higher stiffness results in a higher lift production, which partly originates from the earlier discussed match between sweeping and pitching motion and partly originates from a higher translational force being generated due to the external flow when the stiffness is higher. The higher pitching stiffness prevents the wing from rotating too far beyond its optimal AOA, therefore causing the generation of a higher lift force. Additionally, it has to be noted that the validity of the instantaneous force analysis that includes external flow might be doubtful in some cases. Especially Figure 5-19 shows large force spikes that are induced by the added mass term. This is due to the angular acceleration around the pitching angle of the wing α_{x_c} (not the second time derivative of the Euler angle η) shows sudden large increases during stroke reversal. Therefore, it was decided to use mostly the average lift forces for the conclusions in the current work, rather than the instantaneous forces. It should be noted decision to mostly base the quantitative research on average values is not unique for this study or the modeling methods, since it is shown more often in literature. Nevertheless, future physical experiments could verify if the quantitative analysis shows agreement with reality.

Furthermore, the effective CP does not change significantly when the attitude control parameters are varied. Larger changes are induced by the flow cases, but since those changes would happen symmetrically for all wings, this will most likely not be an issue, since within each flow case the change of effective CP location would still have an insignificant influence on the attitude control torques, compared to the changes in lift force.

Additionally, it was analyzed whether the response to attitude control parameters depends on the wing morphology. It was found that the passive pitching motion becomes rather different for different wing morphology, though the general principles that were found for the dronefly wing seem to hold true for this different morphology as well. The major difference was found in the efficiency of the wing stroke, which does not show any trend in optimal values and shows efficiency decreases up to 85% for the cases where the pitching kinematics become unstable.

Lastly, it should be noted that the conclusions that can be drawn from this chapter are only qualitative and the only quantitative results that are shown are from internal comparisons within the model that was used. Multiple real-life factors like wing flexibility, spanwise flow effects and other nonlinearities are not taken into account by this model. Therefore, it should be verified whether the qualitative results that were found hold true for physical experiments.

5-5 Chapter Conclusion

This chapter has shown the kinematic and aerodynamic changes that are induced by the two suggested attitude control parameters: the sweeping amplitude ϕ_m and pitching stiffness k_η. When no external flows due to body motion are applied, an increase in sweeping amplitude causes an increase in lift production, whereas an increase in pitching stiffness does not induce the same effect for all combinations of parameter settings. The combination of attitude control parameter settings with the lowest lift production, shows a decrease of 50% whereas the settings with the highest lift production show an increase of 50% with respect to the original settings. The changes in lift production efficiency due to variation of attitude control parameters are at most 2%.

External flow cases show that a minimal pitching stiffness is necessary for robust flapping motion and lift production. During forward motion, the sweeping amplitude and pitching stiffness can be increased for higher lift production, within the current modeling domain. The variability of the lift production slightly increases for the forward flow case, which shows a maximal increase in lift production of 59% and a maximal decrease in lift production of 56% compared to the lift production of the original attitude control parameters. For the vertical oscillation case, the maximal increase of lift production is as high as 75% while the maximal decrease in lift production for this case is 21%. This case of body motion shows an increase in lift for each increase step in pitching stiffness, but not necessarily with each increase step in sweeping amplitude. The lift production efficiency becomes lower when external flows are added that are induced by forward flight, up to a decrease of 27%, which is not surprising since the wing shape and flapping kinematics were initially optimized for the case that does not include flow from any direction. The drop in efficiency was lower, in the order of 2%, for the case where vertical oscillations during hovering were introduced.

Furthermore, the effective CP analysis shows that the variation of attitude control parameters do not significantly change the average effective CP of the aerodynamic forces. Therefore it can be concluded that the effective CP can be modeled as a constant point on the wing, and that changes in attitude control torques are only induced by changes in lift force per wing.

The analysis of a non-optimized rectangular wing suggests that the kinematics can show drastically different behaviour when the morphology is slightly adjusted. For the cases where the kinematics resemble the kinematics of the dronefly wing morphology, a similar lift force sensitivity with respect to the attitude control parameters is shown. However, some combinations of attitude control parameters, resulted in unstable wing kinematics, even though the same parameter design domain as before was used. The efficiency results are rather different from the dronefly morphology, since the non-optimized rectangular wing does not necessarily have the same optimal attitude control parameter design as the original dronefly morphology. Moreover, sudden large drops in efficiency were shown for certain parameter combinations that most likely originate from the corresponding unstable wing kinematics.

Chapter 6

Conclusion & Discussion

6-1 Conclusion

The research question in this work was the following:

Which attitude control mechanism is aerodynamically most suitable for the Atalanta?

In previous research, it was found that a variable stroke amplitude and a variable pitching stiffness are the two most utilized mechanisms for this purpose. These are estimated to be the two most promising options, especially when the additional design challenges for the Atalanta are considered, which only allow for actuators that are integrated within the compliant vehicle structure. Hence, the aerodynamic response of these mechanisms was compared. A quasi-steady analytical aerodynamic model was combined with an analytical Multi-Body Dynamics (MBD) description, so that the aerodynamic response of a flapping wing (based on the dronefly wing design) could be analyzed for different attitude control variables and different cases of body motion. This combination of a detailed analytical aerodynamic analysis with attitude control and an analytical MBD description of the vehicle body and wing is unique for the current work.

This work is intentionally focused on qualitative aerodynamic analysis, since physical measurements on attitude control and aerodynamic analysis including body motion are absent in literature. Therefore, it was researched whether the wing kinematics could be simplified so that a general formulation can be made for wing kinematics that does not depend largely on parameter tuning or kinematic measurements. From this research a kinematic description followed that includes a purely sinusoidal sweeping motion and an iterative description of the passive pitching motion, without taking the out of plane heaving motion of the wing into account. Within the boundaries of this model, quantitative analysis was done to further clarify aerodynamic performance differences between different attitude control parameters and body motion cases.

The results of this work show that without body motions, the passive pitching motion changes with variations in both the pitching stiffness and sweeping amplitude. The passive pitching motion changes in terms of amplitude and phase, which both play a large role in the production of aerodynamic forces since these influence the velocity of the wing and the Angle of Attack (AOA). When the aerodynamic forces are calculated for the case without body motion, it is shown that an increase in sweeping amplitude causes an increase in lift production throughout the complete parameter design domain, whereas the pitching stiffness shows clear local optima for lift production. For the case that does not include body motion, the maximal average lift force increase due to variation of attitude control parameters is 50%, and the maximal decrease in average lift force is 50% as well. The lift force variations for the other flow cases are of the same order of magnitude, though each flow case shows a different sensitivity to the attitude control parameters. When a constant frontal flow due to forward flight under a 30° angle is introduced, a higher pitching stiffness becomes more favourable in terms of lift production since it prevents the pitching angle to become too high. Furthermore, a test case that simulates vertical oscillatory motion due to hovering shows that for this case a higher sweeping amplitude results in a lower lift production when the pitching stiffness is too low. It should be noted that the aerodynamic efficiency only decreases at most 2% due to the variation of attitude control parameters in the case without body motion, opposed to a forward flight case where the efficiency can drop as much as 27%.
Furthermore, it was investigated whether the effective Center of Pressure (CP) changes significantly due to attitude control parameter variation. Each flow case shows a change in position of the effective CP due to variation of attitude control parameters, however these minimal position changes have an insignificant influence on the attitude control torques compared to the changes in lift force. This leads to the conclusion that the change in effective CP position does not influence the attitude control torques significantly.
Lastly, attitude control analysis was done with a non-optimized rectangular wing of which the size is comparable to that of the dronefly wing. The sensitivities to attitude control parameters that are found for this rectangular wing design, are comparable to those of the dronefly wing. However, the non-optimized wing shows a chaotic pitching pattern when the pitching stiffness parameter is low. Due to this change in parameter sensitivity, it is not possible yet to draw general conclusions on the aerodynamically most suitable attitude control mechanism for multiple wing morphologies and body motion conditions. The current model would be suitable to test the behaviour of other wing designs and body motion conditions, which would only require the morphological and kinematic inputs to be changed.

In conclusion, the current work presents a model that can be used to analyze the behaviour of a flapping wing for different attitude control parameters (sweeping amplitude and pitching stiffness), different cases of body motion and different wing morphologies. Combining these parameters to investigate the kinematic and aerodynamic effects of attitude control is unique for this work. Hence, this report shows a new approach towards the challenge of attitude control mechanism design for Flapping-Wing Air Vehicle (FWAV). The order of magnitude of the lift variation is similar for both attitude control parameters, so the conclusion for the most suitable attitude control mechanism must be based on other parameters like lift response predictability and robustness to body motions. Variation of the sweeping amplitude shows the most consistent variation in lift for the cases where the pitching stiffness is high enough to ensure that the pitching pattern does not become unstable.
Therefore, provided that the constant pitching stiffness is high enough to ensure predictable

and stable flapping kinematics, variation of the sweeping amplitude would be the aerodynamically most suitable attitude control method for the dronefly wing.

6-2 Discussion

First of all, it should be noted that this work only considers the aerodynamic response of the two suggested attitude control mechanisms, whereas other factors like mechanical efficiency or controllability could play a large role as well. Including these other factors in the analysis could give a more accurate picture of the complete performance of the attitude control mechanism and its physical implementation into an FWAV.
Additionally, flow cases including sideways flow along the wing span (the x_c axis) are not researched in this work. This flow case was omitted intentionally, since the current quasi-steady aerodynamic model does not include spanwise flow components. Attitude control analysis that includes these flows would be a valuable addition to the current work, since more cases of body motion could be included into the analysis, though it would require an extension of the aerodynamic formulation. Moreover, the passive heaving motion could be more significant than this work assumes, especially during cases of body motion that include vertical accelerations, such as the vertical oscillations during hovering that were analyzed in this study. This study only takes the introduced flows into account, without looking at the vertical inertia of the wings and body which could influence the heaving motion of the wing. Therefore, the hovering flow case in this work could be slightly idealized, and a more accurate analysis is required for a quantitative insight into the lift production for this body motion case.
Lastly, the dronefly wing design was used in this work instead of an Atalanta wing design, since physical measurements of the performance of the dronefly wing were available in literature. Once physical aerodynamic measurements of the Atalanta wing without body motions are available, the analysis in this study can be repeated for the Atalanta wing in order to draw conclusions on the most suitable attitude control mechanism for this wing design.

6-3 Future Recommendations

In this work, only one of the additional kinematic terms that were presented in chapter 3 was introduced for the analysis of flapping-wing aerodynamics. To describe the kinematics of the Atalanta wing drive mechanism (or wing drive mechanisms of other devices) in more detail, additional terms could be taken into account for a more specific analysis. An attempt to do so was made while using the Adams® MBD software, which gave promising results for future research, though no additional insights were gained yet for the current study. Furthermore, it could be considered to use the formulations in the current work as a subroutine in MBD analysis, much like the research by Kim et al. [19], in order to simulate flight dynamics in 6 degrees of freedom and investigate the stability of the vehicle.
Additionally, it is recommended to perform physical experiments to both verify the quantitative results in this work and explore the boundaries of the presented model for different wing designs, kinematic descriptions and attitude control parameters.

Appendix A

Time Derivatives of Rotation Matrices

Defining the velocity of a point of which the position depends on the rotational velocity of multiple reference frames is not trivial. As an example, the motion of point I due to rotational velocity of body B is analyzed, starting with the original definition of this velocity as used in 3-11: ${}^{G}\dot{\mathbf{R}}_{b}{}^{b}\mathbf{x}_{I/B}$.

This term contains a time derivative of a rotation matrix, which makes intuitive sense but is not useful in analysis of the linear velocity vector of point p. Therefore, it is necessary to reformulate this rotation term in terms of rotational velocities as done by Schwab et al. [44]. How this is done, will be explained step by step in the following sections.

A-1 Converting the Derived Rotation Matrix

As mentioned earlier, the velocity of point I relative to vehicle body CoM B due to rotation of the vehicle body is analyzed as an example. In short, this is written as:

$$ {}^{G}\dot{\mathbf{x}}_{I/B} = {}^{G}\dot{\mathbf{R}}_{b}{}^{b}\mathbf{x}_{I/B}. \tag{A-1} $$

By definition, the rotation matrices in this work are orthogonal matrices, meaning that

$$ \mathbf{R}^{-1} = \mathbf{R}^{T}. \tag{A-2} $$

Using the notation conventions in this work, this results in:

$$ ({}^{G}\mathbf{R}_{b})^{-1} = ({}^{G}\mathbf{R}_{b})^{T} = {}^{b}\mathbf{R}_{G}. \tag{A-3} $$

Now, by definition of the rotation matrices, the position of point I relative to point B can be defined in multiple ways. Firstly,

$$^{G}\mathbf{x}_{I/B} = {}^{G}\mathbf{R}_{b}{}^{b}\mathbf{x}_{I/B}, \tag{A-4}$$

hence

$$^{b}\mathbf{x}_{I/B} = ({}^{G}\mathbf{R}_{b})^{T}{}^{G}\mathbf{x}_{I/B} \tag{A-5}$$

holds true as well. Equation A-5 can be substituted into A-1, which leads to

$$^{G}\dot{\mathbf{x}}_{I/B} = {}^{G}\dot{\mathbf{R}}_{b}({}^{G}\mathbf{R}_{b})^{T}{}^{G}\mathbf{x}_{I/B}. \tag{A-6}$$

Since every term in equation A-6 is written in the same reference frame, the superscripts can be left out, which leaves the following equation:

$$\dot{\mathbf{x}}_{I/B} = \dot{\mathbf{R}}\mathbf{R}^{T}\mathbf{x}_{I/B}. \tag{A-7}$$

Equation A-7 shows that the effect of angular velocities in any reference frame can be represented by the term $\dot{\mathbf{R}}\mathbf{R}^{T}$. Considering that rotation matrix $\mathbf{R}$ is orthogonal, it can easily be proven that

$$\dot{\mathbf{R}}\mathbf{R}^{T} = \tilde{\boldsymbol{\omega}}, \tag{A-8}$$

where $\tilde{\boldsymbol{\omega}}$ is defined as the skew-symmetric tilde matrix that corresponds to the angular velocity vector in the following way:

$$\tilde{\boldsymbol{\omega}} = \boldsymbol{\omega} \times \mathbf{R}. \tag{A-9}$$

Hence, omega tilde is ordered in such a way that, when it is multiplied with a vector, it resembles the cross product between two vectors. Combining equations A-7 and A-8, results in the following expression:

$$\dot{\mathbf{x}}_{I/B} = \dot{\mathbf{R}}\mathbf{R}^{T}\mathbf{x}_{I/B} = \tilde{\boldsymbol{\omega}}\mathbf{x}_{I/B} = \boldsymbol{\omega}_{B} \times \mathbf{x}_{I/B}. \tag{A-10}$$

Since equation A-10 has no reference frame superscript, this relation holds for any velocity vector with corresponding angular velocity and position vectors as long as they are all defined in the same reference frame. It would appear that equation A-10 gives the final result for the linear velocity. However, the definitions of the angular velocity vector of body B $\boldsymbol{\omega}_{B}$ and position vector $\mathbf{x}_{I/B}$ in this equation are not trivial. Therefore, these will be further worked out in the next sections.

A-2 Vector Definitions

According to the cans-in-series formulation by Schwab [43], explained in chapter 3, the 3 DoF rotations of reference frames relative to each other can be represented by three consecutive rotations rather than three simultaneous rotations. Since the order in which these rotations are formulated is of importance, the angular velocity formulation needs to comply with this order of rotations as well. Moreover, the axes of rotation of the angular velocities change within the process of the reference frame transformation. Therefore, the rate of change of the Euler angles (which for the body rotations would be described as $\dot{\mathbf{\Psi}}, \dot{\mathbf{\Theta}}$ and $\dot{\mathbf{\Phi}}$) cannot be used as the angular velocity vector. In more practical terms, this means that the simple reference frame transformation from equation 3-15, for example, cannot be used. Therefore, Schwab et al. [44] have formulated a method for transforming rotational velocity vectors to a different reference frame, while using the rate of change of Euler angles, as follows. As an example, equation A-10 is formulated in the global frame, giving the following equation:

$$ {}^{G}\dot{\mathbf{x}}_{I/B} = {}^{G}\boldsymbol{\omega} \times {}^{G}\mathbf{x}_{I/B}. \tag{A-11} $$

From equation A-11, the angular velocity term $\boldsymbol{\omega}_B$ depends on the rate of change of Euler angles as follows:

$$ {}^{G}\boldsymbol{\omega}_B = {}^{G}\boldsymbol{\omega}_\Psi + \mathbf{R}_\Psi {}^{I}\boldsymbol{\omega}_\Theta + \mathbf{R}_\Psi \mathbf{R}_\Theta {}^{II}\boldsymbol{\omega}_\Phi. \tag{A-12} $$

Here, all respective angular velocities are defined as follows:

$$ \begin{aligned} {}^{G}\boldsymbol{\omega}_\Psi &= [0, 0, \dot{\Psi}]^T, \\ {}^{I}\boldsymbol{\omega}_\Theta &= [\dot{\Theta}, 0, 0]^T, \\ {}^{II}\boldsymbol{\omega}_\Psi &= [0, \dot{\Phi}, 0]^T. \end{aligned} \tag{A-13} $$

Here, the superscripts I and II refer to the intermediate reference frames after the rotations of Euler angles Ψ and Θ, respectively.

The definition of the other half of equation A-11, ${}^{G}\mathbf{x}_{I/B}$, is a straightforward computation involving only one reference frame transformation and the coordinates of point I in the body-fixed frame. Hence, this completes the derivation of the angular velocity term due to rotations of a body, with in this case the motion of hinge point I as an insightful example for analisys.

Appendix B

Angular Velocity & Acceleration Expressions

B-1 Angular Velocity

The computation of the angular velocity of wing W in the corotating frame, as explained in section 3-2, leads to a three-dimensional rotational velocity vector that consists of the following terms:

$$\begin{aligned} {}^{c}\boldsymbol{\omega}_W(1) = {} & \dot{\eta} - \dot{\Psi}(\cos\Theta(\cos\Phi\sin\theta + \sin\Phi\cos\phi\cos\theta) - \sin\Theta\cos\theta\sin\phi) - \\ & \dot{\phi}\sin\theta - \dot{\Theta}(\sin\Phi\sin\theta - \cos\Phi\cos\phi\cos\theta) + \dot{\Phi}\cos\theta\sin\phi, \end{aligned} \tag{B-1}$$

$$\begin{aligned} {}^{c}\boldsymbol{\omega}_W(2) = {} & \dot{\Phi}(\cos\eta\cos\phi + \sin\eta\sin\phi\sin\theta) + \\ & \dot{\Psi}(\sin\Theta(\cos\eta\cos\phi + \sin\eta\sin\phi\sin\theta) + \\ & \cos\Theta(\sin\Phi(\cos\eta\sin\phi - \cos\phi\sin\eta\sin\theta) + \cos\Phi\cos\theta\sin\eta)) - \\ & \dot{\Theta}(\cos\Phi(\cos\eta\sin\phi - \cos\phi\sin\eta\sin\theta) - \sin\Phi\cos\theta\sin\eta) + \\ & \dot{\theta}\cos\eta + \dot{\phi}\cos\theta\sin\eta, \end{aligned} \tag{B-2}$$

$$\begin{aligned} {}^{c}\boldsymbol{\omega}_W(3) = {} & \dot{\Theta}(\cos\Phi(\sin\eta\sin\phi + \cos\eta\cos\phi\sin\theta) + \sin\Phi\cos\eta\cos\theta) - \\ & \dot{\Psi}(\sin\Theta(\cos\phi\sin\eta - \cos\eta\sin\phi\sin\theta) + \\ & \cos\Theta(\sin\Phi(\sin\eta\sin\phi + \cos\eta\cos\phi\sin\theta) - \cos\Phi\cos\eta\cos\theta)) - \\ & \dot{\Phi}(\cos\phi\sin\eta - \cos\eta\sin\phi\sin\theta) - \dot{\theta}\sin\eta + \dot{\phi}\cos\eta\cos\theta. \end{aligned} \tag{B-3}$$

B-2 Angular Acceleration

The computation of angular acceleration of wing W in the corotating frame, as explained in section 3-2, leads to the a three-dimensional angular acceleration vector that consists of the following terms:

$$
\begin{aligned}
{}^{c}\dot{\boldsymbol{\omega}}_W(1) = {} & \ddot{\eta} - \ddot{\Psi}(\cos\Theta(\cos\Phi\sin\theta + \sin\Phi\cos\phi\cos\theta) - \sin\Theta\cos\theta\sin\phi) - \\
& \ddot{\phi}\sin\theta - \ddot{\Theta}(\sin\Phi\sin\theta - \cos\Phi\cos\phi\cos\theta) + \ddot{\Phi}\cos\theta\sin\phi + \\
& \dot{\phi}(\dot{\Psi}(\sin\Theta\cos\phi\cos\theta + \cos\Theta\sin\Phi\cos\theta\sin\phi) + \\
& \dot{\Phi}\cos\phi\cos\theta - \dot{\Theta}\cos\Phi\cos\theta\sin\phi) - \\
& \dot{\theta}(\dot{\Psi}(\cos\Theta(\cos\Phi\cos\theta - \sin\Phi\cos\phi\sin\theta) + \sin\Theta\sin\phi\sin\theta) + \\
& \dot{\phi}\cos\theta + \dot{\Theta}(\sin\Phi\cos\theta + \cos\Phi\cos\phi\sin\theta) + \dot{\Phi}\sin\phi\sin\theta) - \\
& \dot{\Phi}(\dot{\Theta}(\cos\Phi\sin\theta + \sin\Phi\cos\phi\cos\theta) - \\
& \dot{\Psi}\cos\Theta(\sin\Phi\sin\theta - \cos\Phi\cos\phi\cos\theta)) + \\
& \dot{\Psi}\dot{\Theta}(\sin\Theta(\cos\Phi\sin\theta + \sin\Phi\cos\phi\cos\theta) + \cos\Theta\cos\theta\sin\phi),
\end{aligned}
\tag{B-4}
$$

$$
\begin{aligned}
{}^{c}\dot{\boldsymbol{\omega}}_W(2) = {} & \ddot{\Phi}(\cos\eta\cos\phi + \sin\eta\sin\phi\sin\theta) + \\
& \ddot{\Psi}(\sin\Theta(\cos\eta\cos\phi + \sin\eta\sin\phi\sin\theta) + \\
& \cos\Theta(\sin\Phi(\cos\eta\sin\phi - \cos\phi\sin\eta\sin\theta) + \cos\Phi\cos\theta\sin\eta)) - \\
& \ddot{\Theta}(\cos\Phi(\cos\eta\sin\phi - \cos\phi\sin\eta\sin\theta) - \sin\Phi\cos\theta\sin\eta) + \\
& \ddot{\theta}\cos\eta + \ddot{\phi}\cos\theta\sin\eta + \\
& \dot{\Phi}(\dot{\Theta}(\sin\Phi(\cos\eta\sin\phi - \cos\phi\sin\eta\sin\theta) + \cos\Phi\cos\theta\sin\eta) + \\
& \dot{\Psi}\cos\Theta(\cos\Phi(\cos\eta\sin\phi - \cos\phi\sin\eta\sin\theta) - \sin\Phi\cos\theta\sin\eta)) - \\
& \dot{\theta}(\dot{\Theta}(\sin\Phi\sin\eta\sin\theta - \cos\Phi\cos\phi\cos\theta\sin\eta) + \\
& \dot{\Psi}(\cos\Theta(\cos\Phi\sin\eta\sin\theta + \sin\Phi\cos\phi\cos\theta\sin\eta) - \\
& \sin\Theta\cos\theta\sin\eta\sin\phi) + \dot{\phi}\sin\eta\sin\theta - \dot{\Phi}\cos\theta\sin\eta\sin\phi) - \\
& \dot{\phi}(\dot{\Phi}(\cos\eta\sin\phi - \cos\phi\sin\eta\sin\theta) + \dot{\Psi}(\sin\Theta(\cos\eta\sin\phi - \\
& \cos\phi\sin\eta\sin\theta) - \cos\Theta\sin\Phi(\cos\eta\cos\phi + \sin\eta\sin\phi\sin\theta)) + \\
& \dot{\Theta}\cos\Phi(\cos\eta\cos\phi + \sin\eta\sin\phi\sin\theta)) - \\
& \dot{\eta}(\dot{\Phi}(\cos\phi\sin\eta - \cos\eta\sin\phi\sin\theta) + \\
& \dot{\Psi}(\sin\Theta(\cos\phi\sin\eta - \cos\eta\sin\phi\sin\theta) + \\
& \cos\Theta(\sin\Phi(\sin\eta\sin\phi + \cos\eta\cos\phi\sin\theta) - \cos\Phi\cos\eta\cos\theta)) - \\
& \dot{\Theta}(\cos\Phi(\sin\eta\sin\phi + \cos\eta\cos\phi\sin\theta) + \sin\Phi\cos\eta\cos\theta) + \\
& \dot{\theta}\sin\eta - \dot{\phi}\cos\eta\cos\theta) + \dot{\Psi}\dot{\Theta}(\cos\Theta(\cos\eta\cos\phi + \sin\eta\sin\phi\sin\theta) - \\
& \sin\Theta(\sin\Phi(\cos\eta\sin\phi - \cos\phi\sin\eta\sin\theta) + \cos\Phi\cos\theta\sin\eta)),
\end{aligned}
\tag{B-5}
$$

$$
\begin{aligned}
{}^{c}\dot{\boldsymbol{\omega}}_{W}(3) = {} & \ddot{\Theta}(\cos\Phi(\sin\eta\sin\phi+\cos\eta\cos\phi\sin\theta)+\sin\Phi\cos\eta\cos\theta)- \\
& \ddot{\Psi}(\sin\Theta(\cos\phi\sin\eta-\cos\eta\sin\phi\sin\theta)+ \\
& \cos\Theta(\sin\Phi(\sin\eta\sin\phi+\cos\eta\cos\phi\sin\theta)-\cos\Phi\cos\eta\cos\theta))- \\
& \ddot{\Phi}(\cos\phi\sin\eta-\cos\eta\sin\phi\sin\theta)-\ddot{\theta}\sin\eta+\ddot{\phi}\cos\eta\cos\theta+ \\
& \dot{\phi}(\dot{\Phi}(\sin\eta\sin\phi+\cos\eta\cos\phi\sin\theta)+ \\
& \dot{\Psi}(\sin\Theta(\sin\eta\sin\phi+\cos\eta\cos\phi\sin\theta)- \\
& \cos\Theta\sin\Phi(\cos\phi\sin\eta-\cos\eta\sin\phi\sin\theta))+ \\
& \dot{\Theta}\cos\Phi(\cos\phi\sin\eta-\cos\eta\sin\phi\sin\theta))- \\
& \dot{\Phi}(\dot{\Theta}(\sin\Phi(\sin\eta\sin\phi+\cos\eta\cos\phi\sin\theta)-\cos\Phi\cos\eta\cos\theta)+ \\
& \dot{\Psi}\cos\Theta(\cos\Phi(\sin\eta\sin\phi+\cos\eta\cos\phi\sin\theta)+\sin\Phi\cos\eta\cos\theta))- \\
& \dot{\theta}(\dot{\Theta}(\sin\Phi\cos\eta\sin\theta-\cos\Phi\cos\eta\cos\phi\cos\theta)+ \\
& \dot{\Psi}(\cos\Theta(\cos\Phi\cos\eta\sin\theta+\sin\Phi\cos\eta\cos\phi\cos\theta)- \\
& \sin\Theta\cos\eta\cos\theta\sin\phi)+\dot{\phi}\cos\eta\sin\theta-\dot{\Phi}\cos\eta\cos\theta\sin\phi)- \\
& \dot{\eta}(\dot{\Phi}(\cos\eta\cos\phi+\sin\eta\sin\phi\sin\theta)+ \\
& \dot{\Psi}(\sin\Theta(\cos\eta\cos\phi+\sin\eta\sin\phi\sin\theta)+ \\
& \cos\Theta(\sin\Phi(\cos\eta\sin\phi-\cos\phi\sin\eta\sin\theta)+\cos\Phi\cos\theta\sin\eta))- \\
& \dot{\Theta}(\cos\Phi(\cos\eta\sin\phi-\cos\phi\sin\eta\sin\theta)-\sin\Phi\cos\theta\sin\eta)+ \\
& \dot{\theta}\cos\eta+\dot{\phi}\cos\theta\sin\eta)-\dot{\Psi}\dot{\Theta}(\cos\Theta(\cos\phi\sin\eta-\cos\eta\sin\phi\sin\theta)- \\
& \sin\Theta(\sin\Phi(\sin\eta\sin\phi+\cos\eta\cos\phi\sin\theta)-\cos\Phi\cos\eta\cos\theta)).
\end{aligned}
\tag{B-6}
$$

Appendix C

Additional CP Analysis

Figure C-1 shows the different Center of Pressure (CP) locations for the case of forward motion, Figure C-2 shows the different CP locations for the the case of vertical oscillations during hovering. Figure C-3 shows the different CP locations for the rectangular wing, without any body motions taken into account.

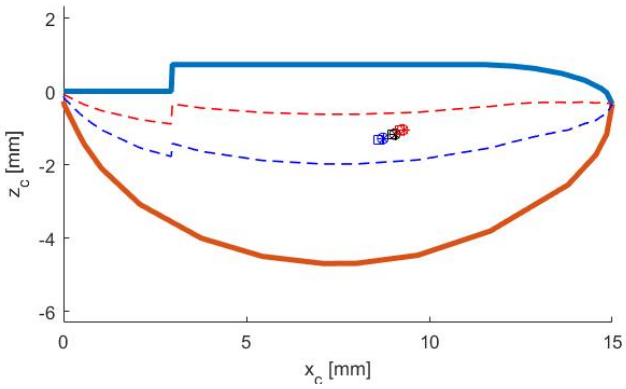

Figure C-1: Schematic representation of the flapping wing, with the CP locations of the 9 most characteristic combinations of attitude control parameters that were used for Figure 5-4 as well. This figure corresponds to the case of forward body motion. Red and blue dashed lines correspond to the quarter chord and half chord respectively.

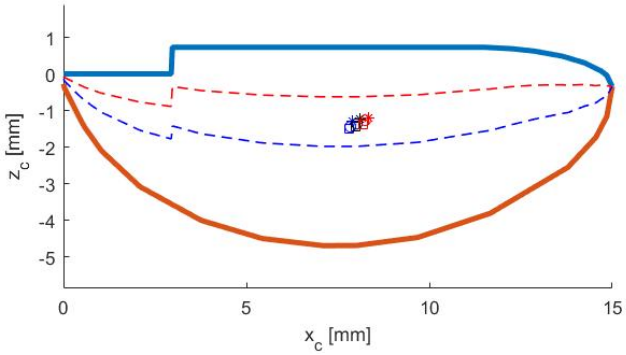

Figure C-2: Schematic representation of the flapping wing, with the CP locations of the 9 most characteristic combinations of attitude control parameters that were used for Figure 5-4 as well. This figure corresponds to the case of vertical oscillations during hover. Red and blue dashed lines correspond to the quarter chord and half chord respectively.

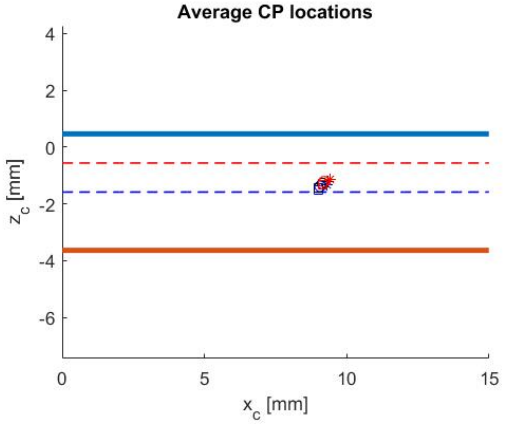

Figure C-3: Schematic representation of the rectangular flapping wing, with the CP locations of the 9 most characteristic combinations of attitude control parameters that were used for Figure 5-4 as well. This figure corresponds to the case that does not take body motions into account. Red and blue dashed lines correspond to the quarter chord and half chord respectively.

Appendix D

Rectangular Wing Body Motion Analysis

The section below contains the aerodynamic analysis that includes flows induced by body motions, for the non-optimized rectangular wing from section 5-3-3.

D-1 Forward Flight

The aerodynamic response of the rectangular wing was analyzed for the same body motion conditions as used in 5-3-2.

Figure D-1 shows that the lowest pitching stiffness results in very unstable kinematics, which is expected due to the earlier results of the rectangular wing in the still case. The highest two stiffness values result in the usual periodic behaviour with a negative pitching angle offset as seen earlier in Figure 5-11.

The lift forces for this flow case are generally higher than the case without flow as shown in Figure D-2. Again, it is shown that for this flow case an increase in pitching stiffness means an increase in lift whereas an increase in sweeping amplitude does not necessarily increase the average lift force. The highest lift force is generated when the sweep amplitude and pitching stiffness are at their highest. Despite the higher lift forces, the overall efficiency of the wing stroke drops for this wing morphology as well, as shown in Figure D-3. This effect is also visible in the earlier forward flight analysis of the dronefly wing. Due to the non-optimized wing design, the efficiency does not show a clear optimum.

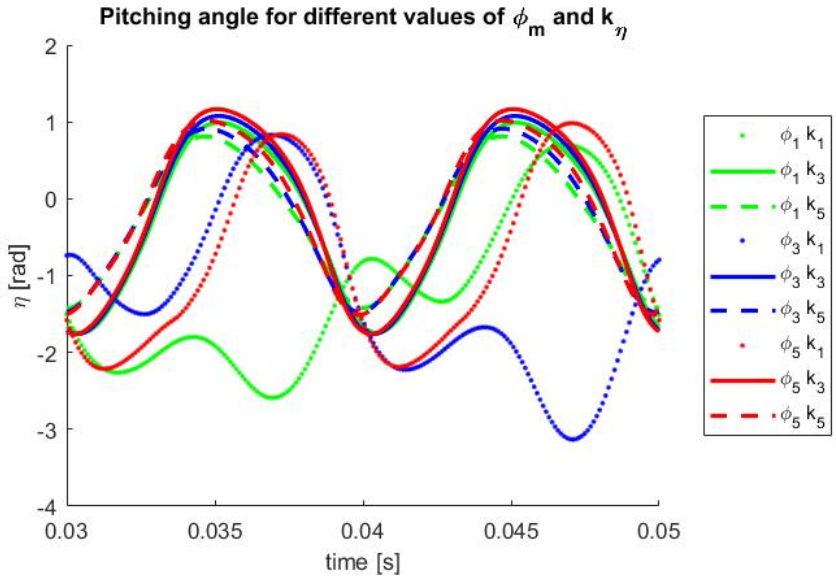

Figure D-1: Pitching angle η associated with the rectangular wing for the same combination of attitude control parameters as in Figure 5-4. This figure corresponds to the forward flight body motion case.

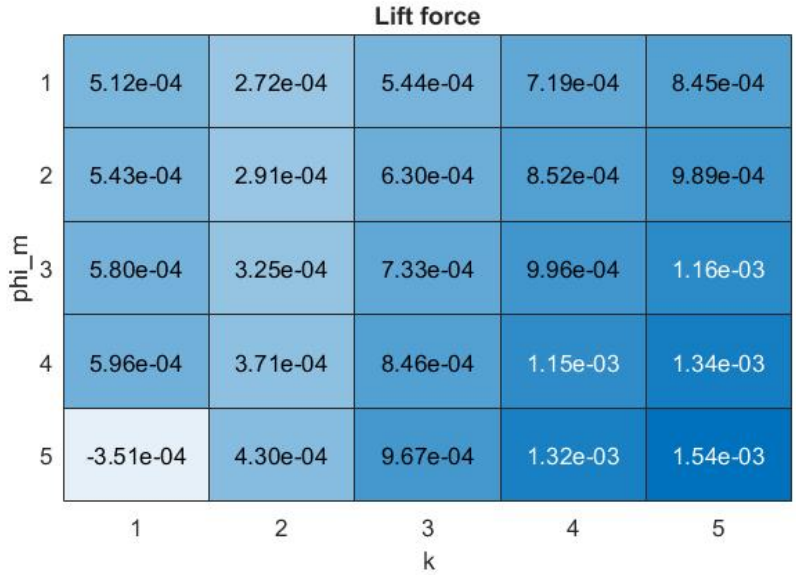

Figure D-2: A quantitative heat map of the average lift produced by the rectangular flapping wing, associated with each of the 25 combinations of attitude control parameters. The figure is associated with the forward flight body motion case.

Figure D-3: A quantitative heat map of the average efficiency of the wing stroke of the rectangular wing, associated with each of the 25 combinations of attitude control parameters. The figure is associated with the forward flight body motion case.

D-2 Oscillations During Hovering

The aerodynamic response of the rectangular wing has been analyzed for the case of body motion that simulates vertical oscillations due to hovering as well. The same body motion description was used as in section 5-3-2.

Figure D-4 shows that the pitching kinematics become unstable for the lowest setting of pitching stiffness, whereas the higher pitching stiffness values cause stable periodic pitching behaviour.

Figure D-5 shows the average lift force for all combinations of attitude control parameters. The two lowest values for the pitching stiffness result in negative average lift forces, higher pitching stiffness values result in positive average lift forces. Interestingly, for higher values of the pitching stiffness (k_3 or higher), the average lift does not always increase with an increase in sweeping amplitude.

Figure D-6 shows the efficiency of the average lift production for all combinations of attitude control parameters. No clear optimum for the efficiency could be found, and the efficiency rapidly drops for the lowest value of pitching stiffness.

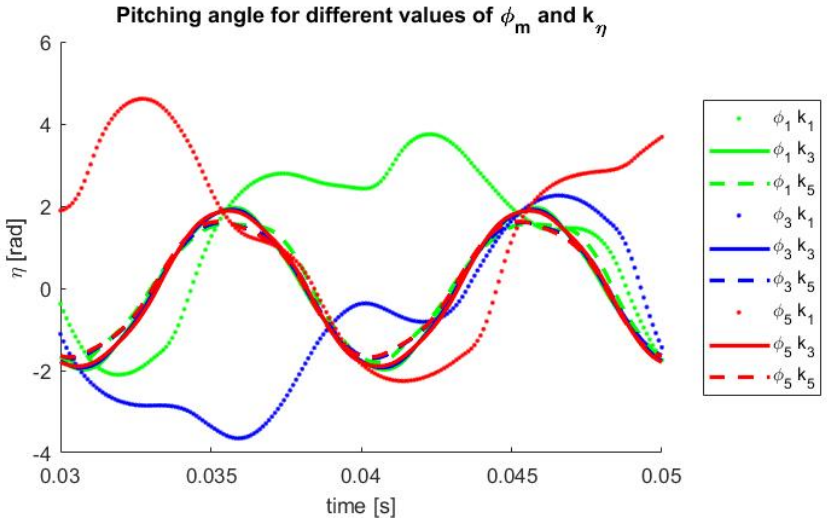

Figure D-4: Pitching angle η associated with the rectangular wing for the same combination of attitude control parameters as in Figure 5-4. This figure corresponds to the vertical oscillation body motion case.

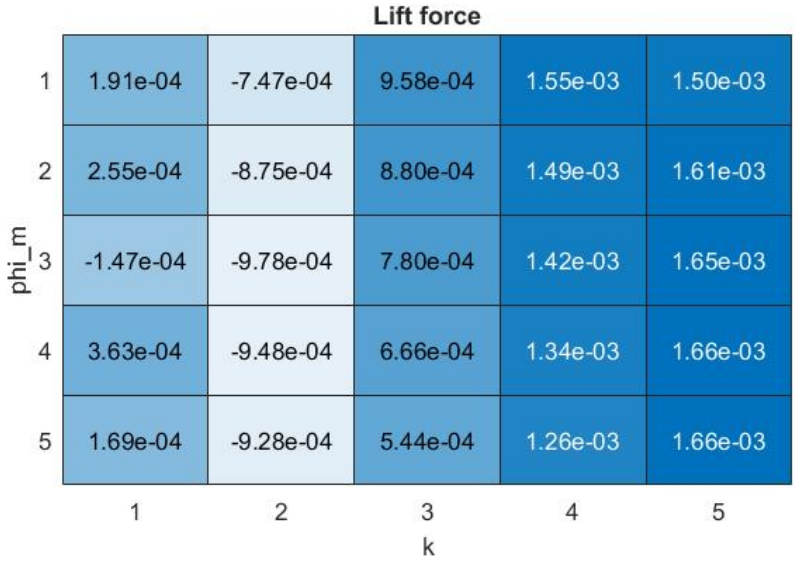

Figure D-5: A quantitative heat map of the average lift produced by the rectangular flapping wing, associated with each of the 25 combinations of attitude control parameters. The figure is associated with the vertical oscillation body motion case.

Figure D-6: A quantitative heat map of the average wing stroke efficiency of the rectangular flapping wing, associated with each of the 25 combinations of attitude control parameters. The figure is associated with the vertical oscillation body motion case.

Bibliography

[1] Gordon J. Berman and Z. Jane Wang. Energy-minimizing kinematics in hovering insect flight. *Journal of Fluid Mechanics*, 582(July):153–168, 2007.

[2] Caspar T. Bolsman. *Flapping wing actuation using resonant compliant mechanisms*. 2010.

[3] Katie Byl. A passive dynamic approach for flapping-wing micro-aerial vehicle control.

[4] Chen Chen and Tianyu Zhang. A review of design and fabrication of the bionic flapping wing micro air vehicles. *Micromachines*, 10(2), 2019.

[5] Xiaokai Chi, Shaoping Wang, Yixin Zhang, Xingjian Wang, and Qing Guo. A tailless butterfly-type ornithopter with low aspect ratio wings. *IET Conference Publications*, 2018(CP743), 2018.

[6] David Coleman, Moble Benedict, Vikram Hirishikeshaven, and Inderjit Chopra. Development of a robotic hummingbird capable of controlled hover. *Journal of the American Helicopter Society*, 62(3):1–9, 2017.

[7] G C H E De Croon, K M E De Clercq, R Ruijsink, and B Remes. based control of the DelFly. 1(2):71–98, 2009.

[8] Christophe De Wagter, Matěj Karásek, and Guido de Croon. Quad-thopter: Tailless flapping wing robot with four pairs of wings. *International Journal of Micro Air Vehicles*, 10(3):244–253, 2018.

[9] R Diekerhof. Resonating structures with flapping wings. 2016.

[10] Michael A.A. Fenelon. Biomimetic flapping wing aerial vehicle. *2008 IEEE International Conference on Robotics and Biomimetics, ROBIO 2008*, pages 1053–1058, 2009.

[11] Michael A.A. Fenelon and Tomonari Furukawa. Design of an active flapping wing mechanism and a micro aerial vehicle using a rotary actuator. *Mechanism and Machine Theory*, 45(2):137–146, 2010.

[12] Nina Gaissert, Rainer Mugrauer, Günter Mugrauer, Agalya Jebens, Kristof Jebens, and Elias Maria Knubben. Inventing a Micro Aerial Vehicle Inspired by the Mechanics of Dragonfly Flight. *Towards Autonomous Robotic Systems*, 8069:15–27, 2014.

[13] John Gerdes, Alex Holness, Ariel Perez-Rosado, Luke Roberts, Adrian Greisinger, Eli Barnett, Johannes Kempny, Deepak Lingam, Chen Haur Yeh, Hugh A. Bruck, and Satyandra K. Gupta. Robo Raven: A Flapping-Wing Air Vehicle with Highly Compliant and Independently Controlled Wings. *Soft Robotics*, 1(4):275–288, 2014.

[14] Du Hyun Gong, Da Woon Lee, Sang Joon Shin, and Sang Yong Kim. String-based flapping mechanism and modularized trailing edge control system for insect-type FWMAV. *International Journal of Micro Air Vehicles*, 11, 2019.

[15] Gregory Gremillion, Paul Samuel, and J. Sean Humbert. Yaw feedback control of a bio-inspired flapping wing vehicle. *Micro- and Nanotechnology Sensors, Systems, and Applications IV*, 8373(May):83731H, 2012.

[16] Lindsey Hines, Domenico Campolo, and Metin Sitti. Liftoff of a motor-driven, flapping-wing microaerial vehicle capable of resonance. *IEEE Transactions on Robotics*, 30(1):220–232, 2014.

[17] Matej Karasek, Florian T. Muijres, Christophe De Wagter, Bart D.W. Remes, and Guido C.H.E. De Croon. A tailless aerial robotic flapper reveals that flies use torque coupling in rapid banked turns. *Science*, 361(6407):1089–1094, 2018.

[18] Matthew Keennon, Karl Klingebiel, Henry Won, and Alexander Andriukov. Development of the nano hummingbird: A tailless flapping Wing Micro Air Vehicle. *50th AIAA Aerospace Sciences Meeting Including the New Horizons Forum and Aerospace Exposition*, (January):1–24, 2012.

[19] Joong Kwan Kim and Jae Hung Han. A multibody approach for 6-DOF flight dynamics and stability analysis of the hawkmoth Manduca sexta. *Bioinspiration and Biomimetics*, 9(1), 2014.

[20] David Lentink, Stefan R. Jongerius, and Nancy L. Bradshaw. The Scalable Design of Flapping Micro-Air Vehicles Inspired by Insect Flight. *Flying Insects and Robots*, (August 2009):1–316, 2010.

[21] Kevin Y. Ma, Pakpong Chirarattananon, Sawyer B. Fuller, and Robert J. Wood. Controlled Flight of a Biologically Inspired, Insect-Scale Robot. *Science*, (May):603–607, 2013.

[22] Dana Mackenzie. Avionics. A flapping of wings. *Science*, 335(6075):1430–3, 2012.

[23] Hosein Mahjoubi and Katie Byl. Analysis of a tunable impedance method for practical control of insect-inspired flapping-wing MAVs. *Proceedings of the IEEE Conference on Decision and Control*, pages 3539–3546, 2011.

[24] Hosein Mahjoubi and Katie Byl. Steering and horizontal motion control in insect-inspired flapping-wing MAVs: The tunable impedance approach. *Proceedings of the American Control Conference*, pages 901–908, 2012.

[25] Quoc Viet Nguyen and Woei Leong Chan. Development and flight performance of a biologically-inspired tailless flapping-wing micro air vehicle with wing stroke plane modulation. *Bioinspiration and Biomimetics*, 14(1), 2019.

[26] Michael Ol, Gregory Parker, Gregg Abate, and Johnny Evers. Flight controls and performance challenges for MAVs in complex environments. *AIAA Guidance, Navigation and Control Conference and Exhibit*, (August), 2008.

[27] M. F. OSBORNE. Aerodynamics of flapping flight with application to insects. *The Journal of experimental biology*, 28(2):221–245, 1951.

[28] Joon Hyuk Park, Emily P. Yang, Chengkun Zhang, and Sunil K. Agrawal. Kinematic design of an asymmetric in-phase flapping mechanism for MAVs. *Proceedings - IEEE International Conference on Robotics and Automation*, (May):5099–5104, 2012.

[29] H. J. Peters, J. F.L. Goosen, and F. Van Keulen. Methods to actively modify the dynamic response of cm-scale FWMAV designs. *Smart Materials and Structures*, 25(5), 2016.

[30] Hugo Peters. *A Controllability Approach for Resonant Compliant Systems*, volume 6. 2016.

[31] Hugo Peters, Qi Wang, Hans Goosen, and Fred Van Keulen. Active control of the hinge of a flapping wing with electrostatic sticking to modify the passive pitching motion. *Computational Methods in Applied Sciences*, 43(January 2016):153–174, 2017.

[32] H V Phan, S Aurecianus, T Kang, and H C Park. Attitude Control Mechanism in an Insect-like Tailless Two- winged Flying Robot by Simultaneous Modulation of Stroke Plane and Wing Twist. (November):1–6, 2018.

[33] Hoang Vu Phan, Taesam Kang, and Hoon Cheol Park. Design and stable flight of a 21 g insect-like tailless flapping wing micro air vehicle with angular rates feedback control. *Bioinspiration and Biomimetics*, 12(3), 2017.

[34] Hoang Vu Phan and Hoon Cheol Park. Insect-inspired, tailless, hover-capable flapping-wing robots: Recent progress, challenges, and future directions. *Progress in Aerospace Sciences*, 111(September):100573, 2019.

[35] Max F. Platzer, Kevin D. Jones, John Young, and Joseph C.S. Lai. Flapping-wing aerodynamics: Progress and challenges. *AIAA Journal*, 46(9):2136–2149, 2008.

[36] Alireza Ramezani, Soon Jo Chung, and Seth Hutchinson. A biomimetic robotic platform to study flight specializations of bats. *Science Robotics*, 2(3):1–13, 2017.

[37] Jayant Ratti and George Vachtsevanos. Inventing a biologically inspired, energy efficient micro aerial vehicle. *Journal of Intelligent and Robotic Systems: Theory and Applications*, 65(1-4):437–455, 2012.

[38] Cameron Rose and Ronald S. Fearing. Comparison of ornithopter wind tunnel force measurements with free flight. *Proceedings - IEEE International Conference on Robotics and Automation*, pages 1816–1821, 2014.

[39] A. Roshanbin, H. Altartouri, M. Karásek, and A. Preumont. COLIBRI: A hovering flapping twin-wing robot. *International Journal of Micro Air Vehicles*, 9(4):270–282, 2017.

[40] Mark Ryan and Hai Jun Su. Classification of flapping wing mechanisms for micro air vehicles. *Proceedings of the ASME Design Engineering Technical Conference*, 4(PARTS A AND B):105–115, 2012.

[41] Gottfried Sachs. Comparison of power requirements: Flapping vs. fixed wing vehicles. *Aerospace*, 3(4), 2016.

[42] Sanjay P. Sane and Michael H. Dickinson. The aerodynamic effects of wing rotation and a revised quasi-steady model of flapping flight. *Journal of Experimental Biology*, 205(8):1087–1096, 2002.

[43] A. L. Schwab and J. P. Meijaard. How to draw Euler angles and utilize Euler parameters. *Proceedings of the ASME Design Engineering Technical Conference*, 2006, 2006.

[44] H. Vallery and A.L. Schwab. *Advanced Dynamics*. 2018.

[45] H. Wagner. Über die entstehung des dynamischen auftriebes von tragflügeln. *Ztschr. F. Angew. Math. und Mech.*, 1925.

[46] Q. Wang, J. F. L. Goosen, and F. van Keulen. Study of design parameters of flapping-wings. *International Micro Air Vehicle Conference and Flight Competition (IMAV2014)*, pages 1–10, 2014.

[47] Q. Wang, J. F.L. Goosen, and F. Van Keulen. A predictive quasi-steady model of aerodynamic loads on flapping wings. *Journal of Fluid Mechanics*, 800:688–719, 2016.

[48] J. P. Whitney and R. J. Wood. Aeromechanics of passive rotation in flapping flight. *Journal of Fluid Mechanics*, 660:197–220, 2010.

[49] Alexander P. Willmott and Charles P. Ellington. The mechanics of flight in the hawkmoth Manduca sexta I. Kinematics of hovering and forward flight. *Journal of Experimental Biology*, 200(21):2705–2722, 1997.

[50] Jian Zhang, Zhan Tu, Fan Fei, and Xinyan Deng. Geometric flight control of a hovering robotic hummingbird. *Proceedings - IEEE International Conference on Robotics and Automation*, pages 5415–5421, 2017.